Measurement of the Top Quark Mass from b-tagged events in the Lepton Plus Jets Channel in $p\bar{p}$ Collisions at $\sqrt{s} = 1.8$ TeV

by

Nathan Robert-Claire Eddy

A dissertation submitted in partial fulfillment
of the requirements for the degree of
Doctor of Philosophy
(Physics)
in The University of Michigan
1999

Doctoral Committee:

Professor J. Wehrley Chapman, Chair
Professor Ratin Akhoury
Professor Dante Amidei
Professor Richard B. Brown
Professor John Keith Riles

Acknowledgments

This thesis is the result of a large collaborative effort. I would like to thank the Fermilab staff and all the members of CDF. Without their tireless efforts the experiment would not be possible.

I would like to thank my advisor, J. W. Chapman, for introducing me to the field of High Energy Physics and giving me the opportunity to work on CDF. I appreciate the freedom he allowed me and am grateful for the guidance he provided when needed. I am grateful to Dan Amidei for encouraging me to pursue top quark physics and for providing many useful suggestions. I would especially like to thank Steve Vejcik and Soo-Bong Kim for taking me under their wings and expanding my understanding of experimental top quark physics. This dissertation would not have been possible without Steve's guidance throughout.

This thesis is founded upon an innumerable amount of work by members of the CDF top and top mass working groups. I am especially grateful to all the members of these groups whose work, comments, and suggestions contributed to the top mass analysis. In particular, I'd like to thank Rob Roser, Luc Demortier, Lina Galtieri, and Jeremy Lys for their contributions and numerous discussions on the subject of the top quark mass.

I would like to thank my entire family for their support and encouragement throughout my life. I am eternally grateful to my Mom and Dad for their love and for the opportunites they have given me.

Table of Contents

Acknowledgments ii

List of Tables vi

List of Figures viii

List of Appendices xi

Chapter

1. Introduction 1

2. Theory 3
- 2.1 Standard Model 4
- 2.2 Proton Anti-proton Collisions 8
- 2.3 Top Quark Production and Decay 9
- 2.4 Top Mass 12

3. Experimental Apparatus 14
- 3.1 The Tevatron 14
- 3.2 The CDF Detector 16
- 3.3 Tracking Detectors 17
  - 3.3.1 SVX 18
  - 3.3.2 VTX 19
  - 3.3.3 CTC 20
- 3.4 Calorimetry 21
  - 3.4.1 Central Calorimeter 22
  - 3.4.2 Plug and Forward Calorimeters 25
- 3.5 Muon Detectors 26
- 3.6 The Trigger System 28
- 3.7 Offline Reconstruction 29

4. Event Samples . . . 31
4.1 Data . . . 31
4.1.1 Triggers . . . 32
4.1.2 Electron Selection . . . 33
4.1.3 Muon Selection . . . 35
4.1.4 W Selection . . . 36
4.1.5 Top Mass Sample . . . 38
4.1.6 b-Tagging . . . 39
4.1.7 Tagged Sample . . . 42
4.1.8 Backgrounds . . . 43
4.2 Monte Carlo . . . 44
4.2.1 Top Samples . . . 45
4.2.2 Background Samples . . . 45

5. $t\bar{t}$ Reconstruction Algorithm . . . 47
5.1 Constraints . . . 47
5.2 Corrections . . . 50
5.2.1 Jet Energy . . . 51
5.2.2 Unclustered Energy . . . 56
5.3 Performance of Reconstruction Algorithm . . . 57

6. Determining the Top Mass . . . 61
6.1 Templates . . . 62
6.1.1 $t\bar{t}$ Signal . . . 62
6.1.2 QCD W+jets Background . . . 66
6.2 Background Calculation . . . 67
6.3 Likelihood Fit . . . 68
6.3.1 Checks . . . 70
6.3.2 Data Results . . . 72

7. Systematic Uncertainties . . . 75
7.1 Jet-Parton E_T Scale . . . 76
7.1.1 Detector Effects . . . 76
7.1.2 Soft Gluon Effects . . . 79
7.1.3 Summary of Jet-Parton E_T Scale Uncertainties . . . 81
7.2 Initial and Final State Hard Radiation . . . 81
7.3 Background Mass Distribution . . . 84
7.4 B-tagging Bias . . . 84
7.5 Parton Distribution Functions . . . 85
7.6 Monte Carlo Generators . . . 86
7.7 Summary of Systematic Uncertainties . . . 86

8. Conclusions . . . 87

Appendices 89

Bibliography 111

List of Tables

Table

2.1 The six fermions (leptons and quarks) currently known along with their electric charge, Q, and the forces via which they interact. 4

2.2 The gauge bosons known in the Standard Model. The coupling constant (α) is given as the strength in comparison to the strong force at 10^{-13} cm, the approximate radius of the proton. 6

2.3 Branching ratios for $t\bar{t}$ decay modes assuming standard model couplings. Here q stands for a u, d, c or s quark. 10

3.1 Characteristics of central and endwall calorimeters. Interaction lengths are given in radiation lengths (X_0) and absorption lengths (λ_0). The two components of the energy resolution are added in quadrature. The electromagnetic resolution is for isolated is for isolated electromagnetic particles and the hadronic resolution is for isolated pions. 23

3.2 Characteristics of central and endwall calorimeters. Interaction lengths are given in radiation lengths (X_0) and absorption lengths (λ_0). The two components of the energy resolution are added in quadrature. 25

4.1 Level 2 triggers used to select primary muon candidates in each muon system and whether it is prescaled. The CMP-only muons are accepted on the $\not{E}_T$ trigger. 32

4.2 Summary of the electron selection criteria. 34

4.3 Cuts used to select and remove photon conversion electrons. 35

4.4 The selection criteria for muon candidates. 36

4.5 The selection criteria used to identify secondary lepton candidates from Z boson decays. 37

4.6 The number of events with at least one jet tagged by either the SVX or SLT algorithms. 43

6.1 The predicted and observed numbers of events along with the calculated background fractions and expected number of background events in each subsample. The totals for the tagged sample are also shown. 68

7.1 The percentage uncertainty on the relative jet energy correction for various detector η regions. 77
7.2 The approximate size of the uncertainties on the jet energy scale. 81
7.3 Systematic Uncertainties 86

B.1 The ΣP_T requirements for events selected from each jet trigger. 93

List of Figures

Figure

2.1 The approximate masses, in GeV/c^2, for the six known quarks: down (d), up (u), strange (s), charm (c), bottom (b), and top (t). 5

2.2 The tree-level Feynman diagram for top quark production by $q\bar{q}$ annihilation and standard model top quark decay. 10

2.3 The Feynman diagram for W+multijet production which is one of the backgrounds to the top signal. 11

2.4 The standard model predictions for various Higgs boson masses (indicated by the shaded bands) are shown as a function of the W mass (M_W) and the top quark mass (M_{top}). The width of the shaded bands is due primarily to the uncertainty in the electromagnetic coupling constant at the Z mass scale, $\alpha(M_Z)$, which has been assumed to be $\delta\alpha(M_Z) = 0.0004$. 13

3.1 Diagram of the Tevatron and its components. 15

3.2 A quarter sideview of the CDF detector. 17

3.3 A portrait of one of the SVX barrels. 19

3.4 Axial view of the CTC endplate showing the nine superlayer geometry. The wire planes are tilted 45° relative to the radial direction to account for the Lorentz angle of the ionization drift velocity. 20

3.5 Cutaway of a single central calorimetry wedge. 22

3.6 Geometry of the central calorimeter wedge and towers. The placement of the central muon chambers is also shown. 24

3.7 Transverse view of the central muon drift chambers. 26

4.1 The transverse mass of the lepton and missing energy for electron and muon events in the W candidate sample. 38

4.2 Schematic of a displaced vertex as reconstructed by the silicon vertex detector. 40

5.1 Counting constraints in the hypothesized $t\bar{t}$ decay system. 48

5.2 Distribution of fitted χ^2 for HERWIG Monte Carlo with $M_{top} = 175$ GeV/c^2. Events with $\chi^2 > 10.0$ are rejected. 51

5.3 The size of the standard corrections as a function of E_T for (a) the relative correction, (b) the absolute correction, (c) the underlying event correction, and (d) the out of cone correction. The corrections are derived for a jet with a cone size of 0.4 and $\eta = 0.7$. 54
5.4 Fractional correction applied to jets due to top specific jet-parton match and tagging information. The curves are for (A) jets from the W boson decay, (B) jets from b-quarks, (C) jets from b-quarks with an SLT-e tag, and (D) jets from b-quarks with an SLT-μ tag. 55
5.5 Average uncertainty in estimated parton P_T as a function of corrected jet E_T. The curves are for (A) jets from the W boson decay, (B) jets from b-quarks, (C) jets from b-quarks with an SLT-e tag, and (D) jets from b-quarks with an SLT-μ tag. 56
5.6 Reconstructed mass for HERWIG $t\bar{t}$ events (M_{top} = 175 GeV/c^2) with at least one tagged leading jet. The solid histogram shows the distribution for those events for which the selected jet-parton configuration was also the correct one. The hashed histogram shows the distribution for events where a correct assignment was ill defined. The cross hatched histogram shows the distributions for which a correct assignment could be defined but was not selected. 59
5.7 Reconstructed mass distribution for simulated background events from VECBOS Monte Carlo. 60

6.1 Fit to HERWIG Monte Carlo templates using the fit described in the text. . 64
6.2 Mean of the pull distributions for the 18 Monte Carlo $t\bar{t}$ templates. 65
6.3 Width of the pull distributions for the 18 Monte Carlo $t\bar{t}$ templates. 65
6.4 Fit to the VECBOS W+jet template. 66
6.5 Probability distribution for the expected number of background events and the corresponding negative log-likelihood. 69
6.6 The median fitted mass vs. the input mass for many samples of simulated experiments. 71
6.7 The pull distribution for a large number of pseudo experiments generated with M_{top} = 175 GeV/c^2. 71
6.8 Reconstructed mass distribution for the 34 tagged data events along with the results of the fit. The shaded region denotes the background contribution, while the solid curve is the result of the best fit combining the signal and background components. The inset shows the shape of the negative log-likelihood function. 73
6.9 Distribution of returned statistical errors in the Monte Carlo pseudo experiments. The arrow shows the returned statistical error for the data. 74

7.1 Uncertainty in jet E_T scale as measured within a jet clustering cone of size 0.4. The vertical axis shows the extent to which the measured jet E_T response varies due to different systematic effects. 78

7.2 Fractional jet E_T in annulus from data samples of W, Z, and γ events. . . . 79
7.3 Fractional jet E_T in annulus from $W+1$ jet events observed in data and from HERWIG Monte Carlo. 80
7.4 Reconstructed mass distributions for Pythia Monte Carlo with ISR and without ISR. 82
7.5 Reconstructed mass distributions for Pythia Monte Carlo for events with exactly 4 jets (no FSR) and events with more than 4 jets (extra jets from FSR). 83
7.6 Reconstructed mass distributions for VECBOS Monte Carlo generated with $Q^2 =< P_T^2 >$ and $Q^2 = M_W^2$ scales. 85

8.1 Measured top mass and W mass plotted along with the theoretical Higgs mass curves. 88

B.1 Run 1A relative correction. 95
B.2 Run 1B relative correction. 96
B.3 Run 1A corrected $\not{E}_T$projection fraction with additional corrections for $\eta = 0$ and $\eta = \pm 1.1$. 98
B.4 Run 1B corrected $\not{E}_T$projection fraction with additional corrections for $\eta = 0$ and $\eta = \pm 1.1$. 99
B.5 Run 1A corrected $\not{E}_T$projection fraction with additional corrections for $\eta = 0$ and $\eta = \pm 1.1$. 100
B.6 Run 1B corrected $\not{E}_T$projection fraction with additional corrections for $\eta = 0$ and $\eta = \pm 1.1$. 101

D.1 The reconstructed mass for VECBOS with $Q^2 = M_W^2$ and $Q^2 = P_T^2$. 106
D.2 The reconstructed mass for non-isolated lepton events (points) along with the VECBOS $Q^2 = P_T^2$ distribution (histogram). A KS test gives a 36% C.L. that they are the same. 107
D.3 The reconstructed mass for plug electron W events (points) along with the VECBOS $Q^2 = P_T^2$ distribution (histogram). A KS test gives a 33% C.L. that they are the same. 108
D.4 The reconstructed mass for W + loose jet events (points) along with the VECBOS $Q^2 = P_T^2$ distribution with loose jet cuts (histogram). A KS test gives a 45% C.L. that they are the same. 109
D.5 The reconstructed mass for Z + 4 jet events in the 1B data and a comparison of VECBOS Z + jet and W + jet Monte Carlo. A KS test yields an 85% C.L. that the latter two distributions are the same. 110

List of Appendices

Appendix

A. Useful Definitions 90

B. The Relative Jet Response 92
B.1 Data Sets 92
B.2 Method 94
B.3 Crosschecks 97

C. Background Shape Crosschecks 102
C.1 Backgrounds in the Mass Sample 102
C.2 W plus Jets Events 103
C.3 Conclusions 105

Chapter 1

Introduction

The mass of the top quark has long been a parameter of interest, even before the top quark was actually discovered. This was due to the fact that although the top quark was predicted by theoretical models, its mass was not. Finding the top quark was closely coupled to the value of its mass. The larger its mass, the harder it was to produce and hence to observe. As experimental searches for the top quark were carried out, limits were set for the top mass. Searches by the UA1 collaboration at the CERN $p\bar{p}$ collider set a lower limit of 44 GeV/c^2 [1]. This was extended by searches at the Tevatron to a lower limit of 91 GeV/c^2 and 131 GeV/c^2 by the CDF and D0 collaborations respectively [2, 3]. Experimenters at the Fermilab Tevatron proton-antiproton collider finally confirmed the existence of the top quark in 1995 [4, 5]. This dissertation describes one method used by the CDF collaboration to measure the mass of the top quark.

Since the discovery of the top quark, its mass has been measured in each of the W decay channels; all-hadronic, dilepton and lepton+jets. In the all-hadronic mode each event consists of 6 jets, two from the b quarks and 4 from the hadronic decay of the W bosons. This channel has the advantage of having a one to one correspondence between the top decay partons and the experimentally observed jets. The disadvantage of this channel is the large QCD+multijet background which makes it difficult to isolate top events from background events. The all-hadronic mass measurement is described in detail elsewhere [6]. Measuring the top quark mass from dilepton decays is particularly challenging due to the

presence of two neutrinos in the final state. The signature of a dilepton event is two jets from the b quarks, and two leptons and a large amount of missing energy from the leptonic decay of the W bosons. Since the energy of the neutrinos must be inferred from the total amount of missing energy in the detector, an individual event does not contain sufficient information to solve for a unique top mass. Additional outside information must be used when fitting dilepton events to a top mass [7]. Presently, the most accurate techniques for measuring the top mass at Fermilab use the lepton+jets channel. In the lepton+jets mode, the $t\bar{t}$ event can be completely reconstructed, as in the all-hadronic mode, but with a much higher purity for top events. Previous measurements from CDF in the lepton+jets channel can be found elsewhere [8] [9]. This thesis presents a measurement of the top quark mass on events in lepton+jets channel.

The Standard Model is summarized in Chapter 2 with specific attention given to aspects relating to the top quark production and decay. Chapter 3 gives a brief description of the apparatus, the CDF detector, used to collect the data for this thesis. The selection requirements used to identify $t\bar{t}$ candidate events are described in Chapter 4. Chapter 5 explains the details involved in reconstructing individual events to the $t\bar{t}$ hypothesis. Description of the method used to determine the final top mass measurement is detailed in Chapter 6. In Chapter 7, the techniques used to evaluate the systematic error on the measurement of the top mass are described. Finally, the conclusions are given in Chapter 8.

Chapter 2

Theory

At the present time, the Standard Model [10] provides the best understanding of the fundamental constituents of matter and how they interact. This theoretical model has been tested to the level of a few tenths of a percent over a large range of energies and provides a remarkably precise description of the subnuclear world over distance scales of several orders of magnitude. One of the strengths of the Standard Model is its predictive power. Over the years, many of its predictions have been confirmed by experimental data. One such prediction was the existence of a sixth quark type, called the top quark. This prediction was verified in 1995, when the top quark was discovered by two separate high energy physics experiments at Fermi National Accelerator Laboratory (Fermilab).

In the Standard Model, there are a number of free parameters, most of which are masses, which must be obtained from experimental measurements. In particular, it does not predict the masses of the fermions. They must be input into the theory. The predictive power of the Standard Model depends upon how precisely the relevant input parameters are known. For instance, the Higgs boson mass is constrained by the measured W boson and top quark masses via electroweak radiative corrections.

While the Standard Model has been quite successful, it should be pointed out that it does have some shortcomings. For instance, it does not predict how many generations of quarks and leptons exist. So far, three generations have been observed but the Standard Model could accommodate more. Further, it provides no explanation for differences in the

masses of the observed fermions. Figure 2.1 shows the six known quarks and their mass. In particular, it gives no fundamental reason for the top quark to be so much heavier than the other quarks. New theories which extend the Standard Model have been proposed, but the Standard Model remains the only theory verified by experimental data. Because the agreement between measurements and the Standard Model predictions, only new theories that incorporate the Standard Model as a subset are generally being considered.

			Q	**Forces**
Leptons				
$\begin{pmatrix} e \\ \nu_e \end{pmatrix}$	$\begin{pmatrix} \mu \\ \nu_\mu \end{pmatrix}$	$\begin{pmatrix} \tau \\ \nu_\tau \end{pmatrix}$	$\begin{pmatrix} -1 \\ 0 \end{pmatrix}$	$\begin{pmatrix} \text{EM, Weak} \\ \text{Weak only} \end{pmatrix}$
Quarks				
$\begin{pmatrix} u \\ d \end{pmatrix}$	$\begin{pmatrix} c \\ s \end{pmatrix}$	$\begin{pmatrix} t \\ b \end{pmatrix}$	$\begin{pmatrix} +2/3 \\ -1/3 \end{pmatrix}$	$\begin{pmatrix} \text{EM, Weak} \\ \text{and Strong} \end{pmatrix}$

Table 2.1: The six fermions (leptons and quarks) currently known along with their electric charge, Q, and the forces via which they interact.

2.1 Standard Model

In the Standard Model there are three kinds of fundamental particles which interact via four forces. The fundamental particles are leptons, quarks, and gauge bosons. The forces governing their interactions are the strong force, the weak force, electromagnetism, and gravity. Gravity is not incorporated into the Standard Model. Each of the particles has an anti-particle which has identical mass and spin, but opposite quantum numbers. As an example, the negatively charged electron (e^-) has the positively charged positron (e^+) as its anti-particle. The known quarks and leptons are shown in Table 2.1.

There are six types of leptons which are grouped into three families. Each family consists of a charged lepton and its associated neutrino. The charged leptons are the electron (e), the muon (μ), and the tau (τ). Each carry an electric charge of -1 and have mass with the electron being the lightest and the tau the heaviest. The electron (ν_e), muon (ν_μ), and tau (ν_τ) neutrinos are electrically neutral and consistent with having zero mass. Leptons

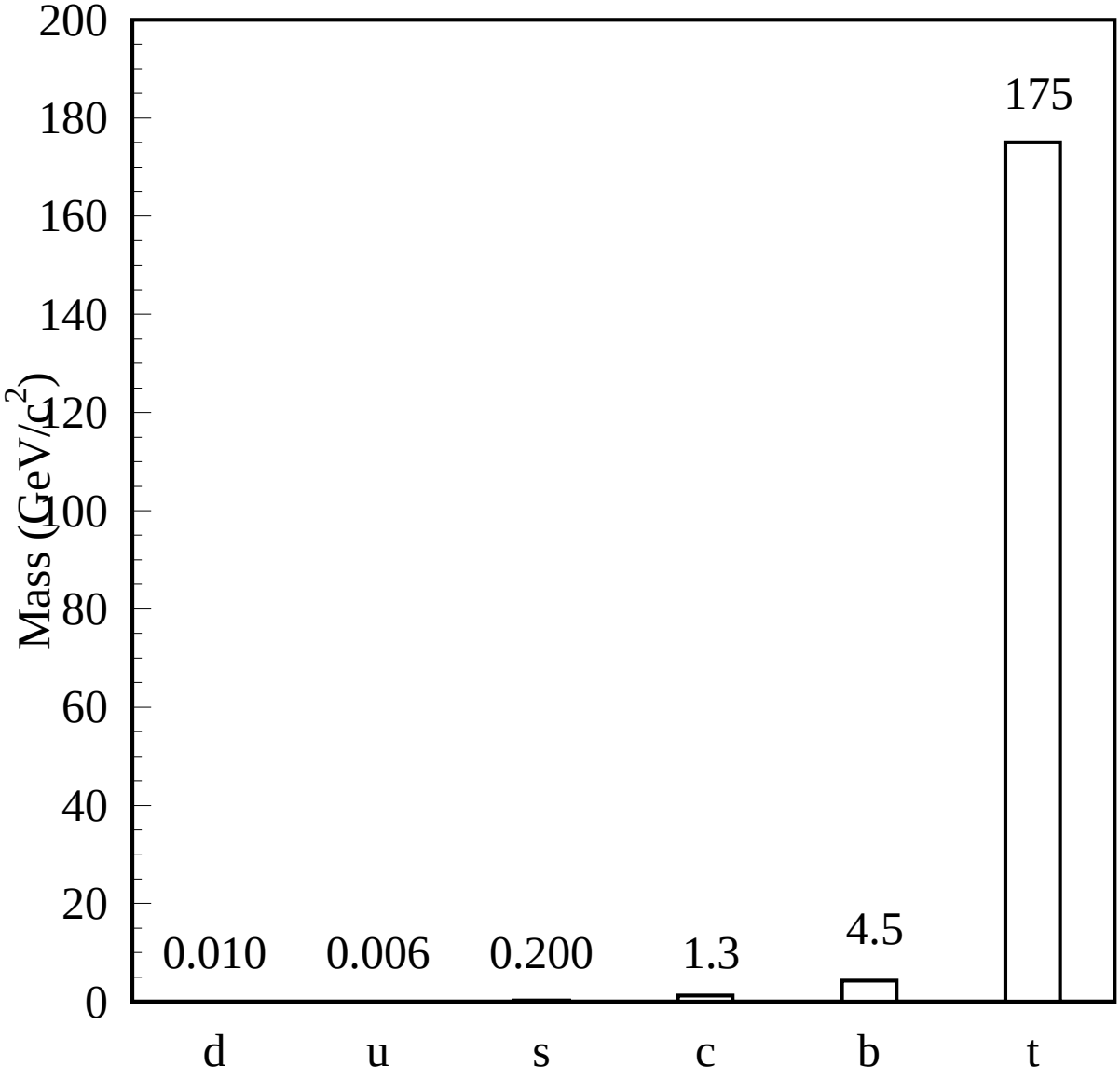

Figure 2.1: The approximate masses, in GeV/c^2, for the six known quarks: down (d), up (u), strange (s), charm (c), bottom (b), and top (t).

Gauge Bosons	**Force**	**Coupling (α)**
Photon (γ)	Electromagnetic	10^{-2}
W^+, W^-, Z^0	Weak	10^{-13}
Gluon (g)	Strong	1

Table 2.2: The gauge bosons known in the Standard Model. The coupling constant (α) is given as the strength in comparison to the strong force at 10^{-13} cm, the approximate radius of the proton.

all possess half integer spin and obey Fermi-Dirac statistics, hence they are referred to as fermions. In the Standard Model, they only interact via the electromagnetic or weak forces. The three families of leptons and their associated electric charge, Q, are shown in Table 2.1. Also shown are the forces with each type of particle interacts.

The quarks are also fermions. They come in 6 flavors, referred to as up (u), down (d), charm (c), strange (s), top (t), and bottom (b). The quarks are arranged in three families of weak isospin doublets. Each quark carries an electric charge which is equal to a precise fraction of an electron's charge. Table 2.1 illustrates the families of quarks and their electric charges. Unlike the leptons, quarks experience strong interactions in addition to electromagnetic and weak interactions. Besides electric charge, each quark also carries a "color" charge labeled red, green or blue for reference. In the strong force, the color charge is analogous to the electric charge of the electromagnetic force but very different in its detailed properties.

The last group of fundamental particles are the gauge bosons. They are called bosons because they have integral spin and obey Bose-Einstein statistics. In the Standard Model, the gauge bosons are the mediators of the forces. The electromagnetic force is mediated by the photon. The strong force is mediated by eight gluons and the weak force is mediated by three vector bosons, W^+, W^- and Z°. A measure of the strength of a force is given by its coupling constant, α. Table 2.2 lists the mediators and coupling constants for the three forces described by the standard model.

The strong force binds quarks together to form hadrons. In general, two types of

hadrons can be formed: mesons and baryons. The mesons are made up of a quark and anti-quark pair. As such they have integral spin and behave as bosons. A common meson, the π^- is composed of a d quark and a $\bar{u}$ quark. Baryons are formed from either three quarks or three anti-quarks. The baryons have half integer spins and are thus fermions. The proton is a baryon comprised of two u quarks and a d quark. The quarks always form combinations such that the resulting electric charge is an integer and the sum of the color charges is neutral. That is, a meson must contain a colored quark and an anti-colored anti-quark of the same color. A baryon must consist of red, blue, and green quarks or the analogous anti-colored anti-quarks.

The standard model uses gauge theories to mathematically describe how the forces interact with the fundamental particles. Gauge theories are a special class of quantum field theories in which an invariance principle necessarily requires the existence of interactions among the particles. The gauge theory of electromagnetism, called Quantum Electrodynamics (QED), describes the photon-mediated interactions of electrically charged particles. The electromagnetic force is proportional to $1/r^2$, where r is the distance between the interacting particles, and its range is infinite. In QED the electric charge of an interaction must be conserved. Quantum Chromodynamics (QCD), which is modeled after QED, describes the gluon-mediated strong interactions of quarks. The strong force is independent of r, so as quarks move further and further apart, the potential energy stored in the field between them increases indefinitely. Like QED, for which electric charge must be conserved, color must be conserved in QCD. Since the quarks carry only one color and color must be conserved, the gluon mediators must carry a color and an anti-color. For example, a gluon may carry red and anti-green.

In the Standard Model, the gauge theories of the electromagnetic and weak forces have been combined into a single structure called the Electroweak theory. This unification implies that at very short distances and high energies, the weak and electromagnetic forces have a common coupling constant. The Electroweak theory predicts four massless gauge bosons, the W^+, W^-, Z° and the photon (γ). To account for the fact that the W^+, W^-,

and Z° bosons are massive, an additional scalar field, the Higgs, was postulated. In the framework of the Standard Model, particle masses arise as a consequence of coupling to the Higgs field. As of yet, the Higgs has not been experimentally observed.

2.2 Proton Anti-proton Collisions

Protons (p) and antiprotons ($\bar{p}$) consist of three quarks called the valence quarks. The proton's valence quarks are uud and the antiproton's valence quarks are $\bar{u}\bar{u}\bar{d}$. Other quarks are continually being created and destroyed inside the proton and antiproton. These quarks are called the "sea" quarks. The sea quarks appear as virtual $q\bar{q}$ pairs, being quickly created and annihilated in the vacuum. The proton also consists of a sea of gluons which bind the proton together. Quarks and gluons are sometimes referred to as partons since they are "part" of the proton. At high enough collision energies, the partons of the proton and antiproton are what interact with the non-interacting partons behaving more or less as spectators.

In a high-energy proton-antiproton ($p\bar{p}$) collision, a quark (or gluon) from a proton scatters off a quark (or gluon) from the antiproton. As the partons move apart the field energy between them increases. Eventually this field energy becomes large enough to create a $q\bar{q}$ pair from the vacuum. These new quarks recombine with themselves and with the original quarks to produce hadrons. Quark anti-quarks pairs are continually created until the original interaction energy is converted into hadrons. This process, called hadronization, produces a large number of particles which are observed experimentally as a jet. The direction of a jet will be approximately collinear with the parton that initiated it.

Most $p\bar{p}$ collisions involve low energy parton scattering. Occasionally an interaction involving large momentum transfer occurs. Only the large momentum transfer interactions are able to produce $t\bar{t}$ pairs. In top quark production, the initial partons collide and form a $t\bar{t}$ pair. Subsequently, the top quarks decay and form jets in the detector. In addition to the $t\bar{t}$ pair, gluons are often emitted from the initial or final state partons. Since gluons carry color, they must also hadronize and produce additional jets in the event. This process

is labeled initial or final state radiation depending on the parton from which the gluon radiates.

In $p\bar{p}$ collisions, the component of the initial momenta parallel to the beampipe, the z momenta, of the valence quarks and the composition of the proton sea is unknown. Therefore, the z momenta of the initial partons is also unknown. However, the components of the momenta which are perpendicular to the beampipe, the transverse momenta, of the initial partons are very close to zero because the initial partons have small momenta in the rest frame of the proton.

2.3 Top Quark Production and Decay

In $p\bar{p}$ collisions, $t\bar{t}$ pairs can be produced by either $q\bar{q}$ annihilation or gluon-gluon fusion. For large top masses (greater than 100 GeV/c^2) and center of mass energy near $\sqrt{s}$ = 1.8 TeV, $q\bar{q}$ annihilation is expected to be the dominant production process. In the Standard Model, the top quark decays almost exclusively to a W boson and a b quark. Other decays are possible, but they involve off diagonal elements of the Cabibbo-Kobayashi-Maskawa (CKM) matrix which are very close to zero. The CKM matrix determines how quarks mix in their coupling to the W. The resulting W boson from the top decay will then decay into either a lepton and its neutrino or a $q\bar{q}'$ pair. The Feynman diagram for the expected top quark production and decay is shown in Figure 2.2.

The manner in which the two W bosons decay determines a $t\bar{t}$ event's topology. The possible final states are listed in Table 2.3. Events in which both W's decay to quark-antiquark pair are called "all-hadronic" decays. The signature for this decay is six or more jets. Though this channel has the largest branching fraction at 44%, it has an enormous amount of background from other QCD multijet production processes. This channel has been studied elsewhere [6]. Events in which both W's decay leptonically to an e or μ are labeled "dilepton" decays. The signature of this channel is two high P_T leptons and large missing transverse energy from the undetected neutrinos along with two jets from the b

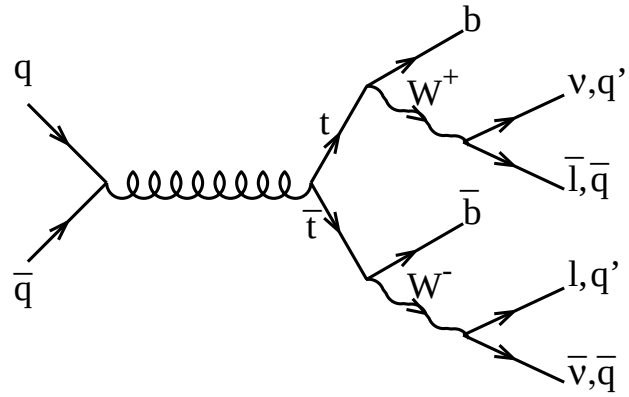

Figure 2.2: The tree-level Feynman diagram for top quark production by $q\bar{q}$ annihilation and standard model top quark decay.

Decay Mode	Branching Ratio
$t\bar{t} \to (q\bar{q}\prime b)(q\bar{q}\prime\bar{b})$	36/81
$t\bar{t} \to (q\bar{q}\prime b)(e\nu\bar{b})$	12/81
$t\bar{t} \to (q\bar{q}\prime b)(\mu\nu\bar{b})$	12/81
$t\bar{t} \to (q\bar{q}\prime b)(\tau\nu\bar{b})$	12/81
$t\bar{t} \to (e\nu b)(\mu\nu\bar{b})$	2/81
$t\bar{t} \to (e\nu b)(\tau\nu\bar{b})$	2/81
$t\bar{t} \to (\mu\nu b)(\tau\nu\bar{b})$	2/81
$t\bar{t} \to (e\nu b)(e\nu\bar{b})$	1/81
$t\bar{t} \to (\mu\nu b)(\mu\nu\bar{b})$	1/81
$t\bar{t} \to (\tau\nu b)(\tau\nu\bar{b})$	1/81

Table 2.3: Branching ratios for $t\bar{t}$ decay modes assuming standard model couplings. Here q stands for a u, d, c or s quark.

quarks. The two neutrinos in these events make it impossible to completely reconstruct the $t\bar{t}$ decay. The dilepton decays have been studied elsewhere [7].

With the goal of reconstructing $t\bar{t}$ decays, the events in which one W decays to a lepton-neutrino pair and the other W decays hadronically offer a number of advantages. These events are termed lepton+jets events. The signature for this channel is a charged lepton with high transverse momentum ($\mathrm{P_T}$), missing energy from the undetected neutrino, and four or more jets from the hadronized quarks. Decays of W bosons to τ leptons

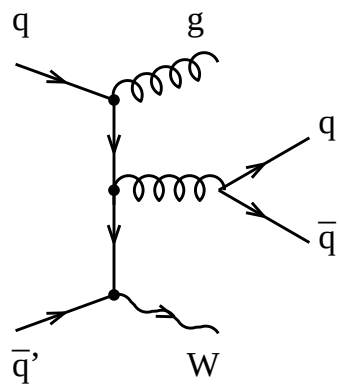

Figure 2.3: The Feynman diagram for W+multijet production which is one of the backgrounds to the top signal.

are not explicitly included in this analysis (except when they subsequently decay to an electron or a muon) because of the difficulties associated with identifying the hadronic decays of τ leptons. Requiring one of the W bosons to decay leptonically to an e or μ substantially reduces the amount of background without significantly reducing the signal detected, $\sim 30\%$. The primary background to the lepton+jets channel comes from higher-order production of W bosons, where the W recoils against significant jet activity. This is referred to as "W+multijet" background. Figure 2.3 shows one of the Feynman diagrams for QCD W+multijet production. The fact that only one neutrino is present allows complete reconstruction of these events.

As previously mentioned, this analysis only considers the Standard Model decay $t \to Wb$, so every top event is assumed to have two b quarks. The W+multijet background in the lepton+jets channel can be greatly reduced by identifying, or "b-tagging", at least one of the b quarks in the event. Two different methods of b-tagging are used in this analysis. The first method utilizes the b's lifetime of $\sim$ 1.5 ps. This long lifetime means that the b quark will form a B hadron and travel on average a few millimeters before decaying. B hadrons can be detected experimentally by looking for jets with vertices displaced from the primary vertex of the event. The second technique is to search in the event for additional leptons coming from the semileptonic decays of B hadrons.

2.4 Top Mass

The top quark is a recently discovered fundamental particle whose properties should be measured to the greatest precision possible. One property, the top quark mass (M_{top}), is an important standard model input parameter. It enters into calculations of radiative corrections which connect several other standard model parameters. By measuring the top mass very accurately, global fits combining M_{top} and other experimental information can be used to test for consistency and predict unknowns of the standard model. At the present time, one of the most pertinent predictions which can be made is the unknown mass of the Higgs boson, M_H. Direct, precision measurements of the mass of the W boson (M_W) and of the top quark (M_{top}), provide an indirect constraint on the Higgs boson mass, M_H, via top quark and Higgs boson electroweak radiative corrections to M_W. Figure 2.4 shows the standard model predictions for various Higgs boson masses (indicated by the shaded bands) as a function of M_W and M_{top}.

Previous direct measurements of the top mass in the lepton+jets channel at CDF obtain a value of $\sim$ 175 GeV/c^2 [8] [9]. In the limit $M_{top} >> M_b$, $M_W >> M_b$, and assuming only three generations of quarks ($|V_{tb}| = 1$) the partial width for the decay ($t \rightarrow Wb$) is given by [11]

$$\Gamma(t \rightarrow Wb) \approx 175\ MeV \left(\frac{M_{top}}{M_W}\right)^3 \tag{2.1}$$

A top quark with mass 175 GeV/c^2 is expected to have a width of nearly 2 GeV and a lifetime of $\sim 4 \times 10^{-25}$ seconds. This means that the top quark travels only $\sim$ 0.04 fm before it decays. The current theory hypothesizes that hadronization does not occur before the outgoing quarks are more than $\sim$ 1 fm apart. At this distance, the stretched color string is expected to break producing $q\overline{q}$ pairs out of the vacuum which can combine with the quarks to form hadrons. Since the top quark travels $<$ 1 fm, it is expected to decay before forming a hadron. However, because the top is so heavy, the decay of a free top quark and a top hadron are not expected to be differentiable in current experiments [12].

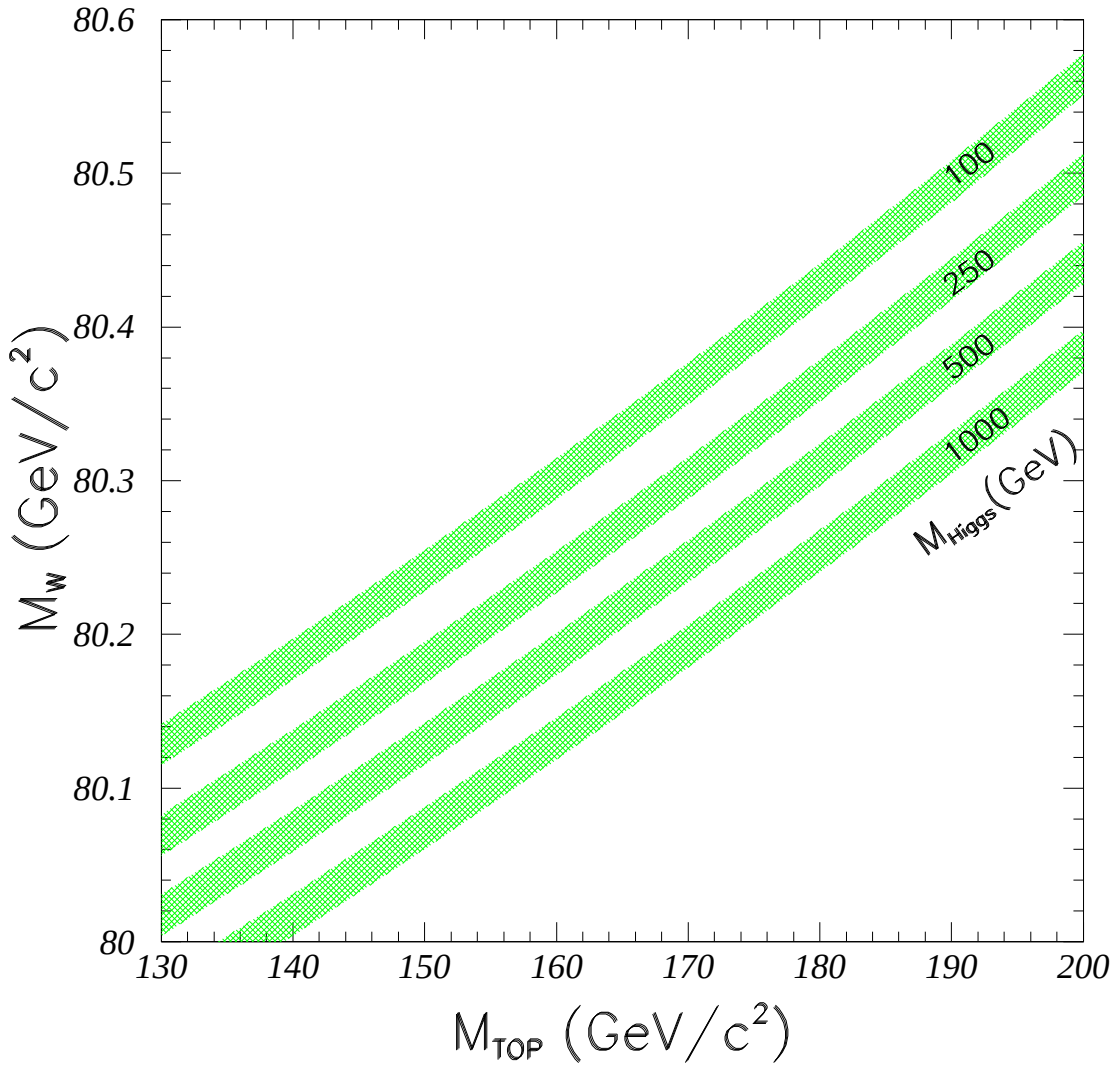

Figure 2.4: The standard model predictions for various Higgs boson masses (indicated by the shaded bands) are shown as a function of the W mass (M_W) and the top quark mass (M_{top}). The width of the shaded bands is due primarily to the uncertainty in the electromagnetic coupling constant at the Z mass scale, $\alpha(M_Z)$, which has been assumed to be $\delta\alpha(M_Z) = 0.0004$.

Chapter 3

Experimental Apparatus

The data for this analysis was collected using the two distinct components. The first is the Tevatron, a synchrotron accelerator at the Fermi National Accelerator Laboratory (Fermilab) that collides beams of protons (p) and anti-protons ($\bar{p}$) at a center-of-mass energy of 1.8 TeV. The second is the Collider Detector at Fermilab (CDF), a general-purpose detector designed to study the results of the $p\bar{p}$ collisions. This chapter describes both components. First, the Tevatron and the associated devices used to generate and accelerate the colliding beams are described. Next is a description of the CDF detector used to collect the data from interesting events.

3.1 The Tevatron

The Tevatron operates with six bunches of 900 GeV protons colliding with six bunches of 900 GeV anti-protons [13]. Figure 3.1 is a diagram of the accelerator and its components. A number of steps are needed to produce 900 GeV bunches of protons and anti-protons. The protons begin as negatively charged hydrogen ions, composed of two electrons and one proton. They are accelerated to 750 keV by a Cockroft-Walton accelerator (not shown in Figure 3.1), and then enter a 150 m linear accelerator, the Linac, which accelerates them to an energy of 200 MeV. The electrons are stripped from the H^- ions by passing them through a carbon foil and the beam is passed to the Booster, a 480 m

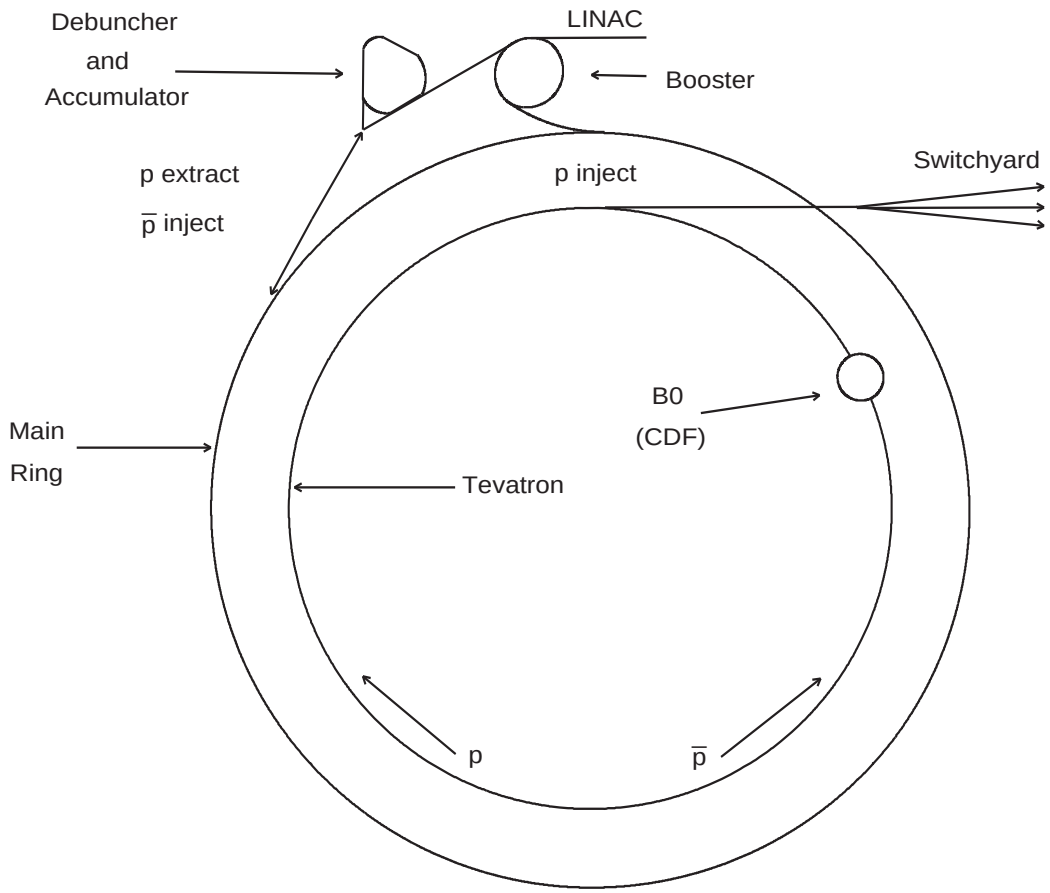

Figure 3.1: Diagram of the Tevatron and its components.

circumference synchrotron, which accelerates the protons to 8 GeV. The protons then enter the Main Ring, a 6.3 km synchrotron. Here the protons are accelerated to an energy of 150 GeV, before being injected into the Tevatron for acceleration to a final energy of 900 GeV. Though shown separately in Figure 3.1, the Main Ring and the Tevatron lie atop one another in the same 1 km radius tunnel.

The process of obtaining the anti-proton beam is a bit more complex. A 120 GeV beam of protons is extracted from the Main Ring and strikes a copper target to create antiprotons. The antiprotons which emerge from the proton-nucleus collisions have a large

momentum spread. A magnetic field is used to focus and collect them. The antiprotons are then passed to the Debuncher where they are stochastically cooled to reduce the phase space of the beam. Out of the Debuncher the antiprotons are passed to the Accumulator, where they are stored. The anti-protons are stored at a rate of 4×10^{10} per hour over a number of hours until a sufficient number have been stored.

To begin collisions, six bunches of protons are injected into the Tevatron. After this, six bunches of anti-protons are taken from the Accumulator and reverse injected into the Main Ring. Once the anti-protons bunches reach an energy of 150 GeV, they are injected into the Tevatron circulating in the opposite direction of the protons. Though the protons and anti-protons travel in the same beam pipe, their densities are too low to cause many collisions. The final step is too focus the beams to collide. There are two interaction regions at the Tevatron, B0 and D0. In these regions, the beams are made to collide by focusing them with quadrapole magnets. The beams typically collide for around 10 hours. During this time, anti-protons are stacked using the Main Ring.

The data used in this analysis were collected during two periods. The first period, referred to as Run Ia, extended from June 1992 to May 1993. Approximately 20 pb^{-1} of data was accumulated during this period. The second period, Run Ib, extended from September 1993 to February 1996. The period produced approximately 90 pb^{-1} of data. The total integrated luminosity for Run I is $109 \pm 7\text{pb}^{-1}$. See Appendix A for details of luminosity calculation.

3.2 The CDF Detector

The CDF detector is a multipurpose detector designed to study high energy $p\bar{p}$ collisions [14]. A quarter view schematic drawing of the detector is shown in Figure 3.2. CDF is cylindrically and forward backward symmetric about the interaction point.

The coordinate system used by CDF is pictured in the upper left corner of Figure 3.2. It is centered on the interaction point, with the positive z axis along the beamline in the direction of the protons, the x axis toward the center of the ring, and the y axis straight

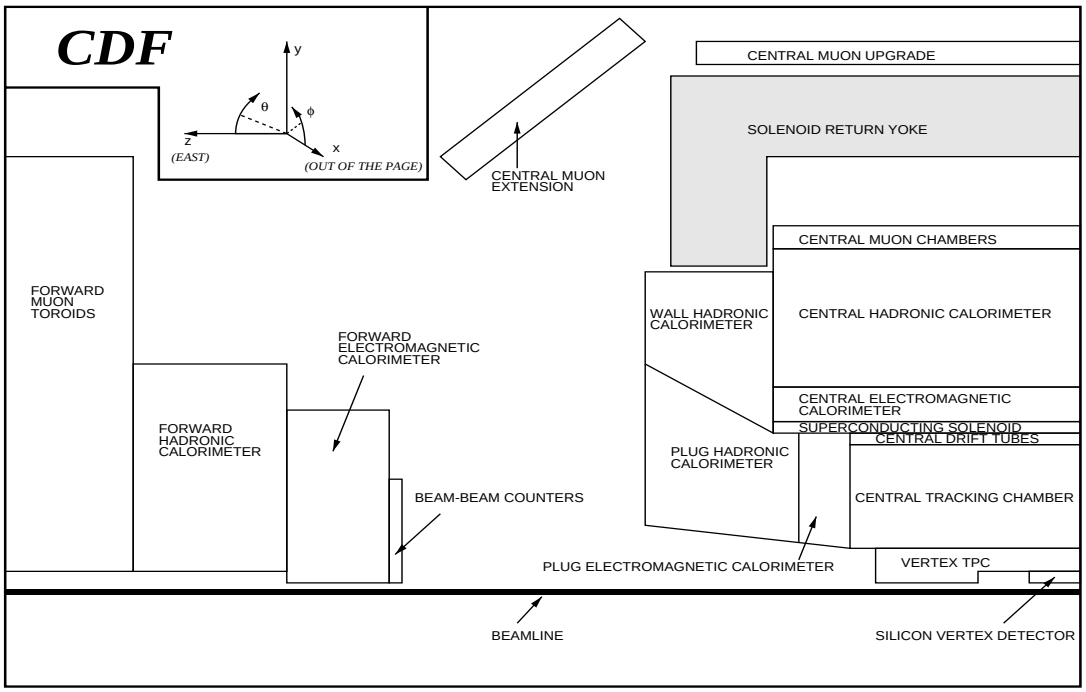

Figure 3.2: A quarter sideview of the CDF detector.

up. The azimuthal angle (ϕ) is defined with respect to the x axis, while the polar angle (θ) is defined with respect to the z axis. Appendix A contains definitions for common terms which will be used throughout the remainder of this dissertation.

The design of the CDF detector is dictated by the behavior of different types of particles. CDF is composed of a variety of smaller detector elements which are designed to function as a whole. It can be viewed as being made up of three fundamental types of components: tracking chambers, calorimetry, and muon chambers.

3.3 Tracking Detectors

The system for tracking charged particles at CDF consists of three components: the silicon vertex detector (SVX), the vertex drift chamber (VTX), and the central tracking

chamber (CTC). All three lie inside a 1.4 Tesla solenoidal magnet of length 4.8 m and radius 1.5 m. The solenoid provides the ability to measure the momentum of charged tracks. The SVX is designed to give precise tracking around an event interaction point, its "vertex", and to identify secondary vertices resulting from the decay of long-lived particles. The VTX provides z position information on tracks and is used to identify the z position of the interaction vertex. The CTC is designed to provide a precise momentum measurement of a charged track.

3.3.1 SVX

The SVX is a silicon microstrip detector designed to provide precision $r-\phi$ tracking near the interaction region [15]. The detector consists of two cylindrical barrels positioned end-to-end along the beampipe. There is a 2.15 cm gap between the barrels at z=0. A schematic of one barrel is shown in Figure 3.3. Each barrel is divided into 12 azimuthal wedges of 30° each with four concentric layers. The innermost layer, layer 0, is 2.86 cm from the beampipe, while the outermost layer, layer 3, is 7.87 cm from the beampipe. The pitch of the strips is 60 μm on the three inner layers and 55 μm on the outer layer. The single hit resolution per layer is approximately 13 μm with a 96% hit efficiency per layer. Each barrel extends $\pm$ 25 cm from the interaction point. Since the Tevatron interaction region has a width of approximately 30 cm along the z axis, the geometric acceptance of the SVX is about 60%.

The basic element of the SVX is the ladder. Each 30° wedge contains four 25.5 cm ladders, one for each layer. Each ladder has three 8.5 cm long single-sided silicon strip detectors with readout strips attached to the outside ends (see Figure 3.3). Each ladder is rotated by 3° about its longitudinal axis to allow an overlap between neighboring ladders. The SVX has a total of 96 ladders. They are readout by custom chips with each chip responsible for 128 channels (strips). There are a total of 46080 channels for the entire SVX detector. This is nearly one third of all the readout channels for the CDF detector. The

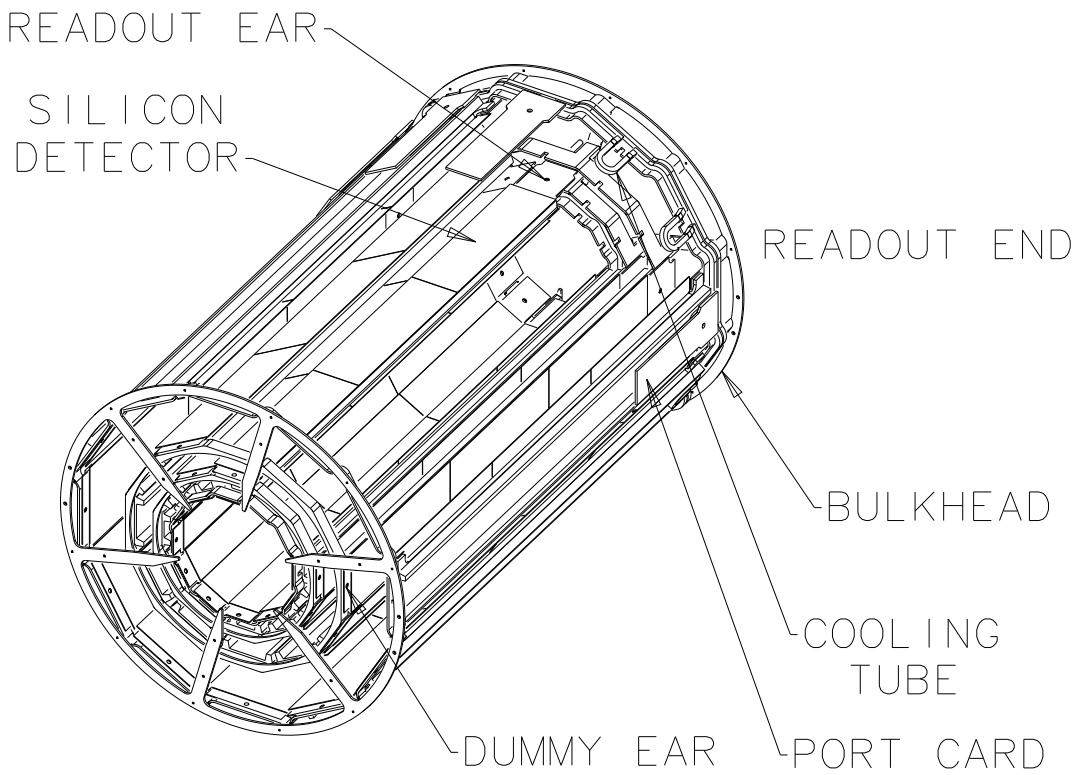

Figure 3.3: A portrait of one of the SVX barrels.

channels are read out in sparse mode meaning only the channels which register a hit are read out. In a typical event, about 5% of the channels are read out.

3.3.2 VTX

At the high luminosities provided by the Tevatron, there is often more than one interaction per crossing. The VTX is used to associate each track to the correct vertex along the beamline. It is made up of an octogon of eight gas chambers outside the SVX. The detector is 2.8 m long with an inner radius and outer radius of 8 cm and 22 cm respectively from the beampipe. The sense wires in the chambers run transverse to the beamline to

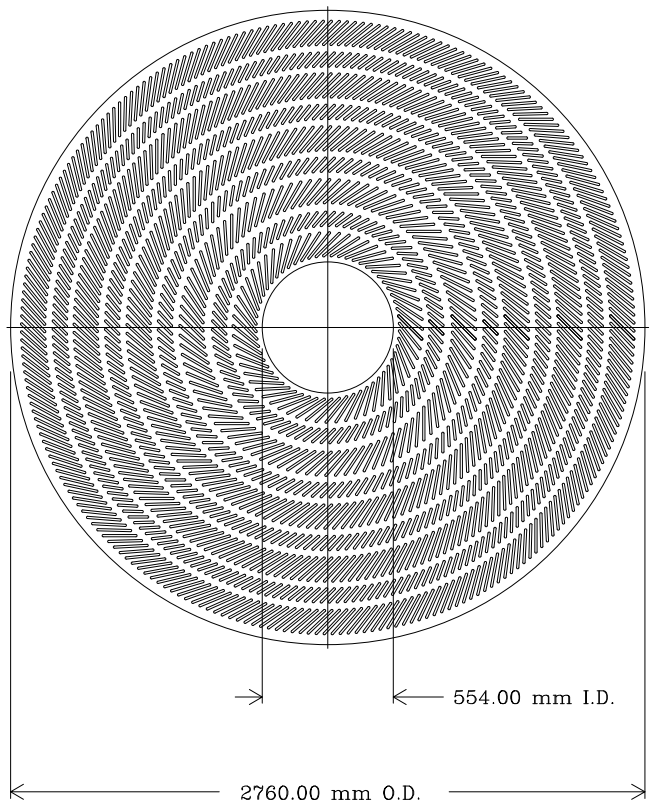

Figure 3.4: Axial view of the CTC endplate showing the nine superlayer geometry. The wire planes are tilted 45° relative to the radial direction to account for the Lorentz angle of the ionization drift velocity.

provide tracking information in the $r - z$ plane. Charged particles passing through the chambers produce free electrons which drift in the axial direction to the sense wires. The location of the wire determines the r information, while the time of arrival determines the z position. The uncertainty on the measurement of the z position of a vertex is about 1 mm.

3.3.3 CTC

The CTC is a large cylindrical open-wire drift chamber. It is used to measure a charged particle's momentum by determining its curvature in the 1.4 T magnetic field. The

CTC is 3.2 m long with an inner radius of 0.3 m and and outer radius of 1.3 m. It is composed of field and sense wires which are arranged into cells containing 6 or 12 sense wires each. The cells are combined to form nine superlayers. Each cell, consisting of a plane of sense wires, is tilted at an angle with respect to the radial direction such that wires from neighboring cells will overlap. Five axial superlayers, comprised of cells of 12 sense wires each, run parallel to the beamline. These are alternated with four stereo superlayers, comprised of cells of 6 sense wires. The stereo layers are rotated at an angle of 3° with respect to the beamline in order to provide z position information for the tracks. Figure 3.4 shows an axial view of the CTC endplate. The nine layers of the CTC can be seen, with the smaller cells being the 6 wire cells of the stereo superlayers, while the larger cells are the 12 wire cells of the axial superlayers.

Tracks are reconstructed by fitting measured hits in the CTC to a helix. The curvature of the track is dependent upon the transverse momentum of the particle. The momentum resolution for the CTC is:

$$\delta P_T/P_T = 0.002 \text{ GeV}^{-1} \times P_T \tag{3.1}$$

The P_T resolution on a track can be improved by including the SVX hits associated with the track. This improves the resolution to:

$$\delta P_T/P_T = 0.001 \text{ GeV}^{-1} \times P_T \tag{3.2}$$

3.4 Calorimetry

There are two types of calorimetry in the CDF detector: electromagnetic, and hadronic. Both types consist of alternating layers of absorbing material and active material. The absorbing material causes particles to interact and produce showers of secondary particles. The active material measures the original particles energy by sampling the resultant energy flow as a function of depth. Because electromagnetic showers develop faster, the electromagnetic calorimeters are placed in front of the hadronic calorimeters. The calorimeter

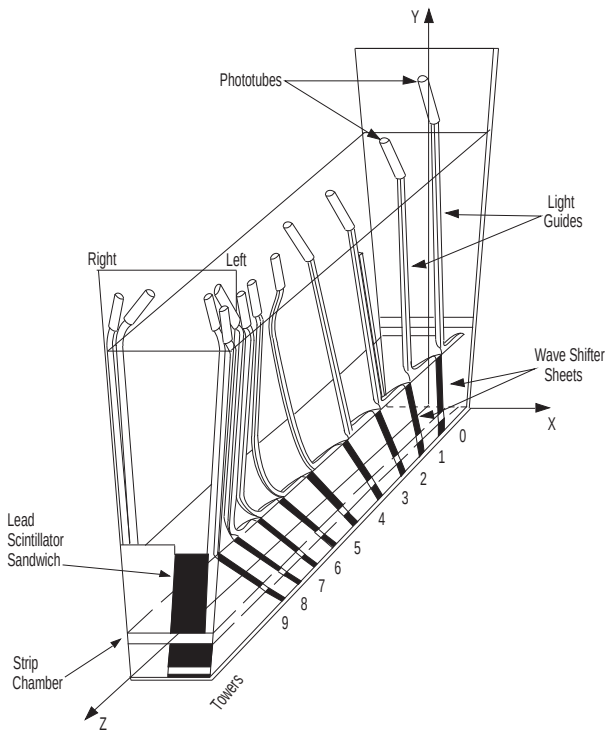

Figure 3.5: Cutaway of a single central calorimetry wedge.

system is used to measure the energy and direction of jets and electromagnetic particles, determine the amount of missing energy in an event, and aid in the identification of electrons, photons, and muons.

Physically, the calorimeters surround the solenoid and tracking chambers. They cover a range of 2π in azimuth and -4.2 to 4.2 in pseudorapidity. The calorimeters are segmented into towers in $\eta - \phi$ space such that each tower points back to the center of the detector (interaction point). It consists of three subsystems which cover different pseudorapidity regions: the central ($|\eta| < 1.1$), the plug ($1.1 < |\eta| < 2.4$), and the forward ($2.4 < |\eta| < 4.2$) calorimeters.

3.4.1 Central Calorimeter

The central electromagnetic (CEM) and hadronic (CHA) calorimeters are segmented in towers of 15° in azimuth and 0.1 units in pseudorapidity. Each 15° section is referred to as a wedge. Particles in the region $0.6 < |\eta| < 1.1$ do not pass through all layers of the CHA. For this reason, an additional hadronic calorimeter, the endwall hadronic calorimeter

	Electromagnetic (CEM)	Hadronic (CHA/WHA)
Coverage (η)	$0 - 1.1$	$0 - 0.9/0.7 - 1.3$
Tower Size ($\delta\eta \times \delta\phi$)	$0.1 \times 15°$	$0.1 \times 15°$
Active Medium	polystyrene scintillator	acrylic scintillator
Absorber	Pb	Fe
Interaction Length	18 X_0	4.5 λ_0
Energy Resolution	$13.7\%/\sqrt{E_T} \oplus 2\%$	$50\%/\sqrt{E_T} \oplus 3\%$

Table 3.1: Characteristics of central and endwall calorimeters. Interaction lengths are given in radiation lengths (X_0) and absorption lengths (λ_0). The two components of the energy resolution are added in quadrature. The electromagnetic resolution is for isolated is for isolated electromagnetic particles and the hadronic resolution is for isolated pions.

(WHA), was added. Particles traversing the calorimeter produce light in the scintillator which is collected by acrylic lightguides and transmitted to photomultiplier tubes located at the back of each wedge. A cutaway diagram of a central calorimeter wedge is shown in Figure 3.5.

The CEM contains 18 radiation lengths of material, and the CHA has 4.5 absorption lengths of material beyond the CEM. The geometric layout of the central calorimetry is displayed in Figure 3.6. To determine the energy resolution, the CEM was calibrated with testbeam electrons. The energy resolution for hadronic showers was measured from isolated pions. The measured energy resolutions and other details of the calorimeters are in Table 3.1. The energy resolutions for isolated particles have two components, one energy dependent and one constant which are added in quadrature.

To aid in precise measurements of electromagnetic showers, a proportional strip and wire chamber (CES) is embedded in the CEM at the expected position of maximum shower deposition (about 6 radiation lengths). The position resolution of the CES for 50 GeV electrons is approximately 2 mm in both $r-\phi$ and z. In addition, a set of proportional tubes (CPR) is located between the solenoid and the CEM. The CPR functions as a preradiator

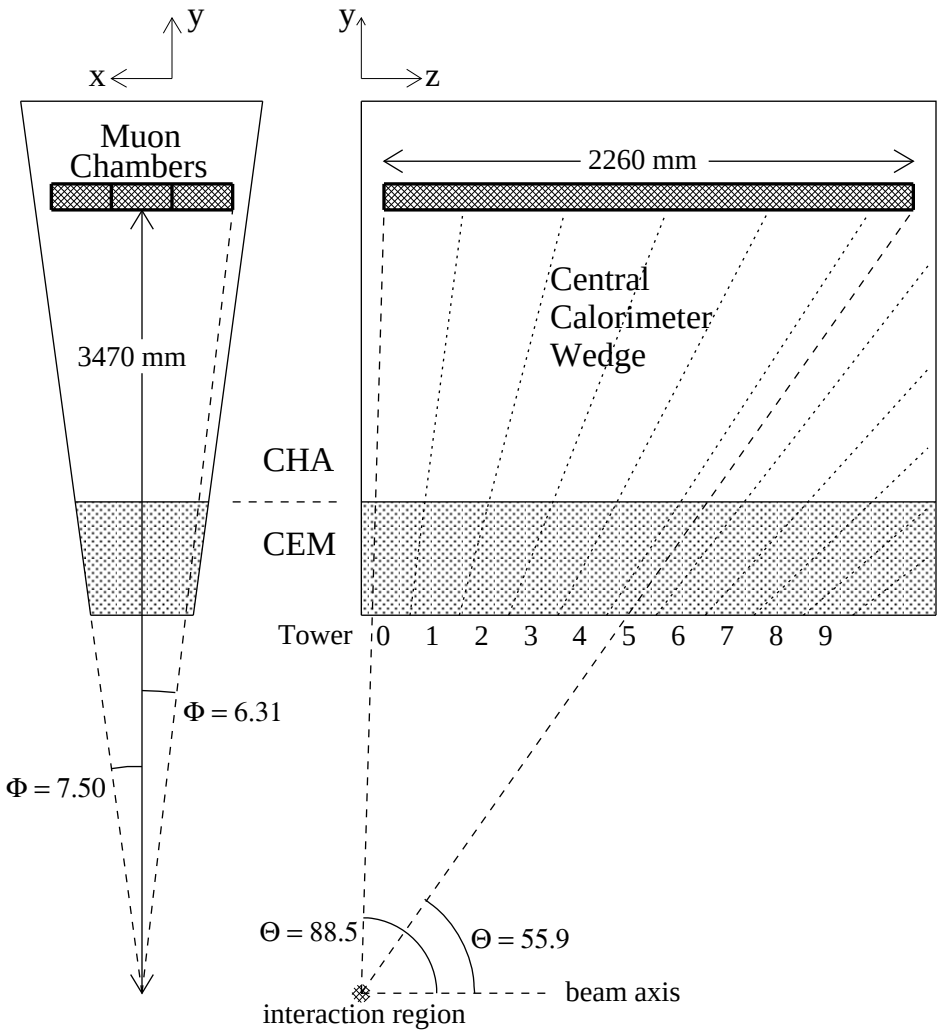

Figure 3.6: Geometry of the central calorimeter wedge and towers. The placement of the central muon chambers is also shown.

	Electromagnetic		Hadronic	
	PEM	FEM	PHA	FHA
Coverage (η)	$1.1 - 2.4$	$2.2 - 4.2$	$1.3 - 2.4$	$2.4 - 4.2$
Tower Size ($\delta\eta \times \delta\phi$)	$0.9 \times 5^\circ$	$0.1 \times 5^\circ$	$0.09 \times 5^\circ$	$0.1 \times 5^\circ$
Active Medium	Proportional tube chambers with cathode pad readout			
Absorber	Pb	94% Pb, 4% Sb	Fe	Fe
Interaction Length	18-21 X_0	25 X_0	5.7 λ_0	7.7 λ_0
Energy Resolution	$22\%/\sqrt{E} \oplus 2\%$	$26\%/\sqrt{E} \oplus 2\%$	$106\%/\sqrt{E} \oplus 6\%$	$137\%/\sqrt{E} \oplus 3\%$

Table 3.2: Characteristics of central and endwall calorimeters. Interaction lengths are given in radiation lengths (X_0) and absorption lengths (λ_0). The two components of the energy resolution are added in quadrature.

and helps distinguish electrons from hadrons. Electrons typically react in the solenoid coil and deposit several particles in the CPR, while hadrons should leave little or no energy.

3.4.2 Plug and Forward Calorimeters

The plug and forward calorimeters measure the energy and location of forward jets and help in determining the missing transverse energy in an event. As with the central, the plug and forward calorimeters have electromagnetic (PEM, FEM) and hadronic (PHA, FHA) components. Table 3.2 provides detailed information on the individual calorimeters.

These calorimeters use gas instead of scintillating material as their active medium. The PEM and FEM consist of alternating layers of lead absorber panels with conductive plastic proportional tube arrays. Each layer is read out by cathode pads arranged in towers, leading to a position resolution of approximately 2 mm in the plug and forward regions. Similarly, the PHA and FHA alternate steel absorber plates with conductive plastic proportional tubes which have cathode readout. The energy resolutions are determined from testbeam electrons and pions.

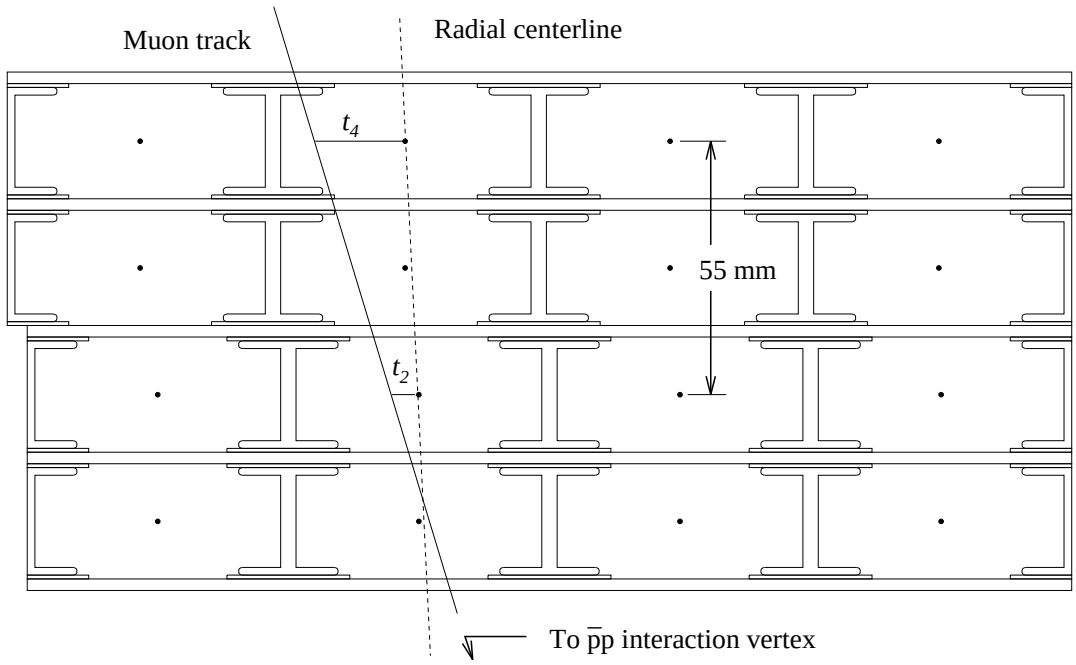

Figure 3.7: Transverse view of the central muon drift chambers.

3.5 Muon Detectors

The CDF muon detectors consist of arrays of drift tubes placed outside of the calorimeters. The lead and steel in the central calorimeters act as filters and prevent most non-muon particles from reaching the drift chambers. There are several subsystems which cover different ranges of η. The two sets of muon chambers in the central region are the Central Muon Chambers (CMU) and Central Muon Upgrade (CMP). Extending further out in η is the Central Muon Extension (CMX), and in the far forward region is the Forward Muon detector (FMU). Muons detected in the FMU are not used in this analysis.

The CMU is located just outside the central calorimeters and covers the pseudo-rapidity range $|\eta| < 0.6$. Like the calorimeter, it is divided into 24 wedges, each covering 15° in azimuth with each wedge subdivided into three 5° cells. Placement of the CMU

chambers is shown in Figure 3.6. Each wedge is also divided into east and west sections at $\eta = 0$. The wedges consist of four layers of drift chambers, giving measurements at four points along the trajectory of the particle. Figure 3.7 shows one section of a wedge through which a sketched track is drawn. The deviation from the radial direction (denoted by a dashed line) is a result of the particle deflecting in the magnetic field. The difference in drift times between projective wires allows a rough measurement of the particle P_T, which is used to select high momentum track candidates at the trigger level. The projective wire pairs, 1-3 and 2-4, are slightly offset. This provides the ability to uniquely select which side of the wire the track passed improving the resolution. The chambers also provide estimates of a tracks z position to about 5cm by measuring the relative charge collected at two ends of the sense wire. Due to gaps between the wedges, the CMU provides coverage for 85% of the $|\eta| < 0.6$ region.

Though the CHA acts as an absorber for the CMU, earlier data-taking showed that pion punch-through remained a significant background. A layer of steel 0.6 m thick was added behind the CMU for additional hadron absorption, and the CMP chambers were added behind this steel.

The CMP chambers are also made up of four layers of drift chambers and function similar to the CMU, though no z information is read out for the CMP. In contrast to the cylindrical shape of the CMU, the CMP chambers are mounted on four flat planes that surround the central detector. Because of its square shape, the wires in the CMP chambers are not projective. Due to gaps in the coverage of the CMP, it subtends only 63% of the solid angle for $|\eta| < 0.6$, and together the CMU and CMP cover only 53%.

Muon coverage is extended to in the $0.6 < |\eta| < 1.0$ region with the addition of the muon extension. The CMX is comprised of four free standing conical arches of drift tubes. The wires in the CMX chambers are projective and half cell staggered for ambiguity resolution and to reduce inefficiencies at the tube edges. The drift tubes are sandwiched between two layers of scintillators (CSX) which help identify particles originating from the

interaction vertex. These chambers cover 71% of the solid angle in the $0.6 < |\eta| < 1.0$ region.

3.6 The Trigger System

At CDF, the beams collide roughly every 3.5 μs with an average of one interaction per crossing in Run Ia and three interactions in Run Ib. This yields a 280 kHz event rate. It is impossible to record every interaction. CDF employs a three level trigger system to determine which events get recorded. The goal of the trigger system is to maximize the number of interesting events recorded while minimizing the amount of "dead-time", the time during which interactions are ignored while information in the detector is read out. Each level of the trigger is a logical OR of many separate triggers designed to identify electrons, muons, photons, and jets. Each successive level of the trigger processes fewer events than the previous level and employs more sophisticated analysis requiring more processing time. The Level 1 and Level 2 triggers are implemented in hardware with the level 2 decisions made by code running on custom processors, while the Level 3 trigger is performed by entirely by software.

The Level 1 trigger incurs no dead-time as it makes its decision in less than 3.5 μs. The trigger is based on identifying energy clusters in the calorimetry or tracks in the muon chambers. Electrons and jets are selected with a calorimetry trigger which requires a single tower to have an energy over a given threshold. The muon trigger requires that at least one pair of projective wires detect a track above threshold in transverse momentum. For regions covered by the CMP, confirmation from these chambers is also required. At Level 1, there is no tracking information available. Events passing the above criteria are passed along to Level 2. The Level 1 trigger reduces the event rate from 280 kHz down to 1 kHz.

The Level 2 trigger makes use of tracking information and more detailed calorimetry information. The central fast tracker (CFT) is a hardware processor which uses CTC hits to reconstruct high momentum tracks in $r - \phi$. The momentum resolution on the CFT is $\delta P_T/P_T^2 = 3.5\%$. At this stage, calorimeter clusters are formed by looking for a seed tower

above a certain threshold and adding in neighboring towers which pass a lower threshold. The transverse energy and position (η, ϕ) are calculated for each cluster. Tracks in the CFT are matched to CEM clusters to form electron candidates or to track segments from the CMU, CMP, and CMX to form muon candidates. The Level 2 trigger decision takes about 20 μs during which time the detector ignores subsequent crossings. This incurs a dead-time of a few percent. The event rate out of Level 2 is 20 to 35 Hz.

The Level 3 trigger is a software reconstruction algorithm which runs on a farm of Silicon Graphics processors. The level 3 software performs nearly complete event reconstruction. Besides selecting events, the Level 3 trigger also splits the data into several output streams for rapid access to specific physics channels and for later offline processing. All events passing the Level 3 trigger are written to 8 mm tape. The typical output rate for Level 3 is 5 to 10 Hz.

3.7 Offline Reconstruction

Events written to tape are processed offline with the full CDF reconstruction code. This code performs three-dimensional tracking and sophisticated identification of jets, electron, and muon candidates.

Jets are formed by finding clusters of energy in the calorimeter. The cluster starts with a seed tower which has transverse energy ($\mathrm{E_T}$) of at least 3 GeV. Neighboring towers which have $\mathrm{E_T} > 1$ GeV are added to the cluster. Adding of nearby towers continues until either there are no more towers with more than the minimum amount of energy, or a maximum cluster size is reached. An energy weighted centroid is calculated for the cluster. A jet's energy is defined to be the sum of energy within a cone of radius $\Delta R = 0.4$ about the centroid. This "raw" jet energy has not been corrected for various detector effects. Additional jet corrections are described in detail in Section 5.2.1.

Electron identification begins with a calorimeter based clustering algorithm similar to the one described for jets. An electron cluster also starts with a seed tower of at least 3 GeV of electromagnetic transverse energy ($\mathrm{E_T^{EM}}$). Adjacent towers with $\mathrm{E_T^{EM}} > 0.1$ GeV

are added until a maximum cluster size is reached. An electron candidate is required to have $E_T^{EM} > 5$ GeV and a ratio of hadronic to electromagnetic energy in the cluster less than 0.125.

A muon candidate consists of a CTC track which is matched to a track segment in a muon detector. Hits in the CMU, CMP and CMX are first fit to form track segments called stubs. Tracks from the CTC are then extrapolated out to the muon subsystems. The muon stubs are linked with the nearest CTC track in $r - \phi$ to form a muon candidate. The match is required to be consistent with multiple scattering of a muon traveling through the intervening material. The details of the matching requirements are presented in the next chapter.

Chapter 4

Event Samples

This analysis makes use of event samples from both Monte Carlo generators and data. The data samples were collected with the CDF detector described in the previous chapter. The Monte Carlo generators are computer programs which simulate data events generated by different physics processes. This chapter details the manner in which the final event samples are selected.

4.1 Data

The first step in measuring the mass of the top quark is to collect events expected to have originated from $t\bar{t}$ decays. As noted in Chapter 2, the top quark has several different final states each characterized by a particular decay mode for the two top quarks. For high mass top quarks, the Standard Model decay is expected to be nearly 100% to a b quark and a real W boson. This analysis focuses on the lepton plus jets decay channel. This channel is characterized by a high energy lepton and large missing energy from the leptonic decay of one W boson, and four jets from the hadronic decay of the other W, and the two b quarks from the initial $t\bar{t}$ decay.

Trigger	Prescaled			
	CMUP	CMU-only	CMP-only	CMX
1) $P_T > 12$ GeV/c track matched stub	NO	YES	-	YES
2) $P_T > 12$ GeV/c track matched stub and one jet with $E_T > 15$ GeV	NO	NO	-	YES
3) $\not\!\!E_T > 35$ GeV and two jets with $E_T > 3$ GeV	NO	NO	NO	NO

Table 4.1: Level 2 triggers used to select primary muon candidates in each muon system and whether it is prescaled. The CMP-only muons are accepted on the $\not\!\!E_T$ trigger.

4.1.1 Triggers

The events for this analysis are collected using a number of triggers which make use of tracking, calorimetry, and muon chamber information. The triggers are designed to select events with leptonic W decays. They specifically look for events with high energy leptons (electrons and muons) or those with large missing energy resulting from the undetected neutrino.

Electron candidates are identified at Level 1 by looking for a single CEM cluster with $E_T > 8$ GeV. The Level 2 trigger requires a CEM cluster with $E_T > 16$ GeV which matches to a CFT track with $P_T > 12$ GeV/c. This trigger is found to be about 90% efficient for electrons with $E_T > 20$ GeV. To increase the efficiency, a second trigger is also used which requires a CEM cluster with $E_T > 16$ GeV and $\not\!\!E_T > 20$ GeV.

Muon candidates are identified at Level 1 from hits in the CMU, CMP, and CMX chambers. Muon candidates in the various subsystems are referred to as stubs. The CMU and CMP have a large overlap but it is not complete. Muons passing through both systems are referred to as CMUP while those passing through only one are referred to as CMU-only and CMP-only respectively. The Level 2 trigger requires a CFT track with $P_T > 12$ GeV/c to be within 5° of the Level 1 muon stub. Because of high trigger rates (due largely to backgrounds), several of the muon triggers are prescaled. This means that only 1 out of n triggers are accepted. To avoid losing interesting events, two other triggers are also employed. One simply requires the addition of a calorimeter cluster (jet) with $E_T > 15$ GeV.

The other looks for events with very large missing energy, $\not{E}_T > 35$ GeV, along with two clusters with $E_T > 3$ GeV. A full list of the triggers and whether or not they are prescaled is shown in Table 4.1.

4.1.2 Electron Selection

A number of quality cuts are applied to the electron candidates. These selection requirements are listed in Table 4.2. The cuts are used to eliminate fake electrons, electrons in jets, and electrons resulting from photon conversions. The E_T of the CEM cluster is required to be above 20 GeV. Electrons are expected to deposit little energy in the hadronic calorimeter. To reflect this, a cut is imposed on the ratio of the hadronic energy of the cluster to the electromagnetic energy, HAD/EM. To ensure the track pointing to the cluster is the result of the same particle, a requirement is made on E/P, the ratio between the energy of the cluster and the momentum of the track. The shower profile as observed in the adjacent calorimeter towers is required to be similar to the profile measured for test beam electrons. The variable L_{shr} is used as an indicator. It is defined as:

$$L_{shr} = 0.14 \sum_i \frac{E_i^{observed} - E_i^{predicted}}{\sqrt{(0.14\sqrt{E})^2 + \sigma^2_{predicted}}} \tag{4.1}$$

where E_i is the energy in tower i either observed or predicted, $\sigma^2_{predicted}$ is the uncertainty on the predicted value, and $0.14\sqrt{E}$ is the uncertainty for the sum of the measured energy over all adjacent towers. To ensure good track matching, requirements are placed on how well the CTC track matches to hits in the CES chambers. The quantities $|\Delta x|$ and $|\Delta z|$ measure the distance in the $r - \phi$ and z directions, respectively, between the track and the shower position. A χ^2 test, χ^2_{strip}, is performed upon the electron shower profile in the CES relative to the shape measured from test beam electrons. A cut is placed on how well the the track matches to the primary vertex in the z direction. In addition the primary event vertex is required to be close to the center of the detector. The electron is also required to be isolated as defined by:

$$I^{electron} = \frac{|E_T^{cone} - E_T^{electron}|}{E_T^{electron}} \tag{4.2}$$

E_T	> 20 GeV
E_{had}/E_{em}	< 0.05
E/P	< 1.8
L_{shr}	< 0.2
$\|\Delta x\|$	< 1.5 cm
$\|\Delta z\|$	< 3.0 cm
χ^2_{strip}	< 10
$\|Z_{electron} - Z_{vertex}\|$	< 5 cm
$\|Z_{vertex}\|$	< 60 cm
$I_{electon}$	< 0.1
Fiducial Requirement	

Table 4.2: Summary of the electron selection criteria.

where E_T^{cone} is the transverse energy in a cone of $\Delta R = 0.4$ centered on the electron and $E_T^{electron}$ is the measured transverse energy of the electron. Finally, fiducial cuts are employed on the shower position to ensure the electron candidate is away from the calorimeter boundaries and its energy is well measured. The fiducial volume for electrons covers 84% of the solid angle in the region $|\eta| < 1.0$. The electron selection criteria are summarized in Table 4.2.

The above selection criteria are designed to enhance the signal for primary electrons. This analysis is specifically interested in electrons resulting from W boson decays. For this reason, it is desirable to remove electrons from the sample if they originate from photon conversions. Photons produced in a collision interact in the material of the detector, usually the VTX, and result in electron positron pairs. It is estimated that conversion electrons account for about 30% of the inclusive electron sample. As the photon is massless, tracks from conversion pairs can be identified by the presence of a second track which extrapolates back to a point where both tracks are tangent to a common line. The tracks are required to have have the same polar angle θ such that $|\Delta cot(\theta)| < 0.06$ and to pass within 0.3 cm of one another in the $r - \phi$ plane. If the second track has a low P_T, it may not be reconstructed. In order to remove electrons of this type, candidates with fewer than 20% of

$\lvert\Delta R\phi\rvert$	< 0.3 cm
$\lvert\Delta cot(\theta)\rvert$	< 0.06
OR	
$VTX_{occupancy}$	< 0.2

Table 4.3: Cuts used to select and remove photon conversion electrons.

the expected hits in the VTX are removed. Table 4.3 summarizes the cuts used to remove conversion electrons. The efficiency for conversion removal is $90 \pm 4\%$.

The efficiency of the above selection criteria for finding primary electrons is measured from Z boson decays. The spectrum of electrons from $Z \rightarrow e^+e^-$ decays is expected to be similar to that for electrons from W boson decays. In order to evaluate the efficiency of the selection cuts, very tight cuts are placed upon one electron and loose cuts are used to search for a second electron. Events for which there are two electrons with an invariant mass between 75 and 105 GeV are assumed to contain real electrons from Z boson decay. The secondary electrons are used to evaluate the efficiency of the selection criteria. The combined efficiency for all cuts including photon removal is $80 \pm 2\%$.

4.1.3 Muon Selection

Muon candidates are selected using the following criteria which are detailed in Table 4.4. The P_T of the reconstructed track is required to exceed 20 GeV/c. Tighter track to muon stub matching is imposed. This cut is looser for the CMP and CMX stubs than for the CMU. This is a consequence of more multiple scattering experienced by particles traversing additional material in reaching these systems. Muons are unlikely to interact in the calorimetry and should deposit little energy there. Limits are imposed upon the amount of electromagnetic and hadronic energy deposited in the direction of the muon to reflect this. As with the electrons, the z position of the muon and the event vertex are required to be within 5 cm, and the event vertex is required to lie near the center of the detector. In addition, the measured impact parameter of the muon track must be less than 3 cm. The

P_T	> 20 GeV/c
$\|\Delta X\|_{CMU}$	< 2.0 cm
$\|\Delta X\|_{CMP}$	< 5.0 cm
$\|\Delta X\|_{CMX}$	< 5.0 cm
E_{em}	< 2.0 GeV
E_{had}	< 6.0 GeV
$\|Z_{muon} - Z_{vertex}\|$	< 5 cm
$\|Z_{vertex}\|$	< 60 cm

Table 4.4: The selection criteria for muon candidates.

isolation requirement for muons is given by:

$$I^{muon} = \frac{\mathrm{P_T^{cone}} - \mathrm{P_T^{tower}}}{\mathrm{P_T^{muon}}} \tag{4.3}$$

where $\mathrm{E_T^{cone}}$ is the transverse energy in a cone of $\Delta R = 0.4$ centered on the muon, $\mathrm{E_T^{tower}}$ is the transverse energy in the tower to which the muon track points, and $\mathrm{P_T^{muon}}$ is the momentum of the reconstructed muon track. As with electrons, the muons are required to have an isolation of less than 0.1.

The efficiency for identifying primary muons with the above cuts is evaluated with $Z \rightarrow \mu^+\mu^-$ decays. The method is identical to that used to determine the electron efficiency. The efficiency differs for the individual muon subsystems. It is found to be $94 \pm 1\%$ for CMUP muons, $90 \pm 2\%$ for CMU-only muons, $88 \pm 2\%$ for CMP-only muons, and $91 \pm 1\%$ for CMX muons.

4.1.4 W Selection

The neutrino which results from a leptonic W boson decay does not interact in the detector so it cannot be detected directly. The presence of neutrinoes is inferred from the missing transverse energy, or $\not\!\!E_T$. The raw $\not\!\!E_T$ is simply calculated by taking the negative vector sum of transverse energy deposited in each of the calorimeter towers. For events with a primary muon, the $\mathrm{P_T}$ of the muon vectorally subtracted from the $\not\!\!E_T$ while the energy of the calorimeter tower associated with the muon is added back in. To avoid mistaken $\not\!\!E_T$

Electrons:	
E_T	> 10 GeV
E_{had}/E_{em}	< 0.12
$I^{electron}$	< 0.2
E/P	< 2.0
Muons (with stub):	
P_T	> 10 GeV/c
E_{em}	< 5.0 GeV
E_{had}	< 10.0 GeV
$\|\Delta X\|_{CMU,CMP,CMX}$	< 5.0 cm
I^{muon}	< 0.1
Muons (without stub):	
P_T	> 10 GeV/c
E_{em}	< 2.0 GeV
E_{had}	< 6.0 GeV
$\|\eta\|$	< 1.1
I^{muon}	< 0.2

Table 4.5: The selection criteria used to identify secondary lepton candidates from Z boson decays.

from undetected particles, similar corrections are performed for minimum ionizing tracks with $\mathrm{P_T} > 10$ GeV/c which pass loose matching requirements with a muon stub or tracks which extrapolate to regions not covered by the muon detectors. The W sample is made up of events with $\not{E}_{\mathrm{T}} > 20$ GeV.

At this stage cuts are imposed on the W sample to remove events resulting from Z boson decays or events collected during known detector problems, referred to as "bad runs". As mentioned previously, Z boson events are identified by searching for a second oppositely charged lepton which yields an invariant mass near the Z mass. The selection criteria for the secondary leptons are listed in Table 4.5. During data taking, runs are flagged as a bad run if there is a problem with any of the detector subsystems. The most common examples are high voltage trips in detector components or noise oscillations in the muon chambers. After all the cuts, there are nearly 100,000 W candidates. There are roughly 38,000 from muons and 57,000 from electrons.

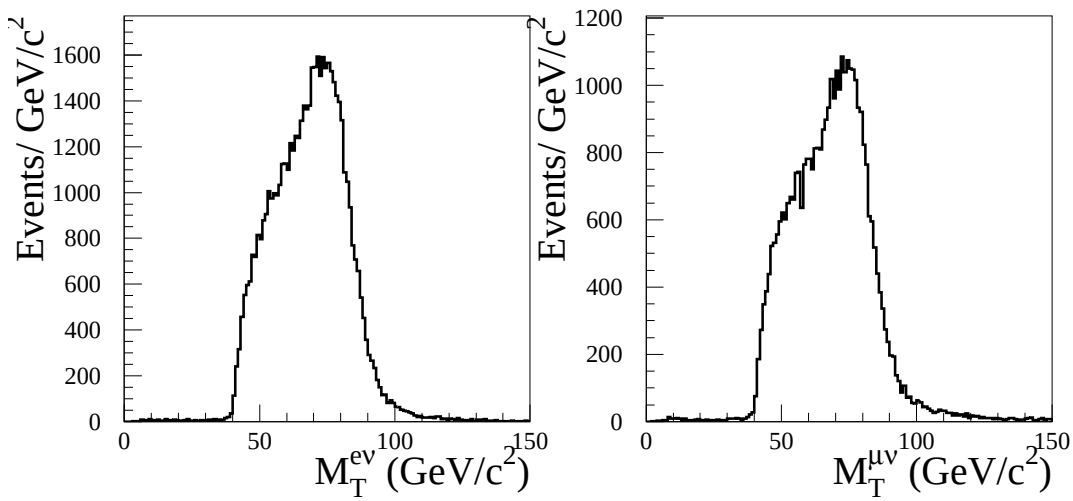

Figure 4.1: The transverse mass of the lepton and missing energy for electron and muon events in the W candidate sample.

To verify whether the above selection criteria are actually identifying real W bosons, the transverse mass of the candidate W's is examined. It is not possible to fully reconstruct the mass of the W's as the longitudinal momentum of the neutrino is unknown. The transverse mass can be calculated using:

$$\mathrm{M_T} = \sqrt{(|\mathrm{P_T^{lep}}| + \not{E}_\mathrm{T})^2 - (\vec{\mathrm{P_T^{lep}}} + \vec{\not{E}}_\mathrm{T})^2} \tag{4.4}$$

where $\mathrm{P_T^{lep}}$ is either the transverse energy of the electron or the reconstructed transverse momentum of the muon. Figure 4.1 shows the transverse mass plots for both electron and muon events in the W sample. Both plots show the expected Jacobian peak at the W mass, approximately 80 GeV.

4.1.5 Top Mass Sample

Besides the W boson leptonic decay products, events must contain at least four jets for the $t\bar{t}$ decay to be fully reconstructed. The standard jet selection criteria used by CDF demands that a cluster be located within $|\eta| < 2.0$ and have $\mathrm{E_T} > 15$ GeV to be accepted. This specification is dictated by the requirement that the jet be taggable by the displaced

vertex b-tagging algorithm employed by CDF. The tagging algorithms will be discussed further in the following section. The event selection used in this analysis requires three jets to pass the above cuts. For the fourth jet, the cuts are relaxed to $|\eta| < 2.4$ and $E_T > 8$ GeV to increase the acceptance. This increases the expected acceptance of top events by 22%. There are 163 events in the W candidate sample which pass these requirements. Estimates based upon Standard Model cross sections for expected backgrounds predict less than half of the events in this sample will originate from $t\bar{t}$ decays.

As discussed in Section 2.3, the dominant source of background is expected to come from QCD $W+$ multijet production. The signature of such events is nearly identical to that of the $t\bar{t}$ signal under study. There is one major difference. Events resulting from the decay of $t\bar{t}$ pairs should contain two jets originating from b quarks (b-jets), while the jets in $W+$multijet events are predominantly from light quarks and gluons. Thus, if events containing b-jets can be identified, the top signal can be enhanced relative to the background.

4.1.6 b-Tagging

Two methods are employed to search for b-jets. The first method utilizes the precise tracking capabilities of the silicon vertex detector (SVX), to identify decay vertices from B hadrons by their displacement from the primary event vertex. The second technique looks for additional leptons (e or μ) inside a jet which result from the semileptonic decay of B hadrons. Jets identified as coming from b decays are termed b-tagged, and the algorithms used to tag the jets are called b-taggers.

4.1.6.1 Silicon Vertex Detector Tags (SVX)

There are two key elements which make displaced vertex tags possible. The fact that B hadrons are long-lived with a lifetime of about 1.5 picoseconds, and they are expected to be very energetic in top decays. The average b quark is expected to travel 3.5 mm in the radial direction before it decays. The SVX detector provides precise tracking in the interaction region which makes it possible to reconstruct disjoint locations of the primary

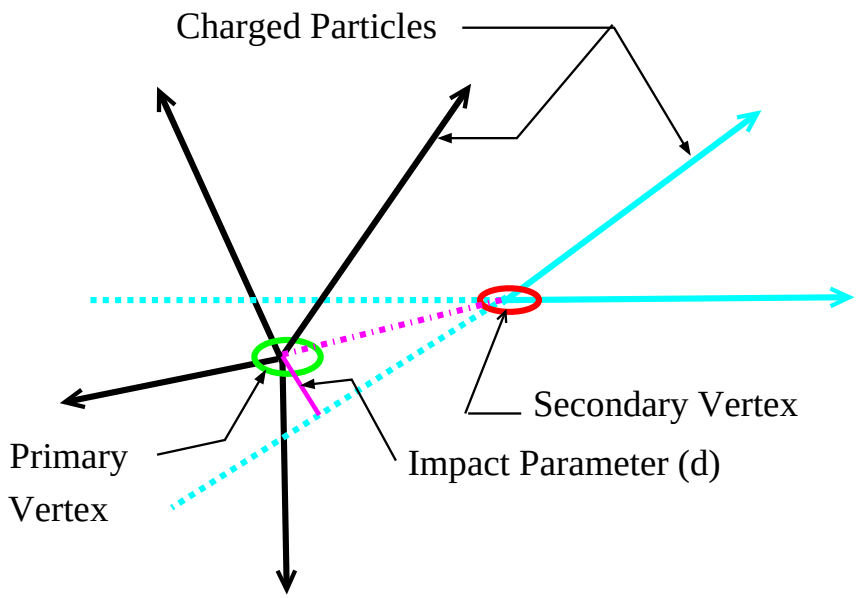

Figure 4.2: Schematic of a displaced vertex as reconstructed by the silicon vertex detector.

and secondary vertices in the $r - \phi$ plane. Figure 4.2 illustrates this. The resolution of this method depends upon how well the primary vertex is reconstructed and upon the uncertainty of tracks associated with the secondary vertex.

To determine the primary vertex, a weighted fit is performed using SVX tracks and VTX z position information. The process entails an iterative approach which removes tracks with large impact parameters. The impact parameter is the distance of closest approach to the primary vertex in the $r - \phi$ plane, see Figure 4.2. The uncertainty on the position of the primary vertex ranges from 6 to 26 μm and is dependent mainly upon the number and quality of the tracks associated to the primary vertex. In the event there are multiple candidates for the primary vertex, as was often the case with high luminosity runs, the P_T for each track associated to a vertex is summed, and the vertex with the largest total transverse momentum is taken as the primary vertex. All subsequent tracks used in the analysis are required to pass within 5 cm in z of the chosen primary vertex. The expected z resolution for CTC tracks with $P_T > 2$ GeV/c is about 6 mm.

In order to be considered for tagging, SVX tracks must be associated with jets that

have calorimeter $E_T > 15$ GeV and $|\eta| < 2.0$. An SVX track is associated with a jet if it lies within 35° of the jet direction determined from the calorimeter. Photon conversions and K_s or Λ decays can also produce displaced tracks. To remove these backgrounds, an impact parameter cut ($|d| < 0.15$ cm) is imposed on the tracks. This cut is expected to be 99% efficient for tracks from b decay. In addition track pairs which reconstruct to a K_s or Λ mass are removed.

The algorithm used to search for SVX tags, employs a two step process. Initially it attempts to reconstruct a displaced vertices using three or more tracks selected with loose track requirements. If this fails, it searches for a displaced vertex using only two tracks with tighter quality cuts. Displaced vertices are reconstructed from displaced tracks identified within a jet. Displaced tracks are those for which the impact parameter, d, is large compared to its uncertainty. The distance in the transverse plane from the primary vertex to the secondary vertex is called L_{xy}. The quantity L_{xy} is positive if the secondary vertex and the corresponding jet are on the same side of the primary vertex. It is negative if they are on opposite sides. Only jets which have a significantly displaced vertex ($|L_{xy}|/\sigma_{L_{xy}} \geq 3.0$) and a positive L_{xy} are tagged. The resolution for displaced vertices is approximately 130 μm. For a detailed description of the SVX tagger see [8] [16].

The efficiency for tagging a b-jet is measured from the data in the inclusive electron and muon samples which are enriched in $b\bar{b}$ decays. This efficiency is compared to the efficiency determined from tagging generic b's in a Monte Carlo simulation. The ratio of the measured efficiency between the data and the Monte Carlo is 0.83 ± 0.03 [18]. This differs from 1.0 as a result of higher track reconstruction efficiency in the simulated events relative to measured data. This ratio is used to correct the estimated efficiency for tagging b-jets from $t\bar{t}$ Monte Carlo events for comparisons to real data. For a top mass of 175 GeV/c^2, 67% of the events are expected to have at least one taggable b jet. The overall efficiency for at least one SVX tag in a $t\bar{t}$ event is about 40% which includes the 0.8 scale factor.

4.1.6.2 Soft Lepton Tags (SLT)

An alternate method for tagging b quarks identifies leptons resulting from semileptonic b decays. These occur via $b \rightarrow l\nu_l X (l = e \text{ or } \mu)$, or $b \rightarrow c \rightarrow l\nu_l X$. The latter being referred to as a cascade decay. Because these leptons are expected to have much less P_T than those resulting from W decays, jets tagged by this method are referred to as soft lepton tags, or SLT.

As described earlier, electrons and muons are identified by extrapolating CTC tracks to electromagnetic clusters or muon chamber hits. To maintain a high selection efficiency for leptons from direct b decay and cascade decays from daughter c quarks, the P_T threshold for considered tracks is set at 2.0 GeV/c. To be considered for this analysis, a track must also lie within a cone $\Delta R = 0.4$ of a jet. To search for electrons, each track is extrapolated to the calorimeter and checked for a matching CES cluster. A matched cluster is required to have a shower profile consistent with expectations for electrons. To identify muons, tracks are checked for a matching stub in the muon chambers. To maintain good efficiency on non-isolated muons, the minimum ionizing requirements (described in Section 4.1.3) used to identify muons from W decays are not imposed. The details of the SLT algorithm can be found in [8] [17].

The lepton finding efficiency, as a function of lepton P_T, for the SLT algorithm is determined from photon conversions and $J/\psi \rightarrow \mu\mu$ data samples. This efficiency is then applied to Monte Carlo $t\bar{t}$ events to determine the efficiency for tagging b-jets. The probability for finding an additional e or μ from a b quark decay in a $t\bar{t}$ event is $18 \pm 2\%$.

4.1.7 Tagged Sample

Events in the mass sample which have at least one of the four highest E_T jets tagged by either the SVX or the SLT tagging algorithms are included in the tagged sample. There are a total of 36 events in the tagged sample. 20 events with at least one SVX tag, and 22 events with at least one SLT tag. There are 7 events with a jet tagged by both algorithms

Tag Type	# of Events
SVX	20
2 SVX	5
SLT	22
SLT-e	6
SLT-μ	17
Total	36

Table 4.6: The number of events with at least one jet tagged by either the SVX or SLT algorithms.

and 6 events with two jets tagged. Table 4.6 gives the complete tagging breakdown for the events. The tagged sample will be used to determine the top quark mass in this analysis.

4.1.8 Backgrounds

The sources of backgrounds expected in the tagged sample come from W+multijet events with heavy flavor, mistags, non-W ($b\bar{b}$) events, single top events, diboson (WW, ZZ) events, $Z \rightarrow \tau^+\tau^-$, and Drell-Yan. The following is a brief description of the main sources of background expected for both the SVX and SLT tagging algorithms. The backgrounds are examined in detail in [8].

The largest source of background in the SVX tags is expected from QCD W plus heavy flavor, for example $p\bar{p} \rightarrow Wg(g \rightarrow b\bar{b}$ or $c\bar{c})$. Monte Carlo samples are used to determine the efficiency for tagging each source of background as a function of the number of jets in the event. This is compared to the number of W+jet events present in the data to estimate the background contribution from each source. The second largest source comes from mistags. Mistags are jets which are tagged but do not contain a true displaced vertex. It is assumed mistagged jets have an L_{xy} distribution which is symmetric about zero. Jets with a negative L_{xy} are parametrized as a function of $\mathrm{E_T}$, η, and the number of SVX tracks. This parametrization is applied to the W+jet data to determine the expected number of mistags.

The dominant source of background in the SLT tags comes from "fake" soft leptons. Fake tags are defined as tags due to particles which did not originate from a heavy flavor decay. This includes non-leptons which pass the lepton identification cuts such as pions faking an electron or muon as well as real leptons which result from other processes such as photon conversions or pions decaying in flight. The fake background is evaluated by determining the fraction of tags per track in a generic jet sample as a function of track P_T. This probability is applied to tracks in the W+jet events to estimate the background present.

The remaining sources of background are evaluated similarly for each tagging algorithm. The non-W, expected to be mostly $b\bar{b}$ events, is estimated by looking at the number of tags in the data as a function of lepton isolation and $\not\!\!E_T$. The number of tags with low $\not\!\!E_T$ and low isolation (expected to contain no real W events) is used to predict the background in the W signal region. The remaining sources of background including single top, diboson, Drell-Yan, Wc, and $Z \rightarrow \tau^+\tau^-$ are evaluated from Monte Carlo predictions. They are all estimated to be small compared to the other sources.

4.2 Monte Carlo

Monte Carlo event generators are used to simulate the physics of $p\bar{p}$ collisions. The measurement of the top mass presented in this analysis relies upon Monte Carlo simulations of $t\bar{t}$ events and of background events. The simulated events are used to determine the acceptances of several classes of events that may be present in the data. These acceptances, together with other information, are used to estimate the relative top and background fractions in different event samples. Monte Carlo simulations were used in the same way in establishing that a top signal was present and in estimating the cross section [8]. Simulated $t\bar{t}$ events are also used to estimate the relation between a measured jet energy and the parent parton energy. Here, the measured energy includes the standard jet energy corrections. This relation is specific to the initial parton source, whether from a W boson hadronic decay, or from a b quark. In the latter case semileptonic decays (with their unobserved neutrinos)

are taken into account. Most importantly, the simulated events are used to model the kinematics of both background and $t\bar{t}$ events with varying top masses.

For all Monte Carlo samples, the response of the CDF detector to the resulting final state particles is simulated [19], and jets and leptons are reconstructed using the same CDF reconstruction algorithms that are applied to the data. The simulation includes the silicon vertex detector. This allows the same selection requirements to be applied to the Monte Carlo samples as are applied to the data.

4.2.1 Top Samples

For $t\bar{t}$ events, the primary Monte Carlo program used is HERWIG [20], version 5.6. The HERWIG program was selected because it best models the observed properties of multijet events in the CDF data [21]. In addition, the programs PYTHIA [22] and ISAJET [23] version 6.36 are used for cross checks and for estimating some systematic uncertainties. Both the HERWIG and PYTHIA programs are based upon leading order QCD matrix elements for the hard-scattering processes. HERWIG uses a multi-process coherent, parton shower model with cluster hadronization and an underlying event model based upon data. PYTHIA uses a multi-process model with coherent final state showers, string hadronization and decay, and an underlying event model based upon parton scattering. Both HERWIG and PYTHIA include color correlations between initial and final state partons. ISAJET uses a parton shower program based upon leading order QCD matrix elements for hard-scattering sub-process, incoherent gluon emission, and independent fragmentation of the outgoing partons.

4.2.2 Background Samples

To study kinematic fitting of background events, simulated QCD W boson plus jets events are used. These events are produced by the program VECBOS [24]. VECBOS is a parton-level program, based on tree-level matrix element calculations. The partons produced by VECBOS are input into the same coherent parton shower evolution and cluster

hadronization as is used in HERWIG. The same underlying event model is also used. For the factorization and renormalization scales in VECBOS, $Q^2 =< P_T >^2$ is used, that is, with Q^2 set to the square of the average P_T of the outgoing partons. The sensitivity to these scales is tested using $Q^2 = M_W^2$.

Chapter 5

$t\bar{t}$ Reconstruction Algorithm

As previously noted, the kinematics of Standard Model $t\bar{t}$ decays through the $t\bar{t} \rightarrow l\nu q\bar{q}b\bar{b}$ channel allow for complete reconstruction of the four momenta of the original t and $\bar{t}$ quarks. The fitting algorithm calculates the four momenta of the t and $\bar{t}$ for a given event by reconstructing them from the four momenta of the six particles in the decay: $l, \nu, b, \bar{b}, q$, and $\bar{q}$. The lepton and the quarks are directly observable by the CDF detector while the neutrino momentum must be inferred. The quarks are observed as jets. In events with more than four jets, only the leading four jets are assigned to $t\bar{t}$ decay quantities. Using the observed quantities and their uncertainties along with kinematic constraints imposed by $t\bar{t}$ decay hypothesis, the algorithm leads to the construction of a χ^2 which can be minimized to yield the best estimates for the momenta of all particles in the decay chain. This chapter describes the constraints used to reconstruct $t\bar{t}$ decays and the corrections applied to the observed quantities input to the fit. The performance of the algorithm is evaluated using samples of Monte Carlo events for both signal and background.

5.1 Constraints

Understanding the reconstruction algorithm requires careful definition of the constraints involved in mass reconstruction. An illustration of the problem is shown in Figure 5.1. The hypothesized production and decay of a $t\bar{t}$ pair is shown on the left side. The

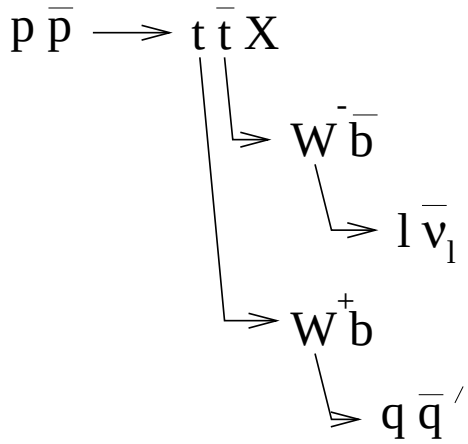

	known	unknown
p's	8	0
t's	1	7
X	2	2
W's	2	6
b's	8	0
q's	8	0
l	4	0
ν	1	3
	34	18

5 vertices → 20 equations
13 4-vectors → 52 variables

18 unknowns → "2C"

Figure 5.1: Counting constraints in the hypothesized $t\bar{t}$ decay system.

unspecified debris resulting from the remains of the proton and anti-proton are denoted as a single four vector, X. The 13 four vectors in the problem yield 52 variables, some of which are measured or have assumed values. Each arrow in the diagram represents a vertex where energy and momentum are conserved. Thus five arrows imply 20 equations of constraint. The right hand side of Figure 5.1 illustrates the number of variables considered known or unknown for each four vector.

It is assumed that the four vectors for the proton and anti-proton are known. The mass of the t and $\bar{t}$ are assumed equal with a width ($\sigma_{M_{top}}$) of 2.5 GeV/c^2 [26], leaving seven unmeasured quantities for their respective four vectors. The transverse momentum of X is measured from the total energy deposited in the calorimeter. The mass and p_z of X are unknown. The W bosons in the decay are assigned $M_W = 80.4$ GeV/c^2 with a width (σ_{M_W}) of 2.12 GeV/c^2 [27]. The momenta of the W bosons is unknown. The momenta of the b quarks and light quarks are measured from the jets and their masses are set at 5.0 GeV/c^2 and 0.5 GeV/c^2 respectively. The lepton is the best measured quantity in the

system. The neutrino is inferred from the missing energy. In this repect, its momenta are treated as complete unknowns and solved for by conservation of momentum in the fit. The neutrino mass is set to zero. This formulation yields 18 unknowns and 20 equations of constraint, resulting in a twice over-constrained or "2C" fit. It is possible to formulate a χ^2 and minimize it to solve for the unknown quantities.

In formulating the χ^2, it is convenient to separate it into two parts, $\chi^2_{measurement}$ and $\chi^2_{constraint}$. The $\chi^2_{measurement}$ term contains all the uncertainties on relevant quantities measured by the detector. The $\chi^2_{constraint}$ term contains the kinematic constraints imposed by the $t\bar{t}$ decay hypothesis. Each term in the χ^2 allows deviations corresponding to the uncertainty for the respective measurement or constraint. The measurement terms include the lepton, jets, and unclustered energy, while the constraint terms include the mass of the top quarks being equal and the mass of the W bosons.

The measurement portion of the χ^2 is written as:

$$\chi^2_{measurement} = \sum_{lep,JETS} \frac{\left(\hat{E}_t - E_t\right)^2}{\sigma^2_{E_t}} + \sum_{i=x,y} \frac{\left(\hat{E}^U_i - E^U_i\right)^2}{\sigma^2_{E^U_i}} \tag{5.1}$$

where the first sum is over the primary lepton and all jets with $\mathrm{E_T} > 8$ GeV and $|\eta| < 2.4$ and the second sum is over the transverse components of the unclustered energy, U. The hatted variables, $\hat{E}_t$ and $\hat{E}^U_i$, represent the fitted outputs, and E_t and E^U_i represent the fully corrected quantities input to the fit. Note that the transverse quantities are used rather than the full energies. This reflects the fact that the transverse energy is the best understood quantity in $p\bar{p}$ collisions. There is an inherent uncertainty upon the longitudinal momentum due to the fact that longitudinal momentum in the initial collision is unknown. Due to this fact, all resolutions are expressed in terms of σ_{E_t}. The constraint term is expressed as:

$$\chi^2_{constraint} = \frac{(M_{l\nu} - M_W)^2}{\sigma^2_{M_W}} + \frac{(M_{jj} - M_W)^2}{\sigma^2_{M_W}} + \frac{(M_{l\nu j} - M_{top})^2}{\sigma^2_{M_{top}}} + \frac{(M_{jjj} - M_{top})^2}{\sigma^2_{M_{top}}} \tag{5.2}$$

where the invariant masses are calculated from the fitted four vectors of the relevant quantities. Conservation of energy and momentum is not explicitly expressed in the χ^2 but is used to compute the invariant masses in the constraint term. In this formulation, the fit parameters are the transverse energies for the lepton and each of the jets, the two components

of the unclustered energy, the reconstructed top mass, M_{top}, and the P_z of the neutrino (the z component of X would be an equivalent choice to use, but P_z of the neutrino simplifies the calculations). This formulation yields $N_{JETS} + 5$ fit parameters with N_{JETS} being the number of jets in the event. There are $N_{JETS} + 3$ terms in $\chi^2_{measurement}$ and four terms in $\chi^2_{constraint}$. Hence, there are two more terms in the χ^2 than there are fit parameters which is equivalent to the tabulation in Figure 5.1.

There are twelve unique ways to assign the four leading jets to the partons in the fit. The P_z of the neutrino is determined from the W mass constraint. This results in two possible solutions, giving a total of 24 possible configurations for a given event. In this analysis, all events contain at least one jet identified as a b hadronized quark. Jets which have been b-tagged are assigned to be from b quarks in the fit. Thus, for events with one jet tagged, there only six possible jet assignments and twelve configurations. For events with two jets tagged, there are only two jet assignments (the two b's can be interchanged) and four total combinations. When fitting an event, all allowed combinations are tried and the configuration with the lowest minimized χ^2 is chosen. At this point, a goodness of fit cut is imposed and events with $\chi^2 > 10.0$ are rejected. Figure 5.2 shows the distribution for the minimum χ^2 in a sample of HERWIG Monte Carlo with $M_{top} = 175$ GeV/c^2. This cut is expected to be 95% efficient for $t\bar{t}$ events and 83% efficient for QCD $W+$ jet events.

5.2 Corrections

The corrections are used to provide an estimate of the parton kinematics under the assumption that the event resulted from a $t\bar{t}$ lepton plus jets decay. This predominantly involves estimating the original quark momenta from the observed jet energies for the leading four jets in the event. Additional jets in the event are also corrected along with the unclustered energy to obtain the best estimate of X, the quantity the $t\bar{t}$ system recoils against, and hence the missing energy. Corrections to the primary lepton in the event are also applied, but they are small as these quantities are considered well measured. These corrections do not depend upon the $t\bar{t}$ decay hypothesis and are detailed elsewhere [25].

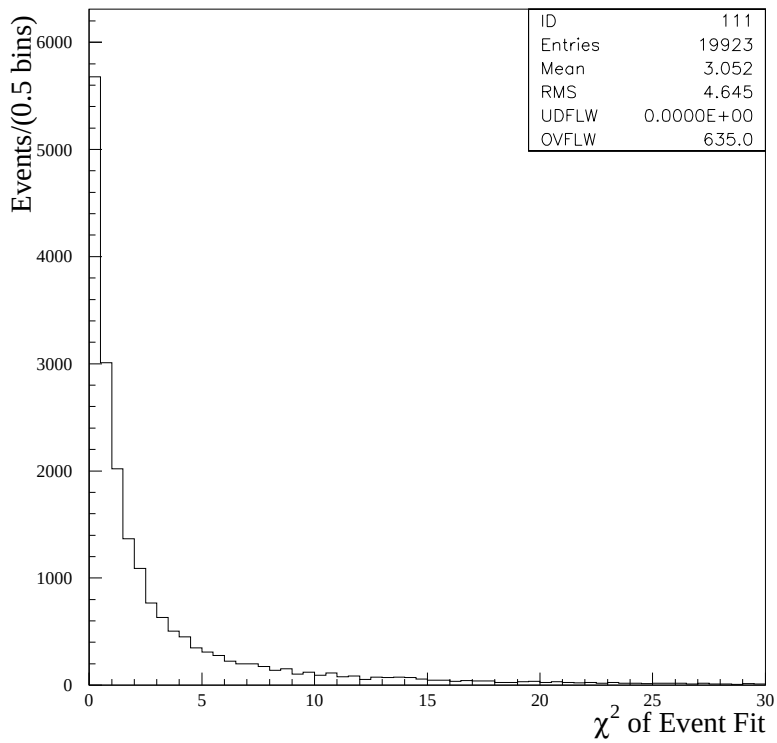

Figure 5.2: Distribution of fitted χ^2 for HERWIG Monte Carlo with M_{top} = 175 GeV/c^2. Events with $\chi^2 > 10.0$ are rejected.

5.2.1 Jet Energy

The corrections applied to jets are done in two steps. In the first step, a set of standard adjustments are applied to provide an estimate of the true jet energy from the observed jet energy. These corrections have been derived by the members of the QCD group and are applied to all jets in the event. The second step involves estimating the actual parton energy from the "corrected" jet energy. This is dependent upon how the jet is assigned during the fitting procedure discussed in the previous section. The standard corrections applied to all jets are referred to as generic jet corrections to distinguish them from the flavor dependent jet corrections.

The generic jet corrections are designed to account for a number of known sources of jet mismeasurement. These include detector effects, energy falling outside the clustering

cone, and contributions from underlying event and multiple interactions. These corrections are applied to all jets in the event with $E_T > 8$ GeV and $|\eta| < 2.4$ using a clustering cone of $\Delta R = 0.4$. For a given jet, its corrected energy, E^{cor}, can be expressed as:

$$E^{cor} = (E^{raw} \times f_{rel} - UEM) \times f_{abs} - UE + OC \tag{5.3}$$

where:

- E^{raw} is the raw measured jet energy
- f_{rel} is the relative jet energy correction
- UEM is the underlying event correction for multiple vertices
- f_{abs} is the absolute energy scale correction
- UE is the underyling event correction for the primary vertex
- OC is the energy estimated outside the clustering cone

The corrections are applied in the order shown in equation 5.3. Each of the corrections is described in more detail below.

The relative jet energy corrections are used to scale the jet response everywhere in the detector to that of jets in the central calorimeter, $0.2 < |\eta| < 0.7$. It is derived by looking at the average P_T balance in large data samples of dijet events where one jet is required to lie in the central calorimeter. The correction is derived as a function of η and P_T and accounts for cracks between calorimeter components and energy scale differences between the different components. A complete account of the relative corrections can be found in Appendix B.

The absolute jet energy scale is based upon measured detector response and fragmentation effects. The CDF detector simulation has been tuned to reproduce the response observed for test beam electrons and pions. The test beam data along with minimum-bias events were used to determine the detector response. This provides accurate measurements

for individual particles but not necessarily jets. Fragmentation is the term applied to the evolution of the primary parton (or gluon) into a jet of particles. Each of the subsequent particles deposits energy in the calorimeter, often showering into additional particles through secondary interactions. The energy sampled in this spray of particles provides the raw jet energy measurement. The mapping of raw jet energy to absolute jet energy is determined by looking at jets generated with the ISAJET fragmentation model which had been tuned to reproduce a number of experimental distributions. The correction factor is determined by comparing the $\sum P_T$ of all particles produced in the Monte Carlo which lie within the clustering cone of the jet to the raw jet energy observed in the calorimeter. The absolute correction is derived as a function of jet P_T.

The underyling event correction has been separated into two pieces. It was originally implemented to account for energy added to a jet from spectator quarks in the primary collision, the UE correction. There is now a separate correction, UEM, to account for extra energy added by other soft collisions, identified by more than one vertex, in the event. Since the absolute correction was derived assuming only one interaction, it is necessary to apply these corrections separately with the UEM correction applied before the absolute correction and the UE correction applied after. UE is fixed at 0.65 GeV for a cone size of 0.4, while UEM is 0.3 GeV per vertex for each additional vertex present in the event.

The out of cone correction is also made up of two components. One accounts for the difference in the average E_T observed when using a clustering cone of 0.4 and 1.0 in both Monte Carlo and Data. This is termed the soft gluon correction since the fraction of energy outside the clustering cone is expected to depend on the jet shape. It is derived as a function of jet P_T. The second component accounts for energy which lies outside a cone of 1.0. This is expected to be about 1 GeV on average and is fixed for all jets.

The size of the correction factor for the above effects is shown in Figure 5.3. The corrections are shown as a function of E_T for a jet in the central with $\eta = 0.7$. Jets from $t\bar{t}$ decays are typically about 50 GeV and receive an average correction factor of about 1.2.

The four highest E_T jets in the event are assigned to the quarks expected in the

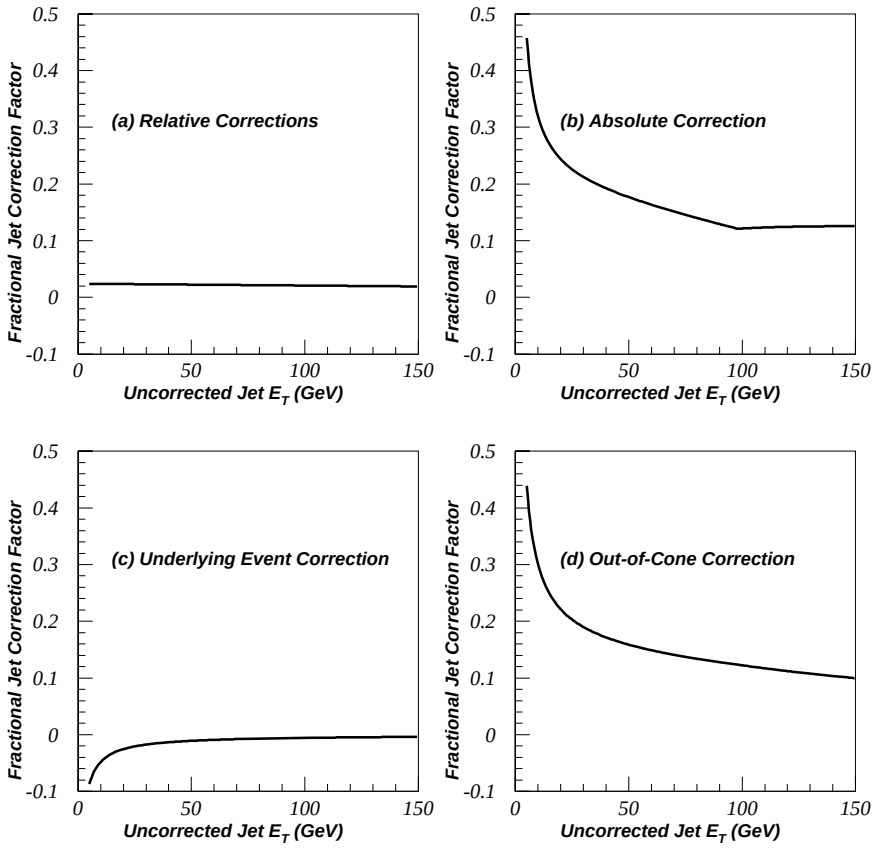

Figure 5.3: The size of the standard corrections as a function of E_T for (a) the relative correction, (b) the absolute correction, (c) the underlying event correction, and (d) the out of cone correction. The corrections are derived for a jet with a cone size of 0.4 and $\eta = 0.7$.

$t\bar{t}$ decay. These jets receive an additional parton specific correction dependent upon the type of parton they are assigned to in the fit and whether a jet was tagged by SLT. There is a specific correction for jets from light quarks, generic b quarks, b quarks that decayed semileptonically into the electron channel, and b quarks that decayed semileptonically into the muon channel. These corrections are derived by comparing the parton momenta in HERWIG generated $t\bar{t}$ events to the fully corrected jet momenta as a function of jet P_T. Figure 5.4 illustrates the fractional change in jet E_T, after all generic corrections are applied,

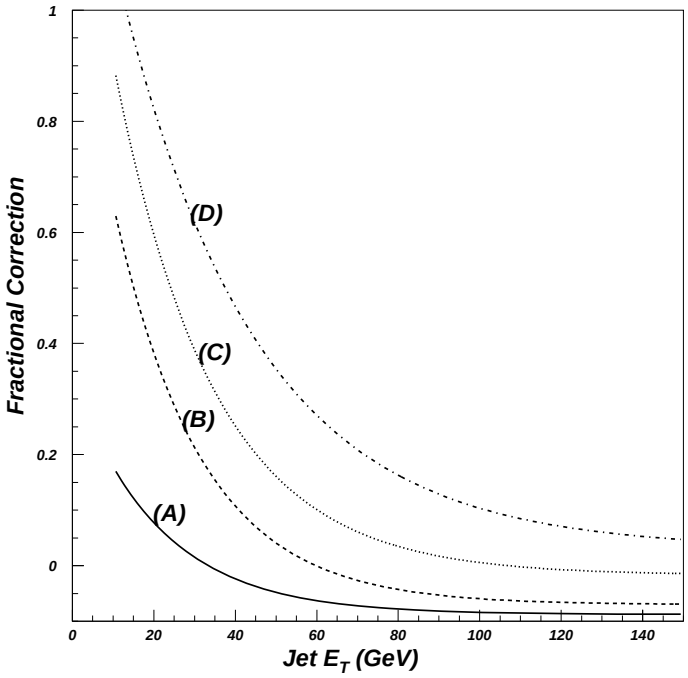

Figure 5.4: Fractional correction applied to jets due to top specific jet-parton match and tagging information. The curves are for (A) jets from the W boson decay, (B) jets from b-quarks, (C) jets from b-quarks with an SLT-e tag, and (D) jets from b-quarks with an SLT-μ tag.

for (A) jets assigned as light quarks from the W boson decay, (B) jets from b quarks without SLT tags, (C) jets from b quarks with an SLT-e tag, and (D) jets from b quarks with an SLT-μ tag. The largest corrections occur for b jets with a semi-leptonic decay due to undetected neutrinos. Figure 5.5 gives the size of the average uncertainty of the parton momentum as a function of corrected jet $\mathrm{E_T}$ for the same four classes of jets. These uncertainties are used as an estimate of a given jets resolution during the kinematic fit. Any additional jets are assigned a 10% uncertainty.

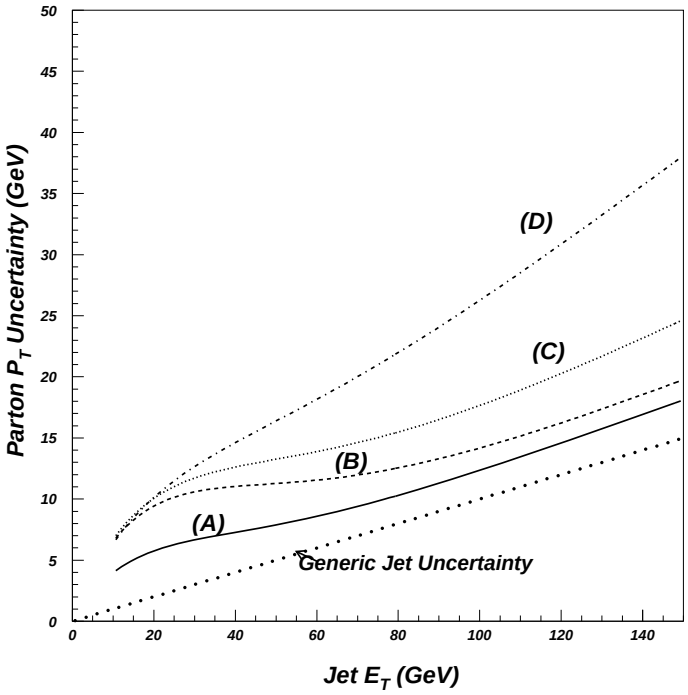

Figure 5.5: Average uncertainty in estimated parton P_T as a function of corrected jet E_T. The curves are for (A) jets from the W boson decay, (B) jets from b-quarks, (C) jets from b-quarks with an SLT-e tag, and (D) jets from b-quarks with an SLT-μ tag.

5.2.2 Unclustered Energy

The combination of the unclustered energy and any additional jets in the event form the recoil, X, against the $t\bar{t}$ system. The momentum of the neutrino from the W boson decay is defined by conservation of energy and momentum in the fit along with the W mass constraint. Energy in the calorimeter which is not clustered into a jet is summed into the unclustered energy, U. The unclustered energy receives a single correction factor of 1.6, based upon the average correction factor for 8 GeV jets. The precision of the unclustered energy measurement is not well understood. For this reason, its transverse components are assigned an error of 100%.

5.3 Performance of Reconstruction Algorithm

The reconstructed mass obtained by fitting simulated $t\bar{t}$ events depends on the intrinsic resolution of the CDF detector and, more importantly, the ability to correctly associate the daughter partons from a $t\bar{t}$ decay with the observed jets. The impact of this aspect of the kinematic reconstruction can be demonstrated by dividing a Monte Carlo sample of $t\bar{t}$ events into three categories:

- **Correctly Assigned Events:** Each of the four leading jets are within $\Delta R < 0.4$ of a parton from the $t\bar{t}$ decay and are correctly associated with the appropriate quark by the lowest χ^2 solution satisfying any imposed tagging requirements. The jet-parton match is required to be unique.

- **Incorrectly Assigned Events:** Each of the four leading jets are within $\Delta R < 0.4$ of a parton from the $t\bar{t}$ decay and each jet-parton match is unique, but the configuration with the lowest χ^2 consistent with tagging information is not the correct one.

- **Ill Defined Events:** A good match between the leading jets and partons cannot be defined. Such events are typically characterized as having extra jets produced from either initial state or final state radiation.

Figure 5.6 shows the mass distribution obtained for each of these categories and the full distribution for simulated HERWIG $t\bar{t}$ events with $M_{top} = 175$ GeV/c^2 having at least one tagged jet among the leading four. The solid histogram is the shape for reconstructed events for correctly assigned events and accounts for the peak in the overall distribution. The RMS width for correctly assigned events is approximately 13 GeV/c^2. The overall width of the reconstructed mass distribution is dominated by the incorrectly assigned events and varies from 28-36 GeV/c^2 with samples generated with higher M_{top} having larger widths.

As noted in Section 4.1.8, non-$t\bar{t}$ events are also expected in the data sample. The dominant background is expected to be due to QCD production of W bosons in association with extra jets. Figure 5.7 shows the expected mass distribution for such events as predicted

by VECBOS Monte Carlo and including the effects of the CDF detector simulation. In contrast to the $t\bar{t}$ Monte Carlo, these events exhibit a broad peak at low mass.

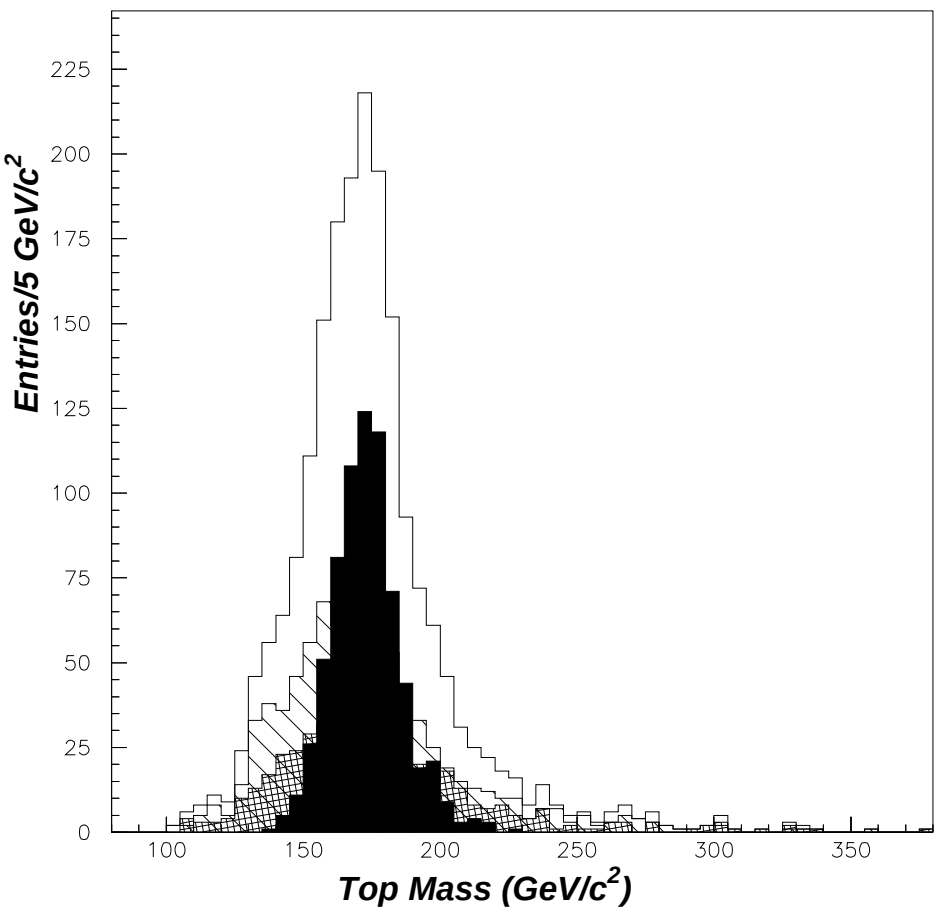

Figure 5.6: Reconstructed mass for HERWIG $t\bar{t}$ events ($M_{top} = 175$ GeV/c^2) with at least one tagged leading jet. The solid histogram shows the distribution for those events for which the selected jet-parton configuration was also the correct one. The hashed histogram shows the distribution for events where a correct assignment was ill defined. The cross hatched histogram shows the distributions for which a correct assignment could be defined but was not selected.

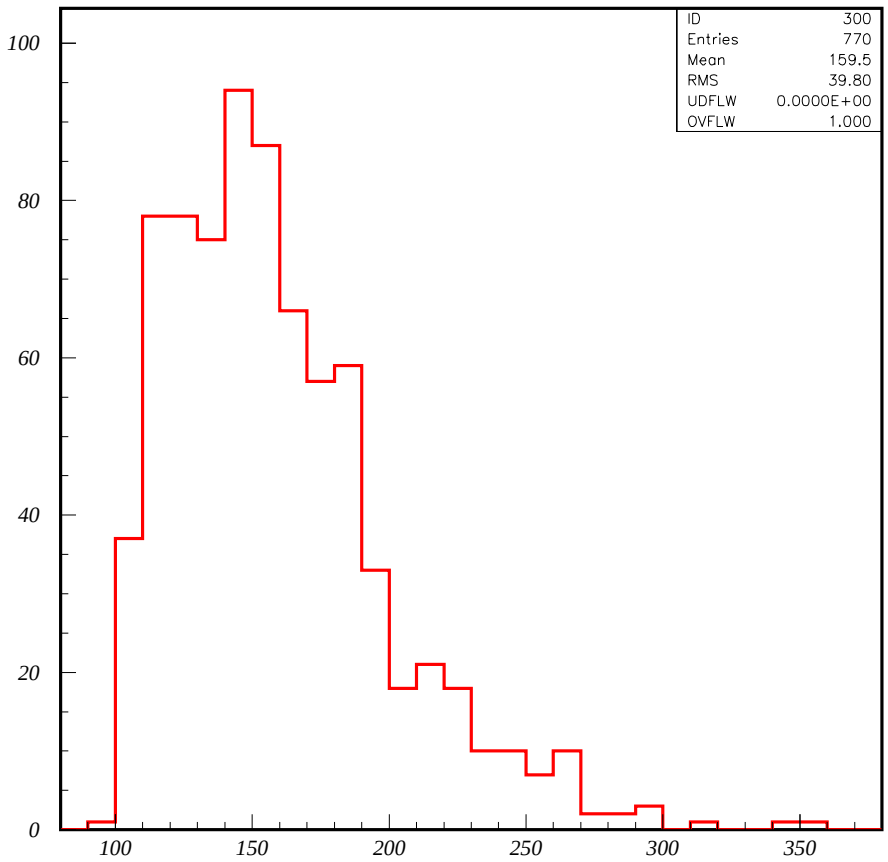

Figure 5.7: Reconstructed mass distribution for simulated background events from VECBOS Monte Carlo.

Chapter 6

Determining the Top Mass

The event reconstruction procedure results in a distribution of n top masses for a sample of n events passing all the requirements. The top quark mass is determined by comparing the shape of the reconstructed mass distribution to Monte Carlo expectations. The Monte Carlo distributions are referred to as templates. As the data sample is also expected to contain non-$t\bar{t}$ events, the comparison must include a background component. Monte Carlo samples are also used to model the expected shape for the background. The size of the background component is constrained to an independent estimate of the number of background events in the data sample. A maximum log-likelihood fit is used to compare the Monte Carlo templates to the data distribution and to determine the most likely top quark mass and statistical error.

Previous top mass measurements at CDF used a discrete likelihood method [8, 4]. That is, the likelihood function was evaluated only at top mass values for which Monte Carlo samples had been generated. The resulting points along with their associated errors were then fit with a continuous function to determine the best top mass and statistical error. In the work which follows, a continuous likelihood method is employed where the Monte Carlo templates are parametrized as functions of M_{top}. This method eliminates uncertainties associated with fitting at discrete points. The discrete approach resulted in large fluctuations in the estimated statistical error for different fitting intervals and

functions. In this respect, the continuous method provides a more robust measurement even in cases where the likelihood function has a non-standard shape.

6.1 Templates

Samples of Monte Carlo events are generated to model the physics of $t\bar{t}$ and background production observed in the data sample. The reconstructed mass distributions for these sample events are referred to as templates. The templates generated with given M_{top} specify the probability for an event with reconstructed mass, M_{rec}, to have resulted from the decay of a $t\bar{t}$ pair with the assumed mass, M_{top}. Because only a finite number of Monte Carlo events can be generated, the templates must be binned to yield an estimate for the probability. By fitting the templates to a smooth function, it is possible to obtain better estimates of the true distributions [28].

6.1.1 $t\bar{t}$ Signal

In $t\bar{t}$ Monte Carlo samples, it is observed that the shape of the reconstructed mass distribution depends on the generated top quark mass. Monte Carlo samples have been generated at 18 different top mass values ranging from $M_{top} = 120$ GeV/c^2 to $M_{top} = 220$ GeV/c^2, resulting in 18 discrete templates. The shapes of the distributions are very similar with a peak near the generated mass value and asymmetric tails. This is quite reasonable, as the physical processes responsible for the distributions are exactly the same over this mass range. Only the mass of the top quark has been changed. This gives rise to the notion that it should be possible to fit the distributions to a single functional form dependent only upon the top mass. A number of functions were examined, and it was found that the distributions are well described by the sum of a gaussian and a gamma function. In this manner, the shape of the signal, f_s, can be expressed as:

$$f_s\left(M_{fit},\vec{p}\right) = \frac{(1-p_6)}{\sqrt{2\pi}p_5}e^{-\frac{1}{2}\left(\frac{M_{fit}-p_4}{p_5}\right)^2} + \frac{p_6 p_3^{(1+p_2)}}{\Gamma\left(1+p_2\right)}\left(M_{fit}-p_1\right)^{p_2} e^{-p_3\left(M_{fit}-p_1\right)} \tag{6.1}$$

where Γ is the Euler function, M_{fit} is the fitted mass, and the p_i's are the parameters of the gamma and gaussian functions. The parameters themselves are linear functions of the input top mass:

$$p_i = \alpha_i + \alpha_{i+6}\,(M_{top} - 175) \tag{6.2}$$

where M_{top} is the input top mass. This yields a total of twelve free parameters. The nominal values for these parameters along with their errors are determined from a simultaneous fit to all 18 top Monte Carlo templates.

The fit does a good job of describing the distributions obtained from the Monte Carlo samples. Figure 6.1 shows the agreement between the discrete templates and the fit for nine of the discrete templates. An advantage to using the single smooth function is a reduction in the sensitivity to statistical fluctuations of individual templates. Information from all the templates is used to determine the shape, effectively increasing the statistical power. One concern of this procedure is that high statistics samples (say at 175 GeV/c^2 for example, where many more Monte Carlo events have been generated than at at extreme mass values) may bias the fit. Several checks have been made:

- The reduced χ^2 for the fit is 1.085 per degree of freedom which indicates a good fit.
- The pull distributions for each bin in the discrete templates have means distributed about 0.0 as shown in Figure 6.2 and widths distributed about 1.0 as shown in Figure 6.3. The figures show the average means and widths over all bins in each discrete template.
- The fit was repeated with the high statistics 175 GeV/c^2 template removed. The resulting $f_s(M_{top} = 175)$ agrees very well with the 175 GeV/c^2 template.

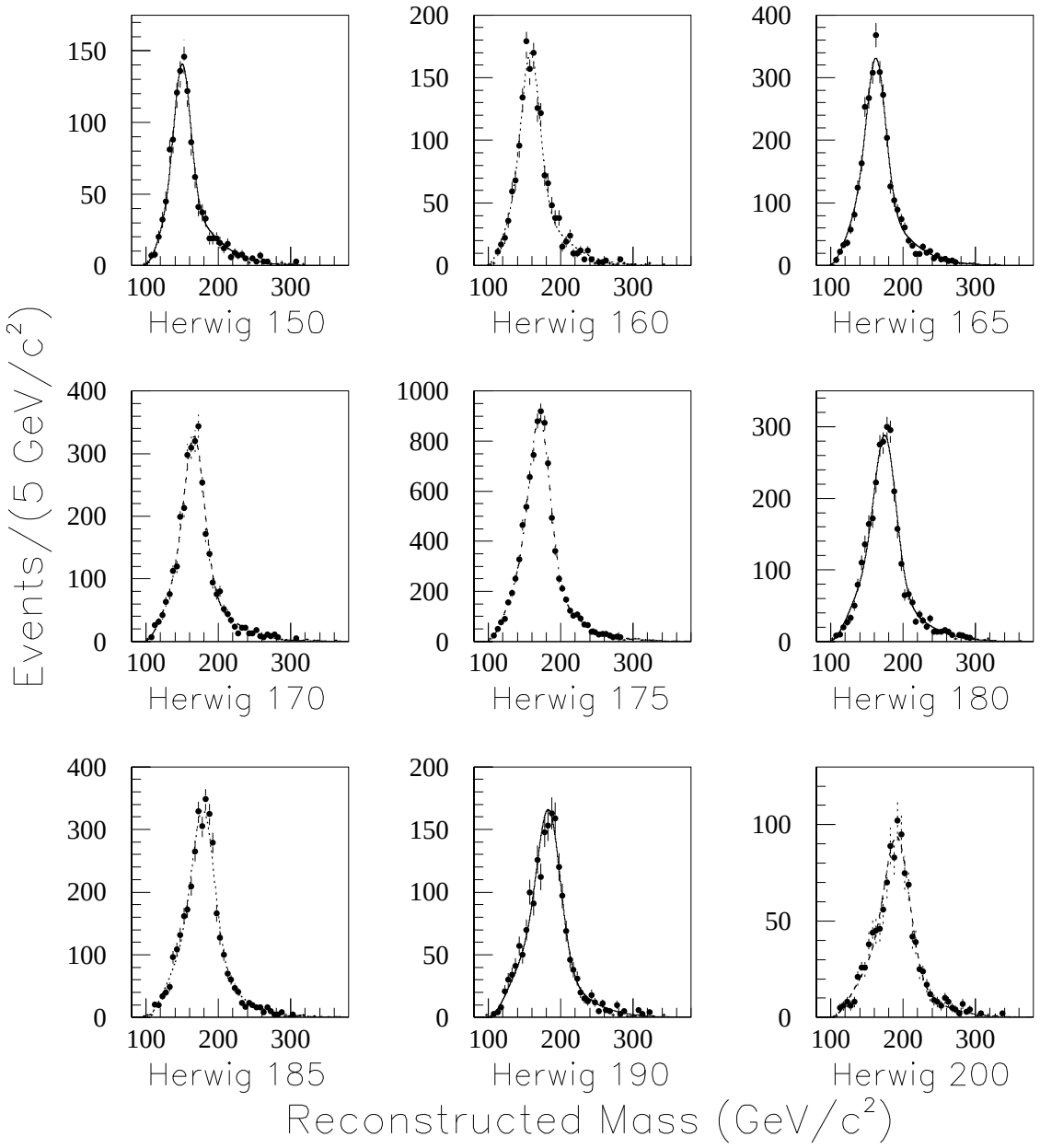

Figure 6.1: Fit to HERWIG Monte Carlo templates using the fit described in the text.

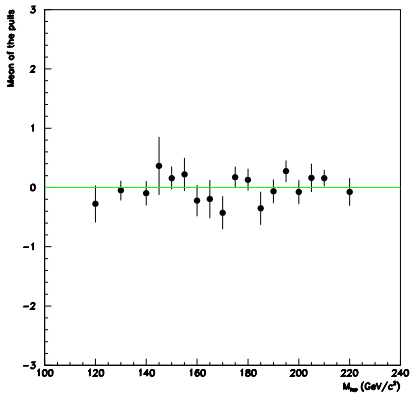

Figure 6.2: Mean of the pull distributions for the 18 Monte Carlo $t\bar{t}$ templates.

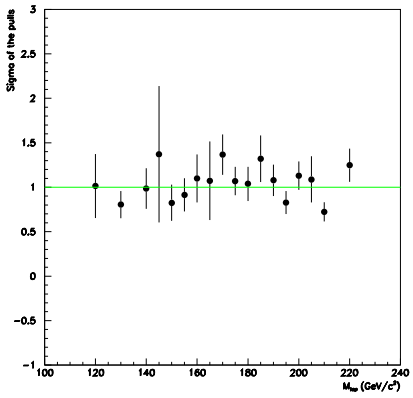

Figure 6.3: Width of the pull distributions for the 18 Monte Carlo $t\bar{t}$ templates.

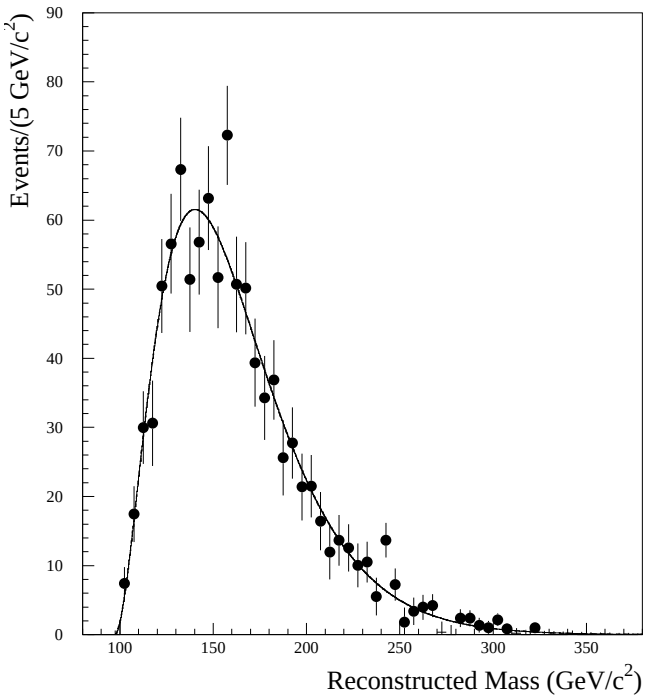

Figure 6.4: Fit to the VECBOS W+jet template.

6.1.2 QCD W+jets Background

As noted in the last chapter, the VECBOS Monte Carlo generated events are used to model the background shape. For a continuous likelihood fit, these events must also be fit to a smooth function. The same functional form used to fit the $t\bar{t}$ signal templates is used to fit the background template. The mass dependence is removed, so there are just six parameters, $\alpha_{13} - \alpha_{18}$, which describe the background parametrization. The fit to the background shape is shown in Figure 6.4. Note that in the case of the background, the fit simply provides a smooth template and does not provide any additional information.

6.2 Background Calculation

The size of the background content of the sample is estimated from expected efficiencies for known background sources described in Section 4.1.8. These efficiencies are extrapolated from the efficiencies used in the lepton + jets channel, $t\bar{t}$ cross section measurement [29]. The numbers are modified to account for the effect of the $\chi^2 < 10.0$ requirement, the loosened fourth jet selection, and the requirement that the b-tag is associated with one of the leading four jets.

Because the SVX and SLT tagging algorithms have different efficiencies, the observed events are categorized in disjoint subsets for the background estimation. The subsets are events with only SVX tags, events with only SLT tags, and events with both SVX and SLT tags. Further, because some efficiencies are based upon jet kinematics, each subset is divided into a 3.5 jet and a 4 jet subsample. The 3.5 jet sample, consists of events with three jets passing the tight cuts and a fourth jet passing the loose cuts, while the four jet sample has four jets passing the tight cuts. For a given subset j, the expected number of events, $N_{pred,j}$, is expressed as:

$$N_{pred,j} = a_j \times N_{t\bar{t}} + b_j \times N_W + N_{abs,j} \tag{6.3}$$

where $N_{t\bar{t}}$ is the number of $t\bar{t}$ events expected, N_W is the number of QCD W+jet events expected, and $N_{abs,j}$ is the absolute number of non-W background events expected in the subsample. The parameters a_j and b_j are obtained from known rates and efficiencies for each subsample.

The values of $N_{t\bar{t}}$ and N_W can be varied to optimize the agreement between the predicted and observed numbers of events. This is accomplished by maximizing the following log-likelihood:

$$L = \sum_i log(\frac{N_{pred,j}}{\sum_j N_{pred,j}}) \tag{6.4}$$

where the sum runs over the observed events in the selected subsets. The results of this procedure are shown in Table 6.1. The likelihood also provides a probability function and associated negative log-likelihood for the number of background events expected. Figure 6.5

shows the expected shapes of these distributions. As described in the next Section, the log-likelihood shape is used to constrain the background content when fitting to determine the top mass.

Sample	N_{pred}	N_{obs}	Bkg. Frac.	N_{bkg}
SVX only	17.8	13	0.11 ± 0.04	1.5
SLT only	11.8	14	0.42 ± 0.09	5.9
SVX and SLT	3.9	7	0.07 ± 0.04	0.5
Tagged Events	33.5	34	0.23 ± 0.04	7.9

Table 6.1: The predicted and observed numbers of events along with the calculated background fractions and expected number of background events in each subsample. The totals for the tagged sample are also shown.

6.3 Likelihood Fit

A maximum log-likelihood method is used to extract the top mass measurement. The likelihood is used to characterize the similarity between the reconstructed masses of the data events and the Monte Carlo models for $t\bar{t}$ and background. The likelihood yields the most probable value of M_{top} to have generated the observed data distribution. The likelihood contains three components:

$$\mathcal{L} = \mathcal{L}_{shape} \times \mathcal{L}_{background} \times \mathcal{L}_{param} \tag{6.5}$$

where:

$$\mathcal{L}_{shape} = \prod_{events}(1 - x_b) f_s(M_{event}, M_{top}) + x_b f_b(M_{event})$$
$$\mathcal{L}_{background} = \mathcal{P}(x_b)$$
$$\mathcal{L}_{param} = e^{\frac{1}{2}(\vec{\alpha}-\vec{\alpha}_0)^T V^{-1}(\vec{\alpha}-\vec{\alpha}_0)}$$

The term $\mathcal{L}_{shape}$ describes the joint probability density for a sample of events with masses, M_{event}, to have come from a parent distribution with a signal fraction of $(1 - x_b)$ and a background fraction of x_b. The probability distributions, f_s and f_b, depend upon the

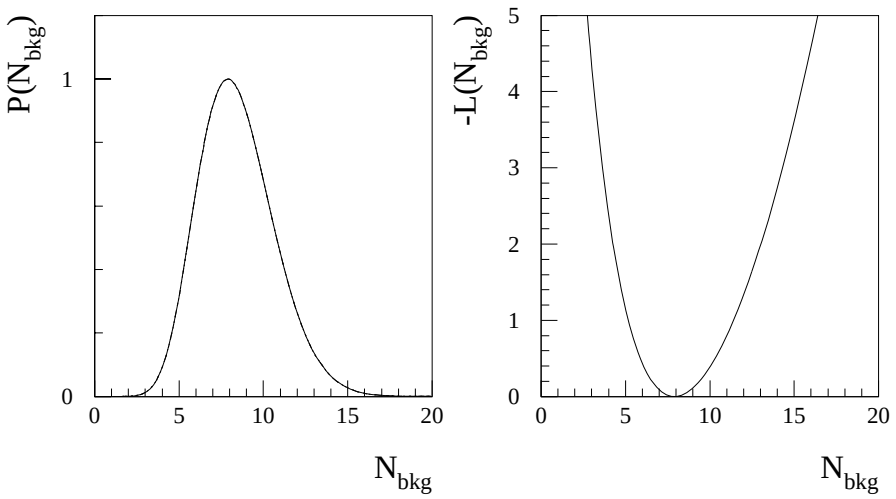

Figure 6.5: Probability distribution for the expected number of background events and the corresponding negative log-likelihood.

parameters, $\vec{\alpha}$, as described in Section 6.1. The background fraction, x_b, is constrained by the probability distribution derived from the background calculation. The 18 parameters, $\vec{\alpha}$, which describe the signal and background templates are allowed to vary from their fitted values, $\vec{\alpha}_0$, during the fit. V is the covariance matrix for the parameters. The inclusion of this term in the likelihood takes into account the finite Monte Carlo statistics used to determine the shape of f_s and f_b. The likelihood $\mathcal{L}$ is maximized with respect to M_{top}, x_b, and $\vec{\alpha}$. Note, that M_{top} is the only free parameter in the fit. All other parameters are constrained. The best M_{top} is that value which minimizes the log-likelihood expression.

6.3.1 Checks

A number of checks can be performed to insure that the likelihood is behaving properly. Monte Carlo pseudo experiments are used to test the performance of the likelihood. The pseudo experiments consist of 34 events which are generated with a varying amount of signal and background events. The exact number of signal and background events in a given experiment is determined from a Poisson fluctuation of the expected number of background events in the data (7.9 events). The signal event masses are generated from the parametrized $t\bar{t}$ templates with a fixed M_{top}, and the background events are generated from the parametrized background template. Unless otherwise stated, 5000 experiments are run for each test.

The most basic question is, if events are generated from a template with mass, M_{gen}, does the fit return the same mass? To answer this, pseudo experiments are generated at a number of different top masses and fit via the likelihood procedure. The median of the fitted masses, M_{fit}, is plotted vs. the generated mass in Figure 6.6. As expected, the points lie along a line with slope of 1.0. A further check, is to look at the pull distribution for the fitted masses. Here the pull is defined as the fitted mass minus the generated mass divided by the statistical error returned from the fit. If the fit is returning the correct mass and statistical error, the pull distribution will have a mean of 0.0 and a width of 1.0. Figure 6.7

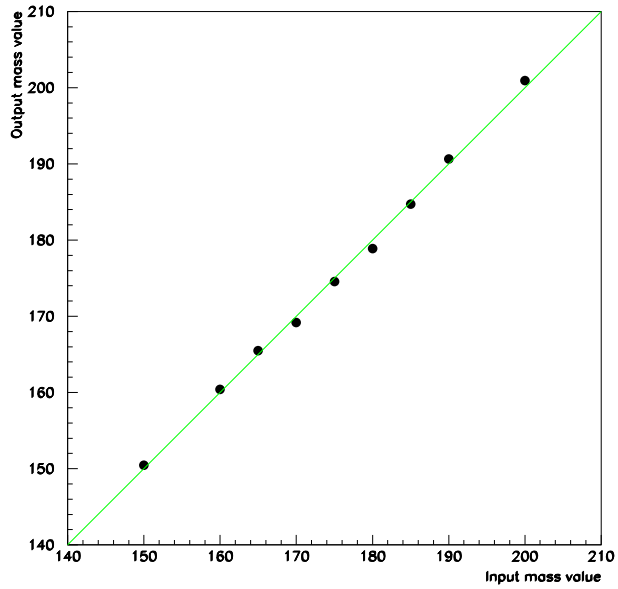

Figure 6.6: The median fitted mass vs. the input mass for many samples of simulated experiments.

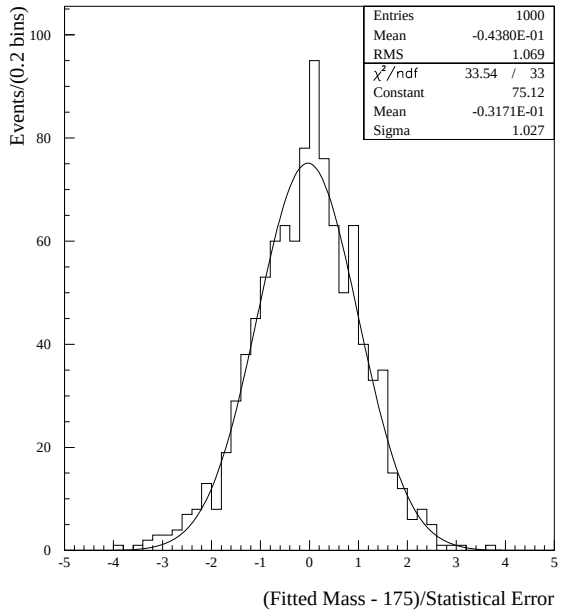

Figure 6.7: The pull distribution for a large number of pseudo experiments generated with $M_{top} = 175$ GeV/c^2.

shows the pull distribution for pseudo experiments generated with $M_{top} = 175$ GeV/c^2. The distribution shows good agreement with the expectation.

6.3.2 Data Results

Having confirmed the likelihood provides consistent results, the method can now be applied to the 34 event data sample. The likelihood fit yields:

$$M_{top} = 173.5 \pm 6.0 \mathrm{GeV/c^2} \tag{6.6}$$

$$x_b = 0.21^{+0.06}_{-0.05}$$

where the errors arise from a half unit change in minus log-likelihood with respect to its minimum and reflect the statistical uncertainty from both the data and the Monte Carlo statistics. The fitted background fraction, x_b, translates to 7.3 ± 1.8 background events used in the fit. The reconstructed mass distribution along with the fitted results are shown in Figure 6.8. The inset shows the shape of the likelihood as a function of the top mass.

To check the result, Monte Carlo pseudo experiments are generated at the same mass to determine how likely the returned statistical error is. Figure 6.9 shows the returned statistical error from the pseudo experiments. An arrow denotes the statistical error which is observed in the data. An equal or smaller error is observed in 20% of the pseudo experiments.

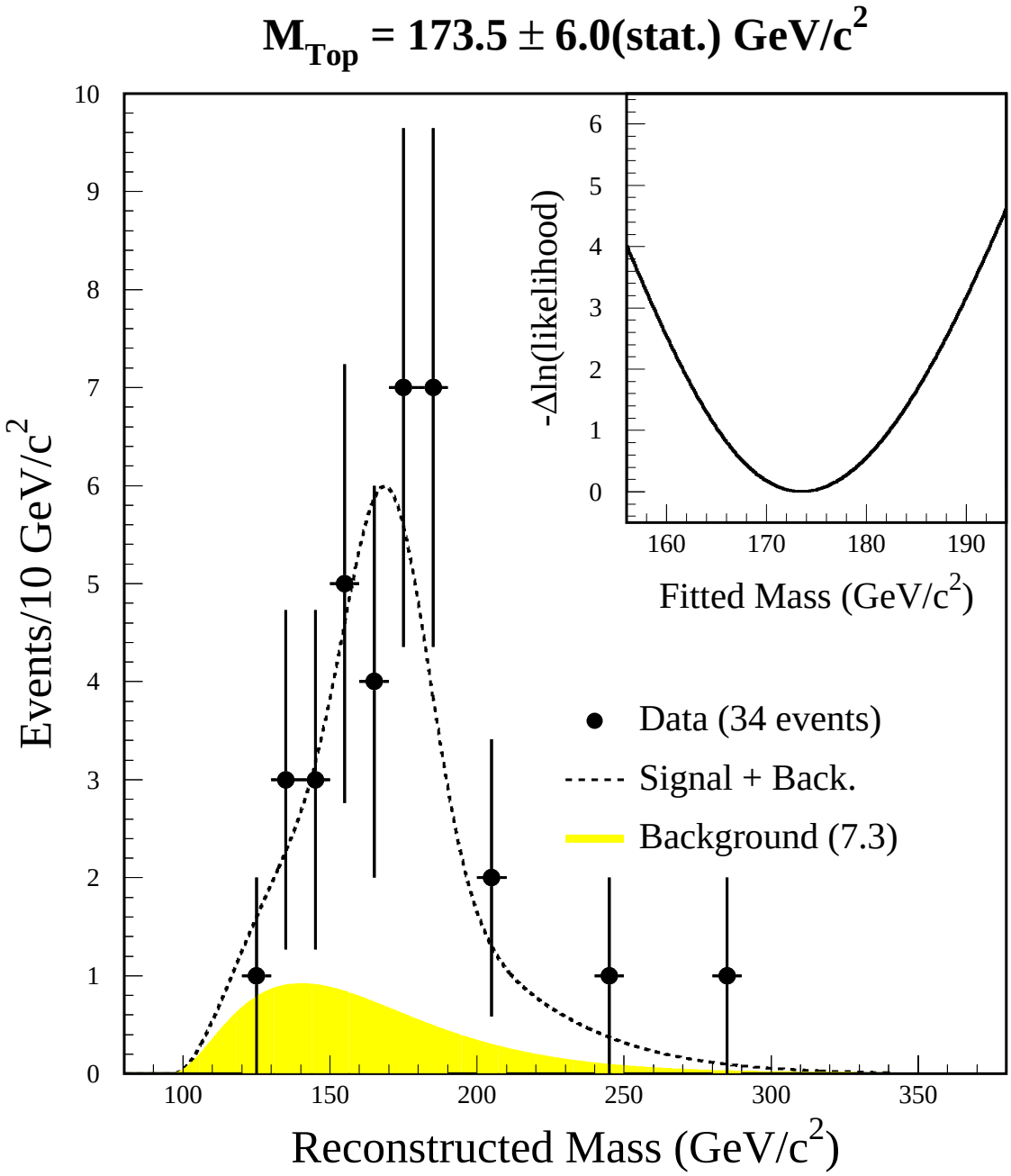

Figure 6.8: Reconstructed mass distribution for the 34 tagged data events along with the results of the fit. The shaded region denotes the background contribution, while the solid curve is the result of the best fit combining the signal and background components. The inset shows the shape of the negative log-likelihood function.

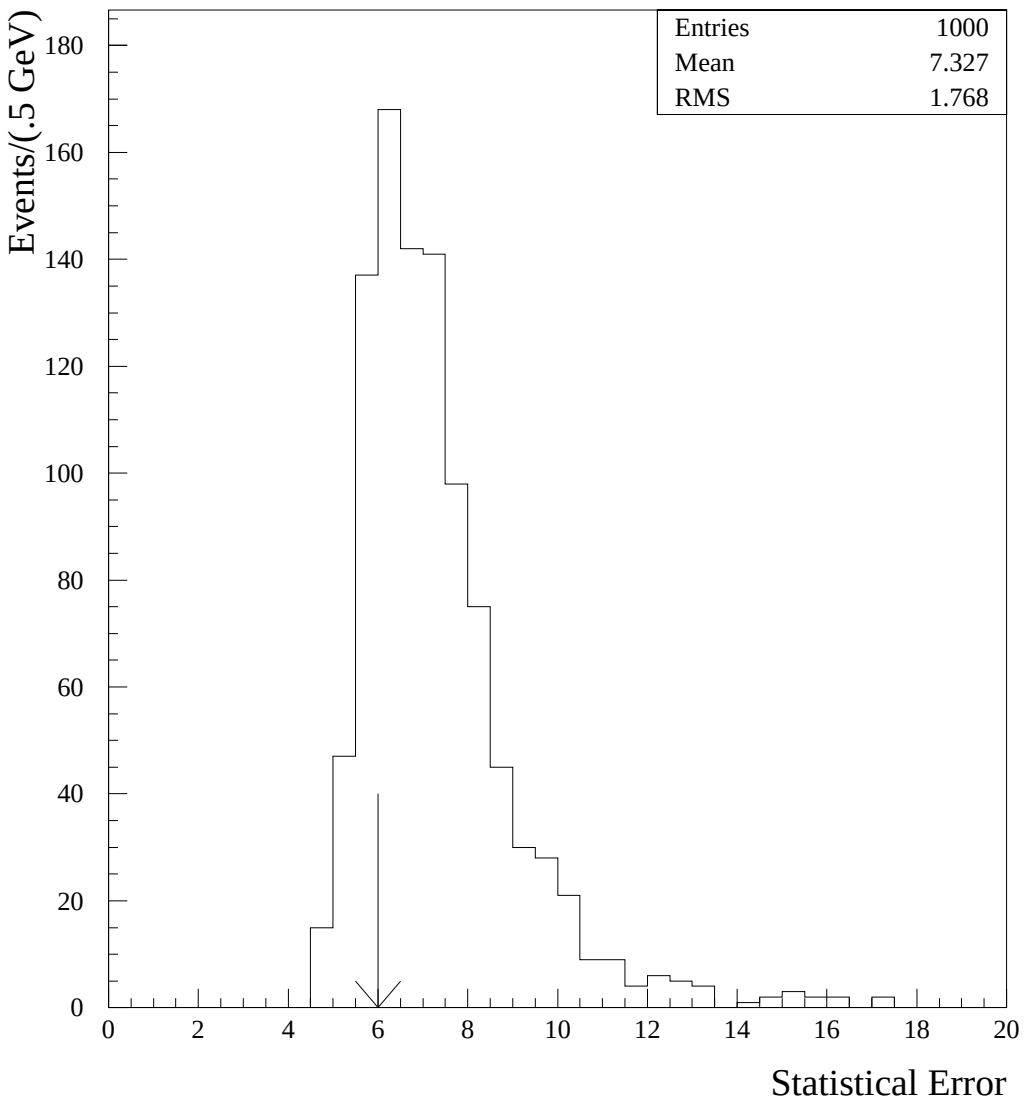

Figure 6.9: Distribution of returned statistical errors in the Monte Carlo pseudo experiments. The arrow shows the returned statistical error for the data.

Chapter 7

Systematic Uncertainties

The top mass measurement is subject to a number of uncertainties related to the measurement procedure as well as uncertainties in the simulations used to model the underlying physics. The total systematic uncertainty is assigned to account for possible biases in the top mass measurement due to these uncertainties. The main sources of uncertainty arise from the detector performance in reconstructing jets and the theoretical models used to describe the physics processes involved.

The magnitude of each systematic uncertainty is evaluated in the same manner. Because event samples with low statistics are involved, many Monte Carlo pseudo experiments, described in Section 6.3.1, are used to decouple systematic biases from statistical fluctuations. Using this procedure, the systematic uncertainty is taken as the observed shift in the median top mass between experiments generated from the default conditions and experiments generated with the condition under study varied within its uncertainty. As an example, to evaluate the systematic shift due to uncertainty in the jet energy scale, Monte Carlo events are reconstructed after all jets have been shifted either up or down (done separately) in energy. This is done for both HERWIG $M_{top} = 175$ GeV/c^2 and VECBOS background samples and the resulting reconstructed mass distributions are parametrized. These templates are then used to generate a set of 5000 pseudo experiments which are fit in the exact same manner as performed on the data. The resulting distribution of fitted masses is then compared with the distribution from pseudo experiments generated from de-

fault top and background probability distributions. The difference in the medians of these distributions is taken as the systematic uncertainty.

Using this procedure, potential shifts can be determined to within 0.2 GeV/c^2. It is not possible to determine shifts smaller than this with the size of the Monte Carlo event samples currently available. This limit was evaluated by generating experiments from top and background probability distributions shifted up or down one sigma by their statistical uncertainty. Thus, the innate uncertainties on the fitted templates gave rise to a 0.2 GeV/c^2 uncertainty in the median mass returned from the pseudo experiments.

It is important to note that for most of the potential sources of systematic error the critical component is whether there is coupling of the uncertain quantity to the top mass which is different in the data than is in the Monte Carlo. If a systematic shift is present in both, then there is no net effect on the final measured value of M_{top}. Ultimately, this is due to the use of the likelihood procedure which selects the Monte Carlo best able to reproduce the kinematics observed in the data. If both the Monte Carlo and data are systematically shifted in some manner, then the best fit value is unchanged.

7.1 Jet-Parton E_T Scale

The event reconstruction algorithm varies the transverse momenta of partons to fit the kinematics of the hypothesized $t\bar{t}$ decay. As outlined in Section 5.2.1, a number of corrections are performed to provide the best estimate of the original parton momenta based upon the measured energy of an observed jet. Potential systematic uncertainties arise from differences in the jet-parton E_T scales between Monte Carlo and data. The uncertainty can be decomposed into a source based upon detector effects and soft gluon effects.

7.1.1 Detector Effects

The systematic uncertainty in the jet-parton E_T scale due to detector effects results primarily from limitations in the modeling of the calorimeter response to incident particles

within the jet clustering cone. It is composed of an uncertainty for calorimeter calibration and an uncertainty for calorimeter stability. The calibration uncertainty is obtained by varying each of the pion, electron, and photon responses by one sigma and adding the effect of each in quadrature. The sizes of these uncertainties are quantified through Figure 7.1. This also includes an uncertainty on primary vertex underlying correction (which is discussed below) and fragmentation effects. An additional uncertainty of 1% is taken for calorimeter uncertainty. It is applied to the uncorrected jet E_T.

As noted in Section 5.2.1 the underlying event correction has two components; one for the primary vertex and another to account for multiple interactions in the same beam crossing. The uncertainty for the primary vertex is taken as 30% of the correction itself and is included above and shown in Figure 7.1. The uncertainty for the multiple vertex correction is taken as 100 MeV per additional vertex.

In addition to the response of the central calorimeter, an additional systematic is assigned due to variations in the relative response between the calorimetry in the central region and that in the plug and forward regions ($1.1 < |\eta|$ and > 2.4 respectively). The calorimeter response in these regions is calibrated relative to that in the central through the use of dijets, and the precision to which this calibration is known is limited solely by the number of dijet events available and varies as a function of detector position. The uncertainty is larger in the cracks of the detector due to poorer resolution and smaller statistics. Table 7.1 gives the percent uncertainty on the relative correction for various detector η ranges.

$\|\eta\|$ interval	% Uncertainty on Relative Correction
0.0 - 0.1	2%
0.1 - 1.0	0.2%
1.0 - 1.4	4%
1.4 - 2.2	0.2%
2.2 - 2.6	4%

Table 7.1: The percentage uncertainty on the relative jet energy correction for various detector η regions.

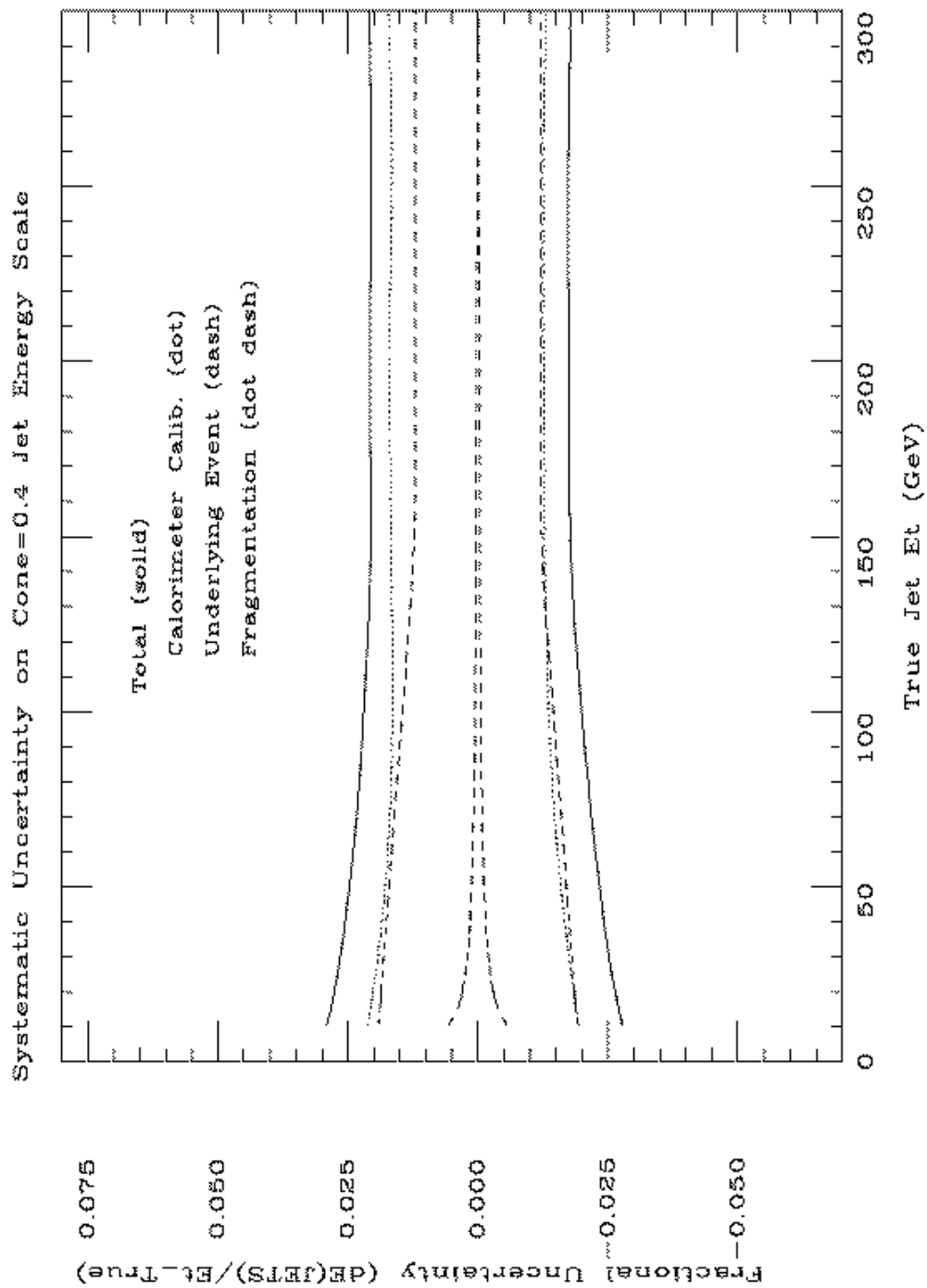

Figure 7.1: Uncertainty in jet E_T scale as measured within a jet clustering cone of size 0.4. The vertical axis shows the extent to which the measured jet E_T response varies due to different systematic effects.

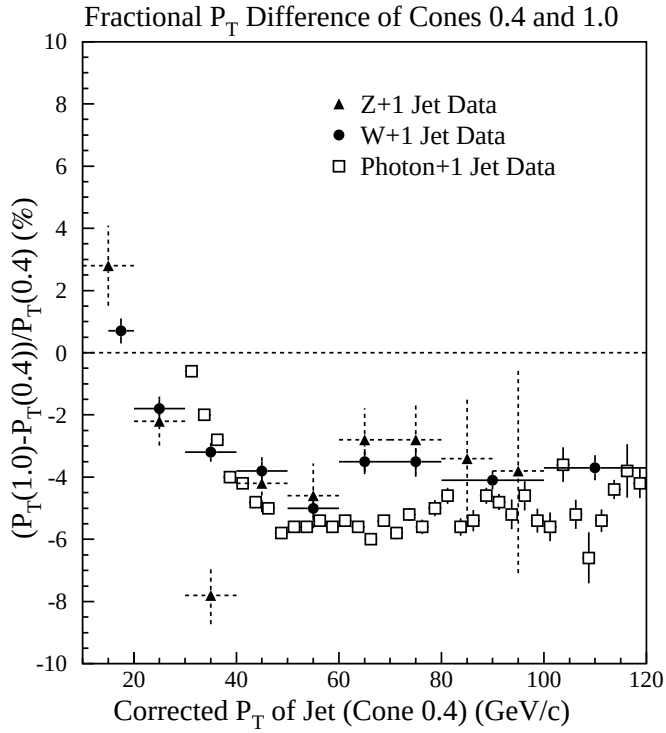

Figure 7.2: Fractional jet E_T in annulus from data samples of W, Z, and γ events.

7.1.2 Soft Gluon Effects

The second source of systematic uncertainty on the jet-parton E_T scale arises due to modeling of jet formation. It has been termed soft gluon effects due to the fact that low energy gluons are produced during parton fragmentation into jets. The number and energy of gluons produced affects the shape of the jet and can carry energy from the initial parton outside of the jet clustering cone. As described in Section 5.2.1, a parton specific correction factor is applied to jets to provide the best estimate of the original parton momenta. This correction factor is derived from HERWIG $t\bar{t}$ Monte Carlo as a function of the corrected E_T measured in a clustering cone of 0.4. Thus, it is very susceptible to potential differences in jet shape between Monte Carlo jets and jets present in the data.

The soft gluon systematic uncertainty is studied by probing the transverse energy flow around the jet axis in single jet data. Studies have been conducted upon single jets produced in association with W, Z, and γ bosons. To study jet flow outside a cone of

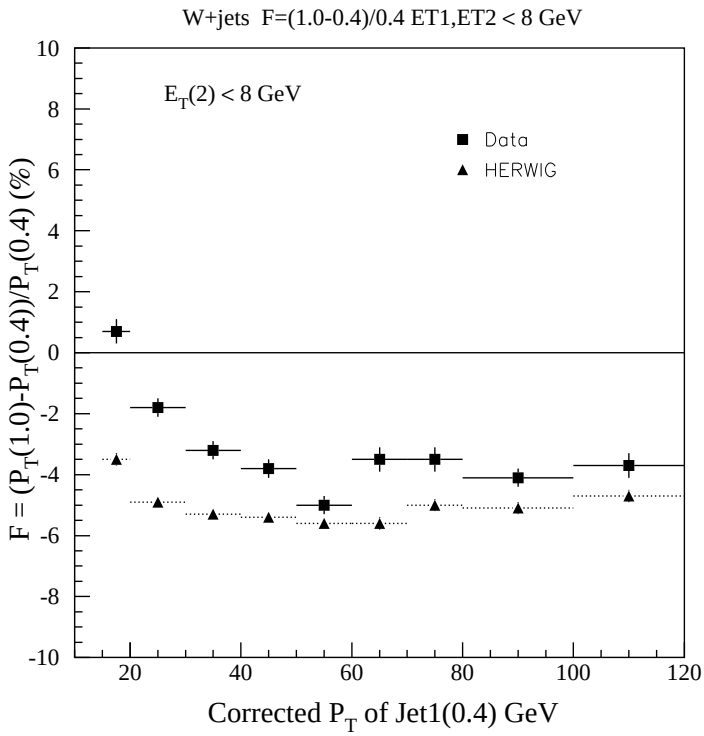

Figure 7.3: Fractional jet E_T in annulus from $W + 1$ jet events observed in data and from HERWIG Monte Carlo.

0.4, the jet in these events is clustered using a cone of 0.4 and 1.0. The jet then receives the standard corrections applicable to the appropriate cone size. Figure 7.2 shows the fractional difference in jet E_T observed between a cone or 0.4 and 1.0 for each of the data samples examined. Note that each sample exhibits the same E_T dependent shape. As it has the largest statistics, the $W + 1$ jet sample is used to quantify the soft gluon systematic uncertainty. Figure 7.3 shows the same plot for the $W + 1$ jet events from both the data and HERWIG Monte Carlo. Note the discrepancy between the data and Monte Carlo especially at low E_T. This discrepancy leads to an uncertainty for corrected jets which ranges from 6% at low E_T to about 1.4% at high E_T and is applied to all jets. Finally, an additional uncertainty of 1.0 GeV is taken for energy lying outside a cone of $\Delta R = 1.0$.

Effect	E_T Scale Uncertainty
Absolute Jet Energy (includes single vertex UE)	≈2.5%
Calorimeter Stability	1.0%
Underlying Event (for multiple vertices)	100 MeV/vertex
Relative Jet Energy	0.2-4% of f_{rel}
Soft Gluon Radiation	6-1.4%
Energy Outside Cone 1.0	1 GeV

Table 7.2: The approximate size of the uncertainties on the jet energy scale.

7.1.3 Summary of Jet-Parton E_T *Scale Uncertainties*

Table 7.2 shows the approximate size of each E_T scale uncertainty. Each of the jet-parton E_T systematic shifts are added in quadrature and applied in both the positive and negative direction to all jets to determine the systematic uncertainty on the measurement of the top mass. The positive and negative shifts are symmetrized to produce the final systematic. The final systematic uncertainty on the top mass is 4.1 GeV/c^2.

7.2 Initial and Final State Hard Radiation

Modeling of jet production can affect the estimate of the top mass in other ways. A significant component of the resolution with which the top mass is estimated is due to the presence of jets that originate from QCD radiative processes. QCD radiation which produces jets can originate from the outgoing (Final State) or incoming (Initial State) partons, the $t\bar{t}$ quarks, or from interference among the three. The latter two effects are expected to be small so that the effects studied here correspond to Initial State Radiation(ISR) and Final State Radiation(FSR). For a detailed account of methods used to examine gluon radiation in top events at CDF, see [30].

The effects of the modeling of hard gluon radiation on the measurement of the top mass are studied using the PYTHIA Monte Carlo program, which allows the two effects to be

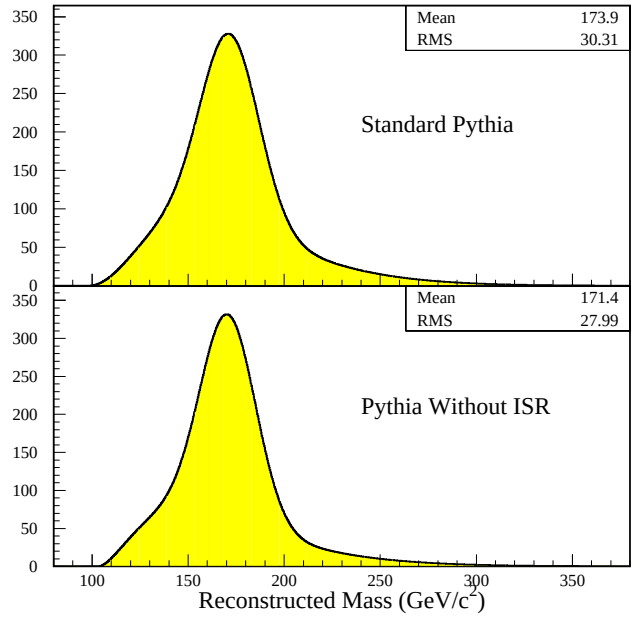

Figure 7.4: Reconstructed mass distributions for Pythia Monte Carlo with ISR and without ISR.

studied in isolation from one another. Figure 7.4 shows the reconstructed mass distribution expected from simulated samples of $t\bar{t}$ with and without ISR. In such an environment, analysis with ensembles of simulated experiments indicate that the measurement of the top mass would be biased by 2.1 GeV/c^2 were ISR not present at the estimated level. To arrive at a systematic uncertainty on the measured top mass, this bias is assumed to represent the maximum bias possible due to overestimating the amount of Initial State radiation. Assuming further that an equal but positive bias would correspond to underestimating the amount of radiation and that no amount of ISR is more likely than any other, the systematic uncertainty is estimated as

$$\sigma^{ISR}(M_{top}) = 2 \times \frac{2.1 \text{ GeV/c}^2}{\sqrt{12}} = 1.2 \text{ GeV/c}^2$$

(7.1)

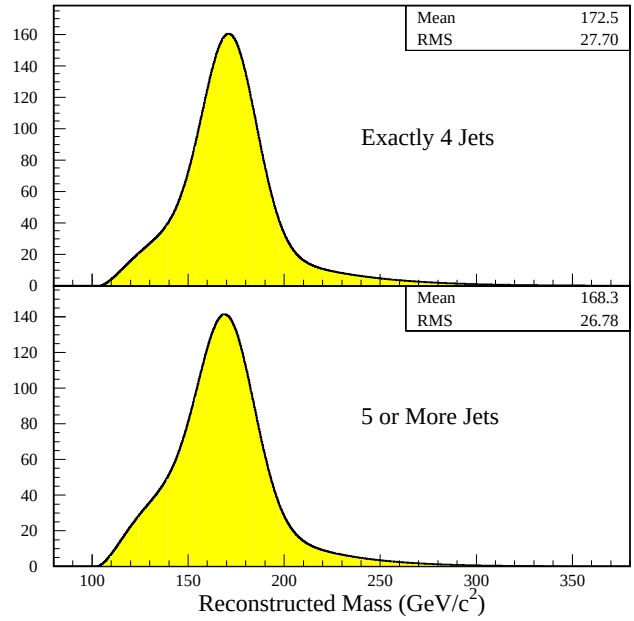

Figure 7.5: Reconstructed mass distributions for Pythia Monte Carlo for events with exactly 4 jets (no FSR) and events with more than 4 jets (extra jets from FSR).

Extracting the effects due to Final State Radiation is a more subtle exercise because PYTHIA, like HERWIG, describes jet formation through a parton shower which ascribes the entirety of a jet to FSR. The uncertainties in modeling the softer gluon components on the measurement of the top mass are included in the studies described above for soft gluon radiation. To study the effect of FSR which induces additional observed jets, simulated samples of $t\bar{t}$ events were studied without Initial State Radiation. A reasonable assumption is that extra jets observed in such events are due to Final State Radiation. The subset of this sample that had additional jets are therefore classified as events with FSR and those with exactly four jets as non-FSR events. Figure 7.5 shows the corresponding M_{top} distributions for the two types of events. Relying on these subsamples to represent the extremes of the

FSR model, there is a 3.5 GeV/c^2 shift between the no FSR and all FSR cases. Assuming equal probability for all amounts of FSR, the estimated systematic uncertainty for modeling FSR is then calculated as

$$\sigma^{FSR}(M_{top}) = \frac{3.5}{\sqrt{12}} = 1.0 \text{ GeV/c}^2 \tag{7.2}$$

7.3 Background Mass Distribution

The background systematic uncertainty accounts for uncertainty in the shape of the background mass distribution. The background distribution used in determining the top mass is generated from VECBOS Monte Carlo with a $Q^2 =< P_t^2 >$ scale. The Q^2 scale is a measure of the momentum transferred in a collision between partons and effects the scale of the coupling constants involved. To vary the background shape, VECBOS events were generated with $Q^2 = M_W^2$ scale. Figure 7.6 shows the reconstructed mass distributions for both Q^2 scales. The difference results in a systematic uncertainty of 0.3 GeV/c^2. See Appendix C for studies on how well VECBOS models the expected backgrounds.

7.4 B-tagging Bias

A b-tagging bias leads to an uncertainty in the top mass due to the uncertainty in SVX and SLT tagging efficiency versus E_T and the rate of tagging non-b jets in real top events. The SVX tagging efficiency is determined from Monte Carlo and then corrected by a scale factor. The scale factor is determined from data using CTC tracking studies. The bias is evaluated by varying the scale factor. This results in a 0.1 GeV/c^2 systematic uncertainty for the SVX tags. The SLT uncertainties are determined from high statistics data samples of $\psi \rightarrow \mu\mu$ and $\gamma \rightarrow ee$. These samples have been well studied and the residual uncertainties are small. The relevant uncertainty for SLT tags arises in the ratio of real to fake SLT tags in top events. This ratio has a 10-20% uncertainty. It is conservatively evaluated as half the difference between the resulting mass for all real SLT tags and all fake

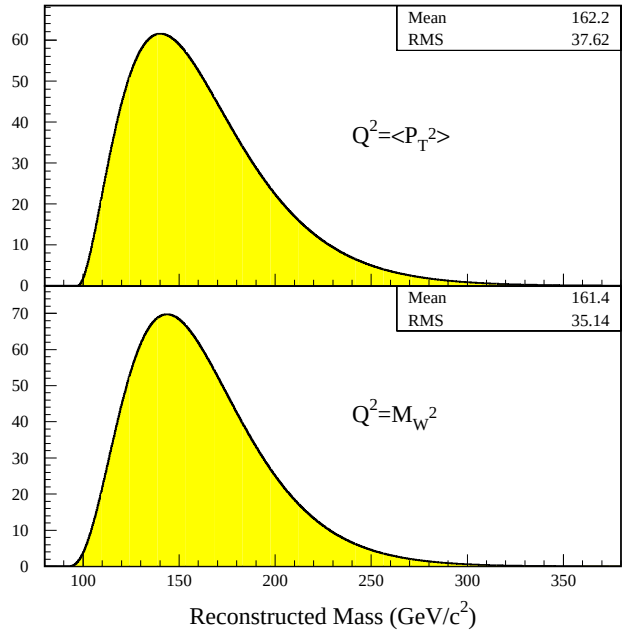

Figure 7.6: Reconstructed mass distributions for VECBOS Monte Carlo generated with $Q^2 =< P_T^2 >$ and $Q^2 = M_W^2$ scales.

SLT tags. This results in a 0.4 GeV/c^2 systematic uncertainty for the SLT tags. Added in quadrature, the final result is 0.4 GeV/c^2 for the b-tagging bias.

7.5 Parton Distribution Functions

A parton distribution function (PDF) describes how the momentum fraction of the partons inside of a hadron is distributed. All of the Monte Carlo samples used to measure the top mass were generated with the MRSD0' parton distribution function. This was the preferred PDF at the time the samples were generated. Newer distribution functions now exist, in particular ones which fit CDF's inclusive jet cross section. One such PDF, CTEQ4L, provides a reasonable variation in gluon distribution compared to MRSD0'. The mass shift between samples generated with the two PDF's yields an uncertainty of 0.5 GeV/c^2.

7.6 Monte Carlo Generators

The effect of using different Monte Carlo generators has also been studied. Previously, the uncertainty was evaluated by examining the difference between the HERWIG and ISAJET generators. Studies of various kinematic distributions have shown ISAJET to have poor agreement with the data [21]. In particular, it appears that most of the difference between HERWIG and ISAJET is in the amount of initial and final state radiation present which is already accounted for in a separate systematic. Given this information, the Monte Carlo systematic uncertainty is evaluated using the difference between the HERWIG and PYTHIA generators. This gives a systematic uncertainty of 0.5 GeV/c^2.

7.7 Summary of Systematic Uncertainties

All of the relevant systematic uncertainties studied for the top mass measurement are listed in Table 7.7. Combining all of these effects in quadrature gives a total systematic uncertainty of 4.9 GeV/c^2.

Source	Value (GeV/c^2)
Jet Energy Measurement	4.1
Initial and Final State Radiation	1.6
Shape of Background Spectrum	0.3
b Tab Bias	0.4
Parton Distribution Functions	0.5
Monte Carlo generator	0.5
Total	4.5

Table 7.3: Systematic Uncertainties

Chapter 8

Conclusions

Using techniques described in this thesis, the mass of the top quark has been measured using a sample of b-tagged lepton plus jet events to be $173.5 \pm 6.0(stat.) \pm 4.8(syst.)$ GeV/c^2. Adding the uncertainties in quadrature yields a result of 173.5 ± 7.0 GeV/c^2 for the top quark mass. It is interesting to note that though a relatively small number of top quark candidates have been observed, it already has the smallest fractional uncertainty of any of the quark masses.

As described in Chapter 2, a measurement of the top quark mass along with a measurement of the W boson mass places bounds on the mass of the Higgs boson. The current CDF W mass measurement along with the result from this thesis are shown in Figure 8.1 superimposed upon the Standard Model Higgs theory curves. The latest CDF W mass is 80.375 ± 0.120 GeV/c^2 [31]. The current data favors a lighter Higgs mass but has a very strong dependence on the mass of the W boson.

The next chance to study the top quark will occur in Run II at the Tevatron collider, which is planned to begin taking data in 2000. For Run II, the Tevatron is being upgraded to deliver an order of magnitude greater instantaneous luminosity and to have $\sqrt{s} = 2.0$ TeV. These improvements should result in a factor of about fifteen increase in the production of $t\bar{t}$ events. The CDF detector is also being upgraded to handle the increased luminosity and improve its performance. It is hoped that 2 fb^{-1} of data will be collected. More data will reduce the statistical error and facillitate studies of systematic uncertainties as

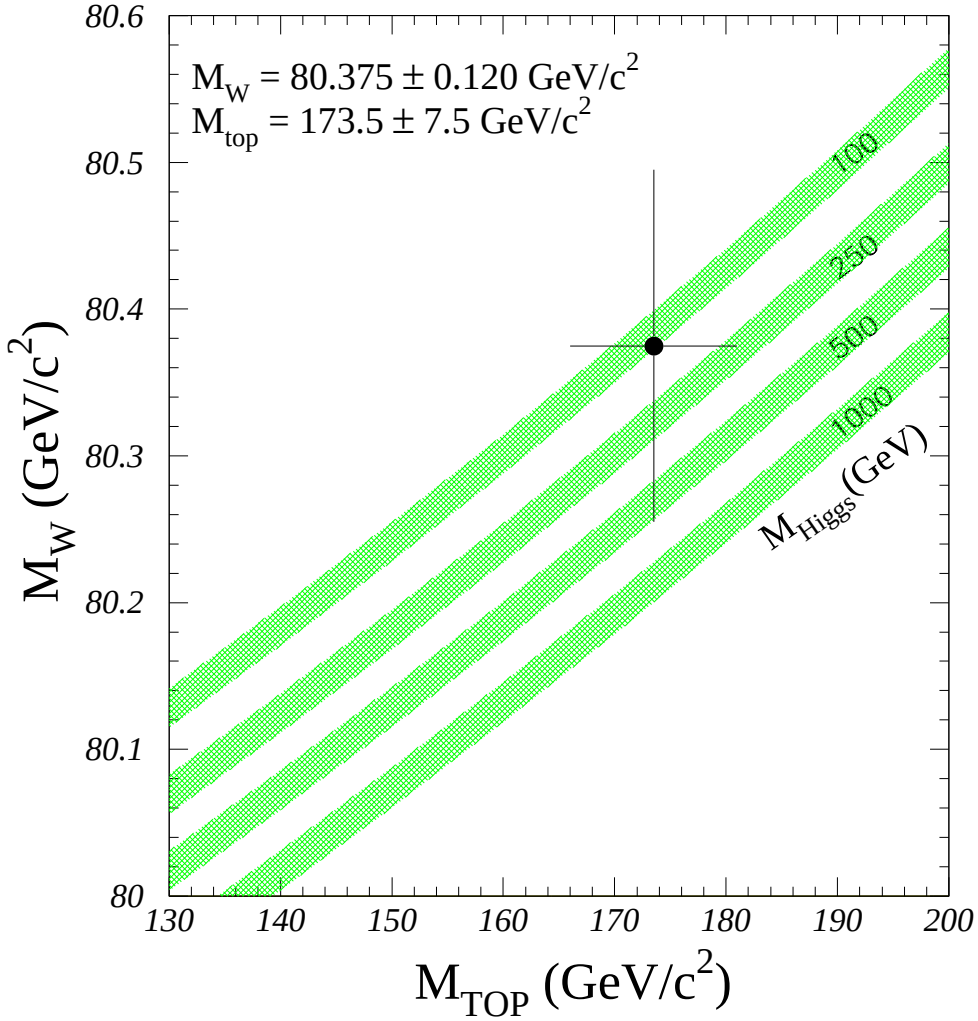

Figure 8.1: Measured top mass and W mass plotted along with the theoretical Higgs mass curves.

well. Increased data will provide better understanding of energy scale effects and the model of parton fragmentation. With 2 fb^{-1} of data, it is projected that the top mass will be measured to within an uncertainty of 2 GeV/c^2 [32].

Appendices

Appendix A

Useful Definitions

Definitions for quantities used in this thesis:

- In the CDF coordinate system, θ and ϕ are the polar and azimuthal angles, respectively, in relation to the proton beam direction, which is the positive z-axis.

- η, pseudorapidity, is defined as

$$\eta = -ln[tan(\theta/2)]$$

- ΔR, is the radius of a cone defined as

$$\Delta R = \sqrt{(\Delta\eta)^2 + (\Delta\phi)^2}$$

- $\mathrm{P_T}$, the transverse momentum of a particle, is the momentum perpendicular to the beam pipe.

$$\mathrm{P_T} = \mathrm{P}sin\theta$$

  where P is the total momentum of a particle and θ is the angle the particle makes with the beam axis. ($\theta = 0$ is parallel and in the same direction as the proton beam.)

- $\mathrm{E_T}$, the transverse energy, is the energy perpendicular to the beam direction of a particle.

$$\mathrm{E_T} = \mathrm{E}sin\theta$$

where E is the total energy of a particle and θ is the angle the particle makes with the beam axis.

- $\not{E}_T$, missing E_T, is the energy that is missed in the detector. It is calculated as the negative vector sum of all energy measured in the calorimeter such that the $\not{E}_T$ plus the total calorimeter energy sum to zero. Because neutrinos do not deposit any observable energy in the detector, large $\not{E}_T$ is often an indicator of the presence of a neutrino in the event.

- Luminosity is determined by integrating the instantaneous luminosity over the course of data taking. In general, for a given process

$$R = \sigma \dot{L}$$

where R is event rate, σ the cross section, and L the instantaneous luminosity. The instantaneous luminosity is determined by observing event rates for a process with a well known cross section. At CDF, it is determined from coincidence event rates in beam-beam counters located very near the beam line.

Appendix B

The Relative Jet Response

The relative jet corrections are used to balance the calorimeter jet response as a function of η. They correct for eta cracks and possible differences between the response of the central, plug, and forward calorimetry. In a perfect detector, dijet should balance back-to-back in P_T. This fact is used to equate jets in the central calorimetry to other detector regions. The corrections are derived by equating all jets to an equivalent central jet. This is accomplished by looking at dijet events where one jet is required to be in the central calorimeter ($0.2 < |\eta| < 0.7$) and sufficiently far from the 90 degree and 30 degree cracks. Jet response in this region is very flat and has been studied extensively for other analyses. The correction factor is parametrized as a function of η and the P_T of the jet. To account for possible changes in calorimeter response during extended shutdowns, the relative corrections are derived separately for the Run 1A and Run 1B collider runs.

B.1 Data Sets

Jet data collected during the run under study is used to derive the relative jet corrections. Data events are selected from the single jet triggers: JET20 (at least one jet with $P_T > 20$ GeV), JET50 (at least one jet with $P_T > 50$ Gev), JET70 (at least one jet with $P_T > 70$ Gev), and JET100 (at least one jet with $P_T > 100$ Gev). Dijet events are selected from the jet data samples based upon the following criteria:

- At least one jet in the region $0.2 < |\eta| < 0.7$
- Two jets with $P_T > 15$ GeV/c
- No other jets with $P_T > 15$ GeV/c
- Primary vertex cut

  One vertex for Run 1A

  One or two vertices for Run 1B
- $|Z_{vertex}| < 60$ cm
- $\Delta\phi_{jet1-jet2} > 2.7$ radians
- Event passes a cosmic ray filter

The vertex requirement was loosened to 2 primary vertices in Run 1B because more than half of the events have more than one vertex due to the increased luminosity. In addition, the ΣP_T of the two dijets is required to be greater than twice the single jet trigger threshold. The ΣP_T requirements for each trigger sample are shown in Table B.1. This is done to avoid biases due to trigger thresholds. For Run 1B, the JET100 sample was divided into two samples to improve the extrapolation to very large P_T jets.

Trigger	ΣP_T
JET20	50
JET50	110
JET70	150
JET100	210 310 (1B)

Table B.1: The ΣP_T requirements for events selected from each jet trigger.

B.2 Method

To perform the jet balancing, a quantity known as the $\not{E}_T$ projection fraction, MPF, is used. It is defined as:

$$MPF = \frac{2 \cdot \vec{\not{E}}_T \cdot \hat{P}_T^{probe}}{P_T^{trigger} + P_T^{probe}} \tag{B.1}$$

The central jet is refered to as the *trigger* jet, while the other jet is the *probe* jet. In the case where both jets lie in the central , a random number generator is used to pick the *trigger* jet. The factor of 2 arises from dividing by the average jet P_T. This quantity represents the fraction of energy "missing" in the direction of the *probe* jet. That is,

$$\vec{\not{E}}_T \cdot \hat{P}_T^{probe} = P_T^{trigger} - P_T^{probe} \tag{B.2}$$

Using the MPF, rather than simple P_T balance, minimizes K_T kick effects from soft jets in the event. Finally, the correction factor, β, is defined as

$$\beta = \frac{P_T^{trigger}}{P_T^{probe}} \tag{B.3}$$

can be expressed

$$\beta = \frac{2 + MPF}{2 - MPF} \tag{B.4}$$

The quantity β is the relative jet scale for a given P_T and η. A smooth fit is used to parametrize β. For a given η bin, a linear fit of β vs. $\langle P_T \rangle$ for each P_T range chosen. This yields two parameters, a slope and an intercept. The parameters are varied using MINUIT, and a smooth spline fit is made for each P_T range. The best fit parameters are obtained iteratively by minimizing the χ^2 of the fit to the data. The results for the Run 1A and 1B data are shown in Figures B.1 and B.2 respectively.

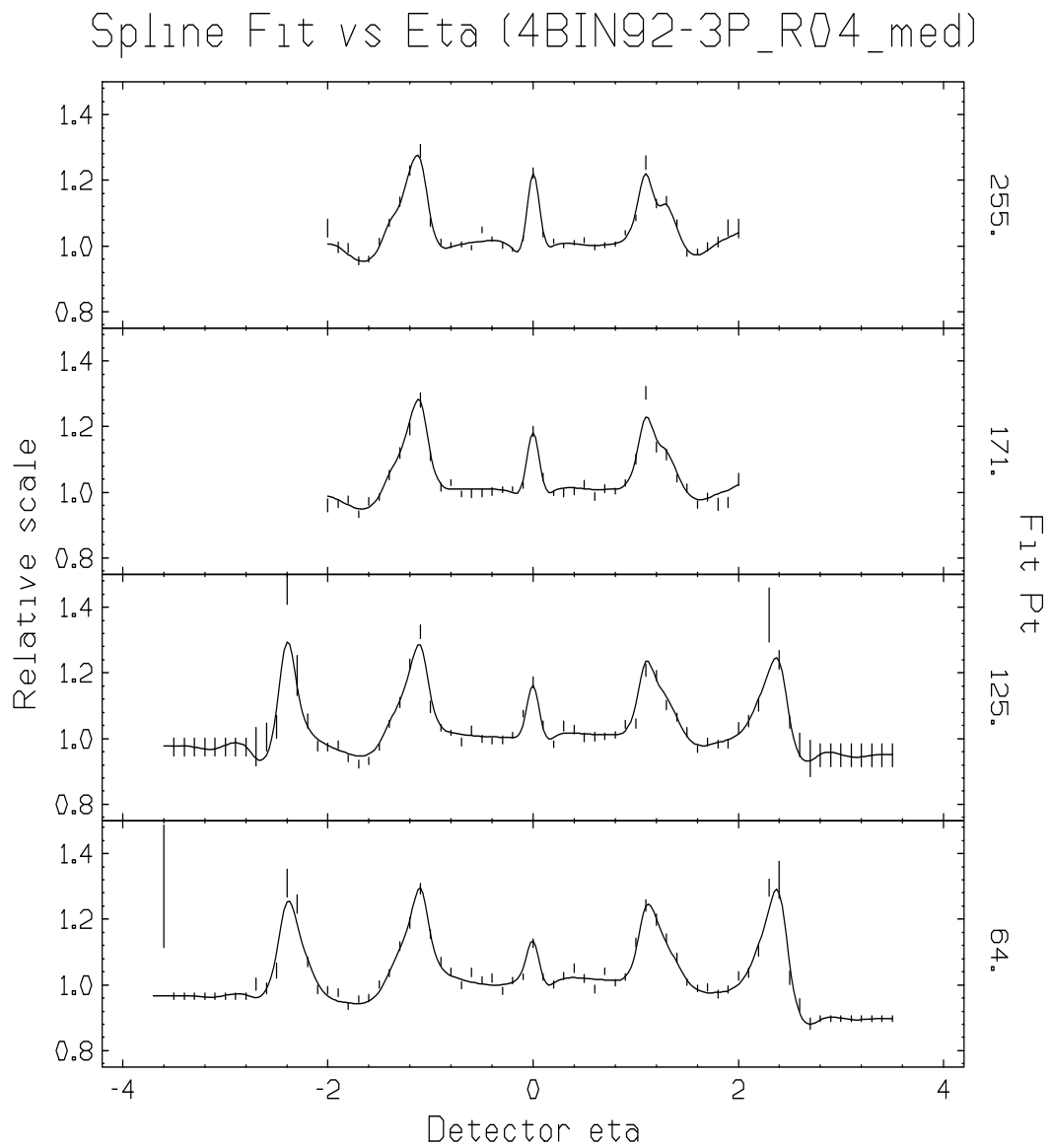

Figure B.1: Run 1A relative correction.

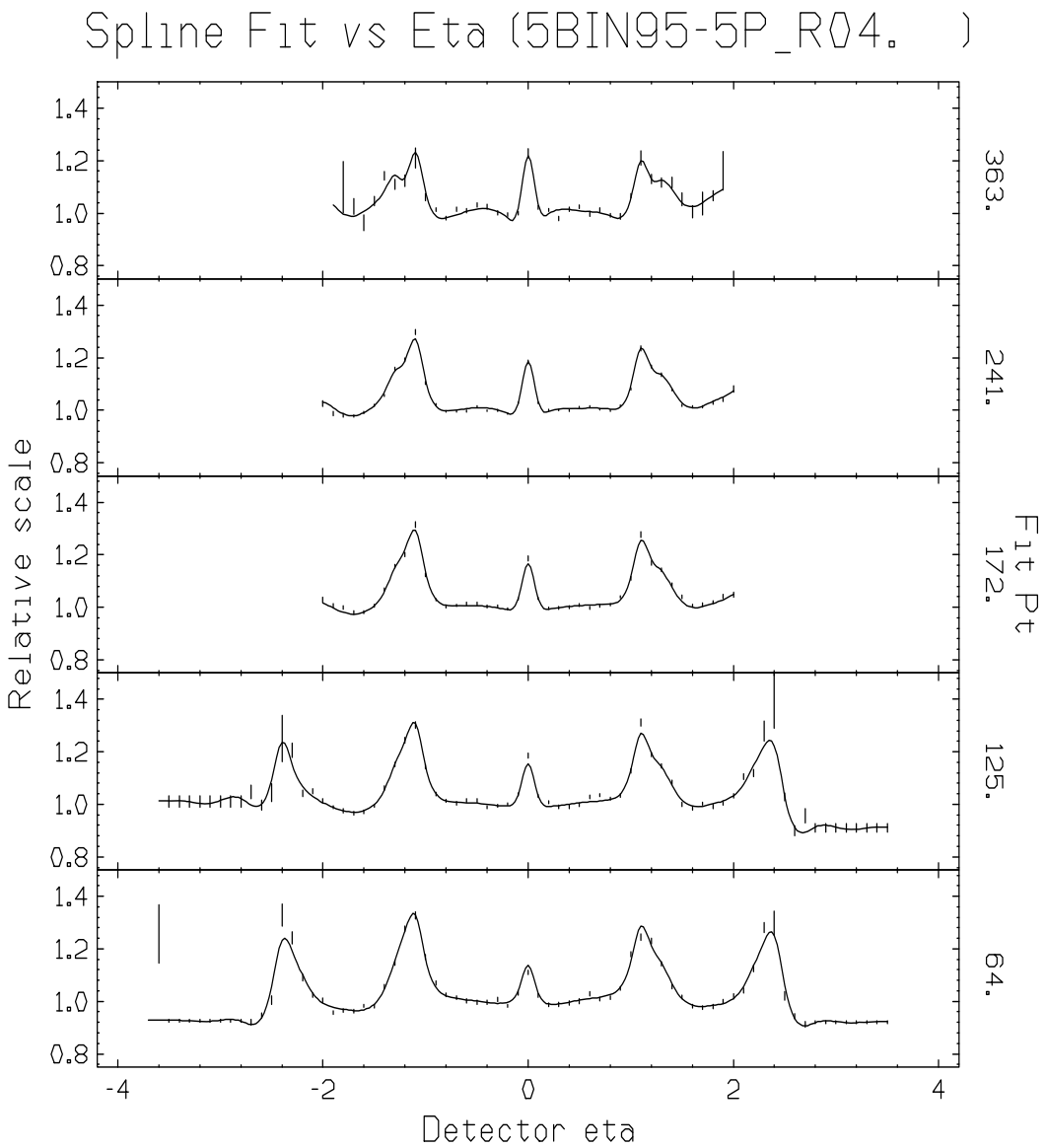

Figure B.2: Run 1B relative correction.

B.3 Crosschecks

To examine whether the relative corrections are behaving properly, it is sufficient to examine the MPF of dijet events after the corrections have been applied. Figures B.3 and B.4 show the corrected MPF plots for Run 1A and Run 1B dijet events. Close examination reveals systematic shifts at $\eta = 0$ and $\eta = \pm 1.1$ in both plots. This was determined to be due to spline fits inability to correctly fit the peaks in these regions. To account for this, an additional linear correction was applied to these regions. Figures B.5 and B.6 display the corrected MPF distributions with this correction. The uncertainty on the relative correction is determined from the variance in the corrected MPF plot.

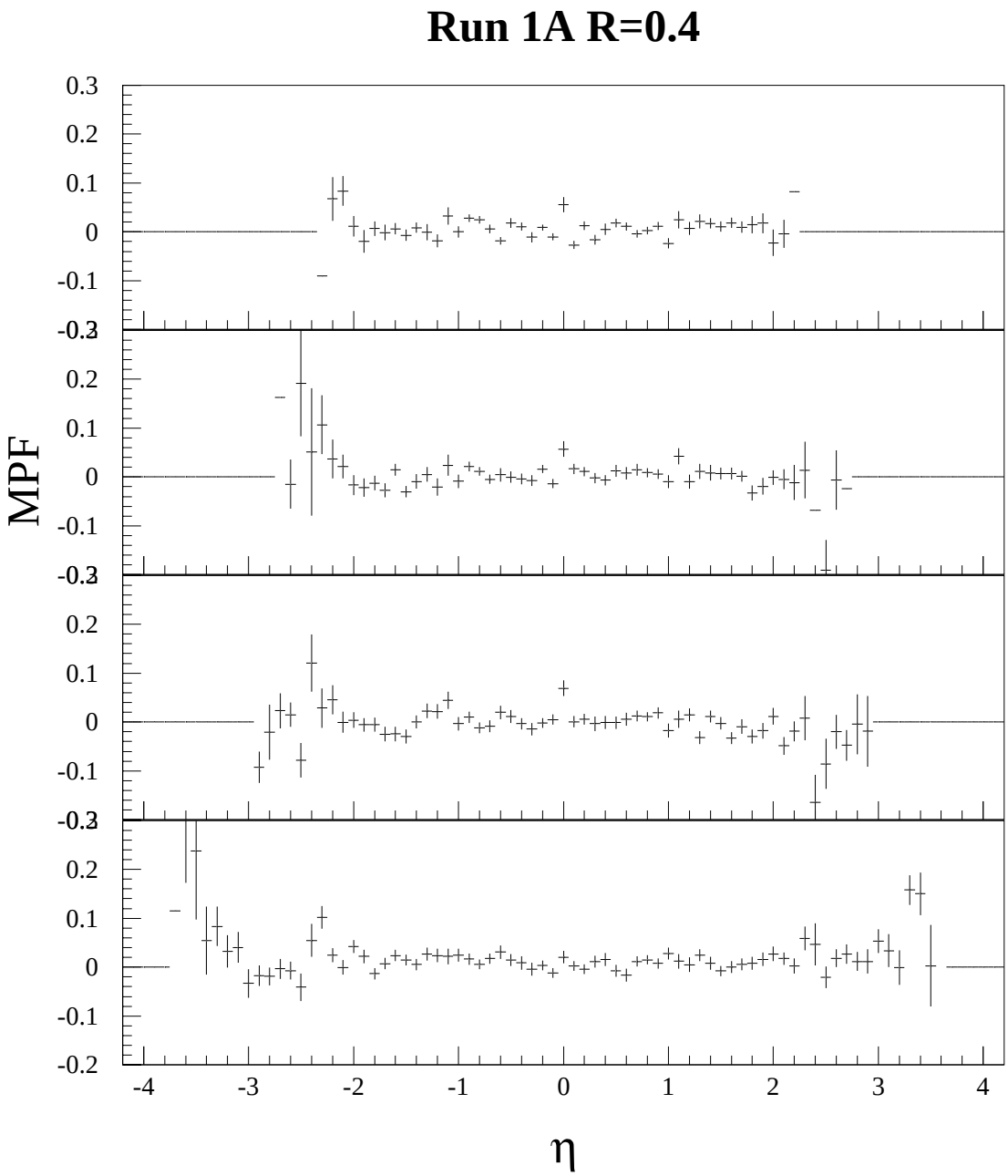

Figure B.3: Run 1A corrected $\not{E}'_T$ projection fraction with additional corrections for $\eta = 0$ and $\eta = \pm 1.1$.

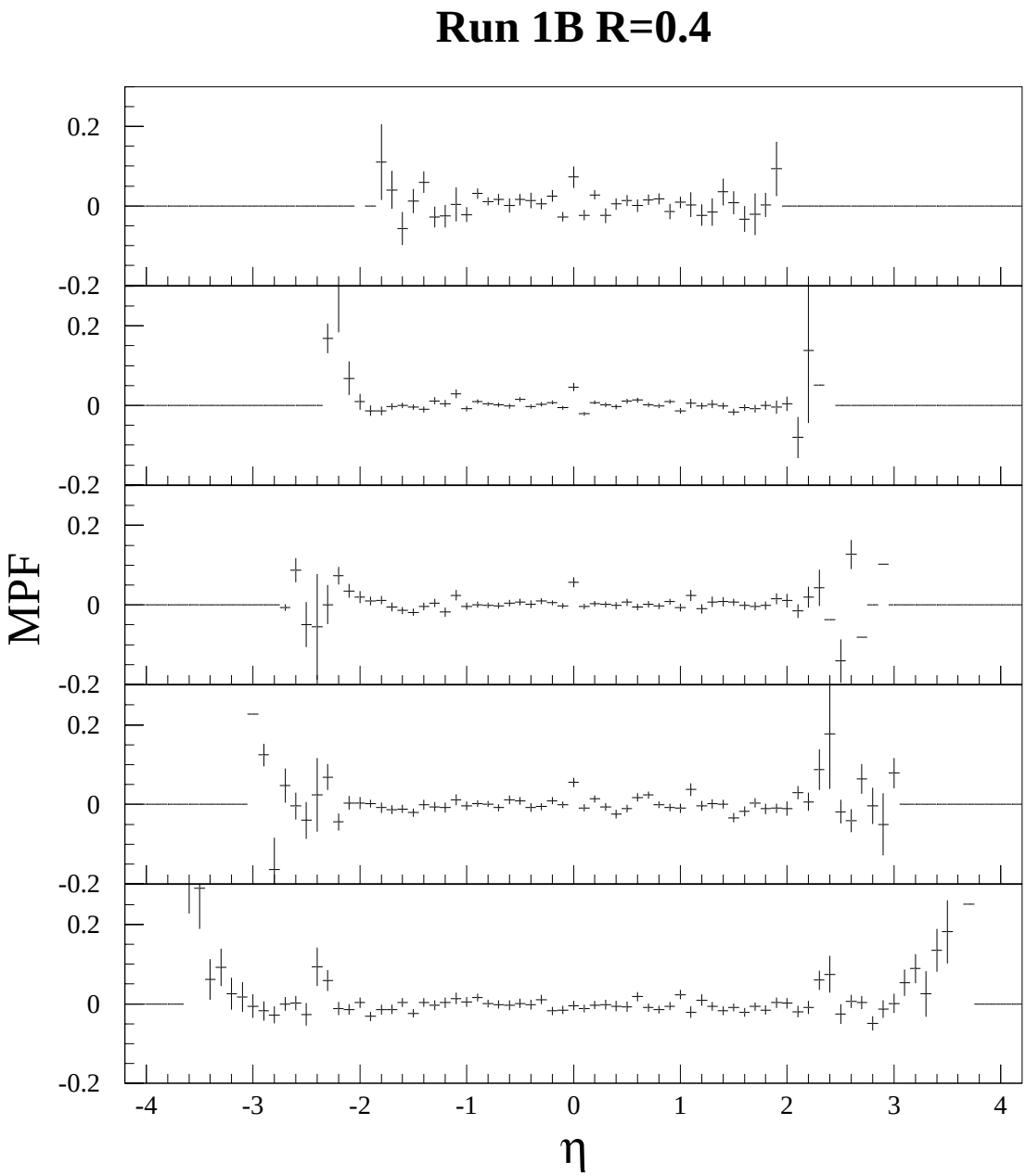

Figure B.4: Run 1B corrected $\not{E}_T$projection fraction with additional corrections for $\eta = 0$ and $\eta = \pm 1.1$.

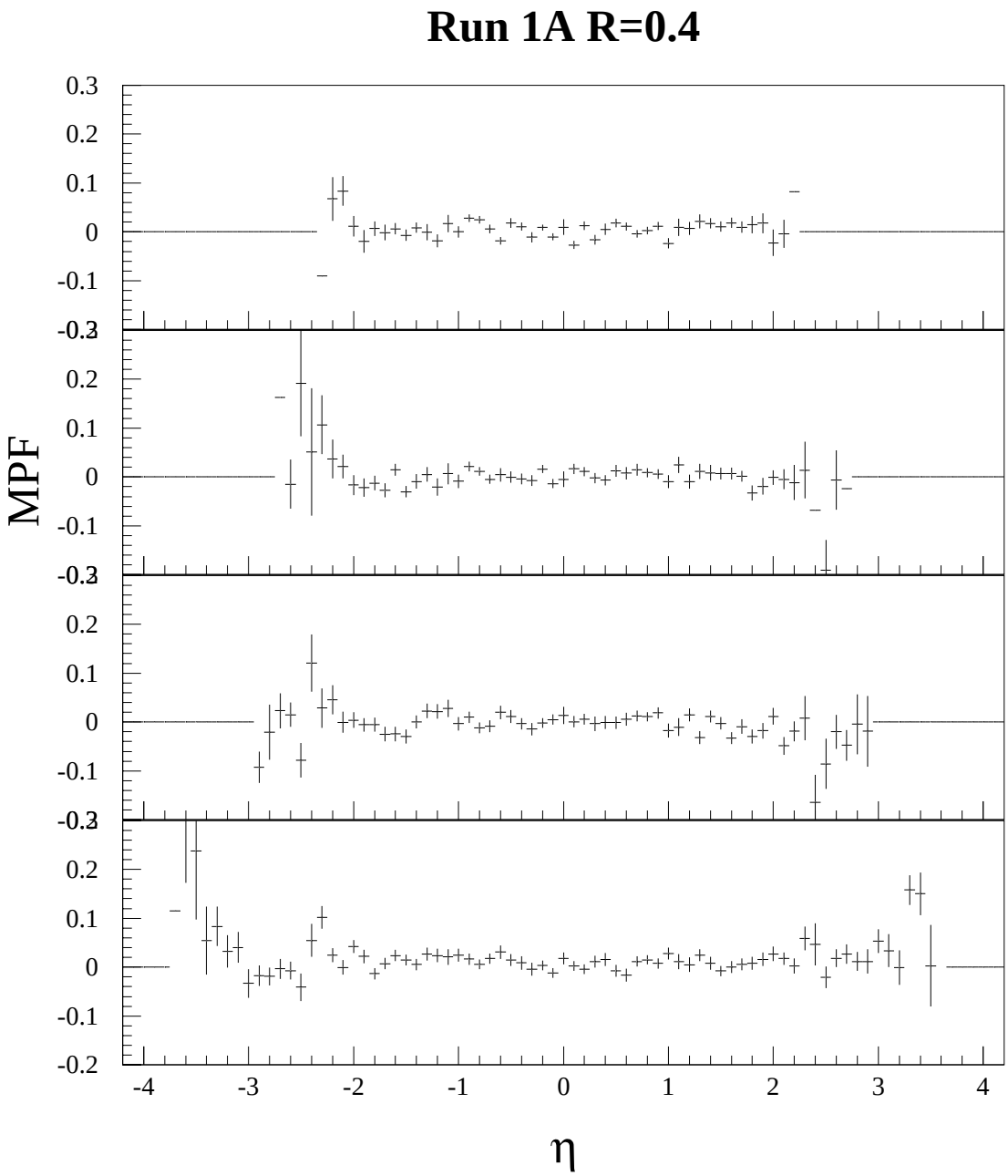

Figure B.5: Run 1A corrected $\not{E}'_T$ projection fraction with additional corrections for $\eta = 0$ and $\eta = \pm 1.1$.

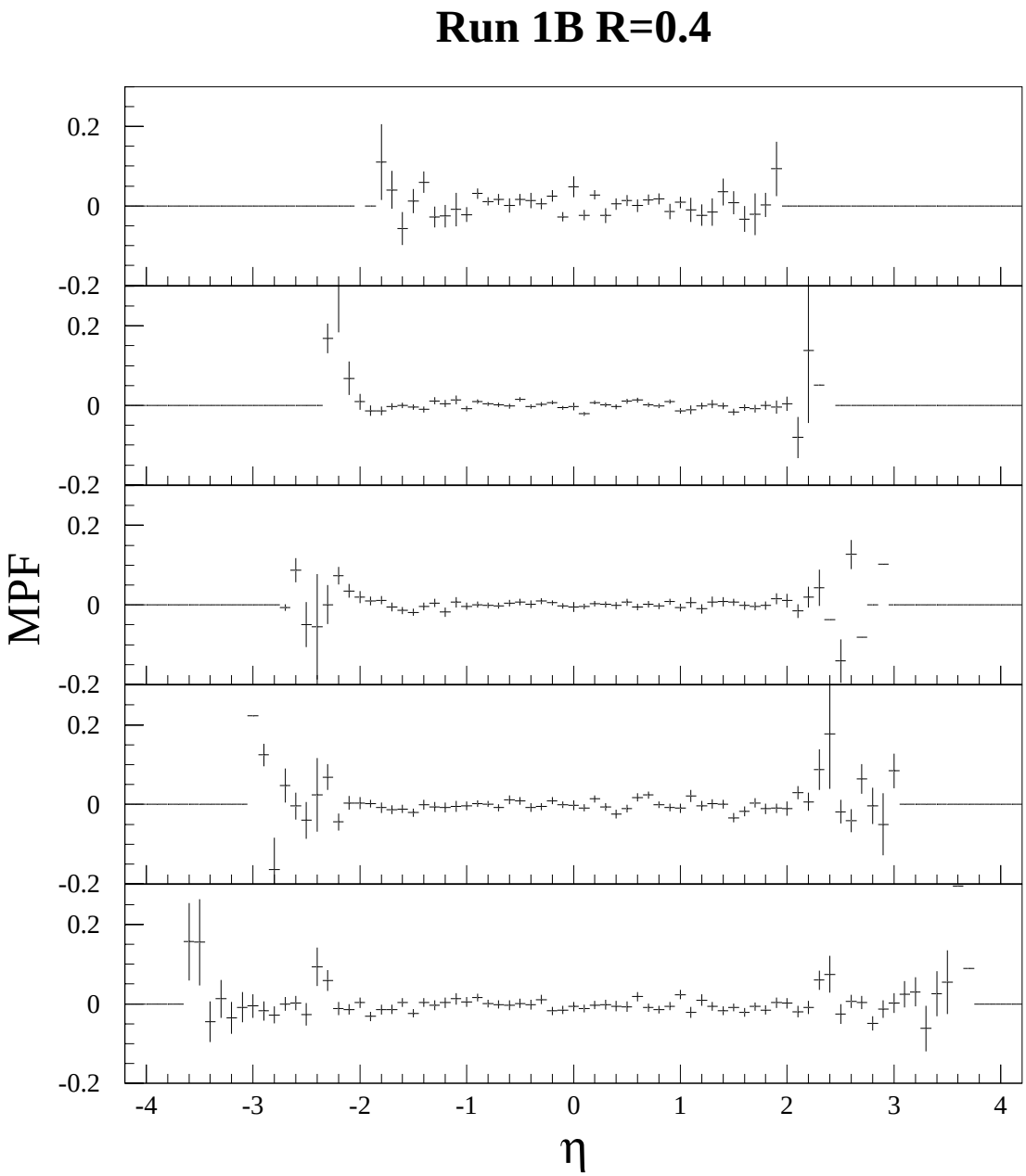

Figure B.6: Run 1B corrected $\not{E}'_{\mathrm{T}}$projection fraction with additional corrections for $\eta = 0$ and $\eta = \pm 1.1$.

Appendix C

Background Shape Crosschecks

The systematic uncertainty for the background shape in the top mass measurement is determined by comparing the expected results from the VECBOS model using different Q^2 scales. This assumes that VECBOS W + jet Monte Carlo is a good model for the backgrounds in the lepton + jets sample. In particular, this appendix addresses the following questions:

- Does VECBOS accurately model W + jets?
- How sensitive is the VECBOS distribution to model parameters?
- Are non-W + jets events reasonably modeled?

C.1 Backgrounds in the Mass Sample

The majority of the background in the lepton plus jets $t\bar{t}$ sample is expected to come from W + jets (~3 events) but there is some contribution from non-W backgrounds due to (1) misidentified leptons in QCD-jet events or semileptonic b-decays from $b\bar{b}$ events (~2 events), (2) Z decays where one lepton is undetected due to detector inefficiencies (<1 event), and (3) diboson decays such as WW, WZ, and ZZ (<1 event). At question here is how accurately the VECBOS Monte Carlo program reproduces the mass distributions for W plus multijet events and also for non-W background samples.

C.2 W plus Jets Events

As noted above, W + jet events are predicted as the main source of background to $t\bar{t}$ events. For this reason, VECBOS W + jets Monte Carlo generated with $Q^2 = P_T^2$ is used to represent the background when fitting the top mass. As a reasonable variation on this model, one can also look at the results using a different Q^2 scale. VECBOS generated with $Q^2 = M_W{}^2$ is used for this. Figure 1 shows the mass distributions for both Q^2 scales. Note that they are very similar in shape with the $P_T{}^2$ sample being slightly stiffer. In the subsequent sections, the VECBOS $P_T{}^2$ is examined to determine how well it agrees with expected background distributions. All further VECBOS W + jet references and distributions will be for $Q^2 = P_T{}^2$.

Non-Isolated Lepton plus Jets Events

The largest source of Non-W backgrounds is expected to come from QCD and $b\bar{b}$ events. These backgrounds are reduced primarily by requiring an isolation cut (ISO < 0.1) on the lepton candidate. To study a sample rich in such backgrounds, this cut is simply reversed (ISO > 0.1) while keeping all other cuts the same. In the current 1B data sample (81 pb^{-1}) there are 171 events passing the anti-isolation cuts. When these events are fit to the mass hypothesis, 164 have a good $\chi^2 < 10.0$. The mass distribution for this sample is shown in Figure 2 along with the VECBOS W + jet prediction. There is good agreement between the two distributions. The Kolmogorov-Smirnov test yields an 36% C.L. that the distributions come from the same sample.

Plug Electron W + Jets

Kinematically, the W and hence the lepton from $t\bar{t}$ decay is expected to be central ($|\eta| < 1.1$). For this reason, one expects a sample of W candidates from plug electrons ($1.1 < |\eta| < 2.4$) to contain real W + jet events with not much $t\bar{t}$ contribution. Again this sample is generated keeping all cuts exactly the same as the standard sample. In the current data sample, there are 29 events passing the cuts. Of these events, 26 have a good fit with $\chi^2 < 10.0$ and their mass distribution is shown in Figure 3. For comparison, the

VECBOS W + jet distribution is also shown. The KS test yields a 35% C.L. that the two distributions come from the same sample.

W + Loose Jets

By loosening the E_T cuts on the jets, the amount of background in the sample can be greatly increased. This provides a high statistic sample which is dominated by backgrounds, but is in a different kinematic region than the standard W + jets. The loose jet sample is defined by requiring at least 4 jets with raw $E_T > 8.0$ and $|\eta| < 2.4$ and at most 2 jets with raw $E_T > 15.0$ and $|\eta| < 2.0$. The latter cut is to reject events in the standard mass sample in order to reduce the $t\bar{t}$ contribution. There are 280 events passing these cuts in the 1B data, of which 243 have a fit with a $\chi^2 < 10.0$. The distribution for these events is shown in Figure 4 along with the VECBOS distribution when the same cuts are applied. The KS test yields a 45% C.L. that the two distributions come from the same sample.

Z + Jets

The Z candidate events removed from the sample during the selection process can be fit to the mass hypothesis by treating one leg of the Z as if it were $\not{E}_T$. This is done for each lepton resulting in two possible fitted solutions per event. The Z + jet sample can provide a couple checks on our background model. As it is expected to contain no top contamination, the Z + jet data sample can be compared directly to VECBOS Monte Carlo samples of both Z's and W's. At present, there are only 10 events in the data so this method is not statistically significant but could provide a very good cross check on VECBOS in Run II. In principle, the physics processes which produce W + jet and Z + jet events are identical (the only difference being the mass of the Bosons), and hence it is reasonable to expect a similar reconstructed mass distribution for Z + jet events. The reconstructed mass distributions for the data and VECBOS are shown in Figure 5. The KS test yields an 85% C.L. that the VECBOS Z + jet and W + jet distributions come from the same parent sample.

C.3 Conclusions

The background shape and how well it is modeled by our VECBOS W + jet Monte Carlo program has been cross checked against different samples. The reconstructed mass distributions for VECBOS agree very well with data samples expected to contain non-top W + jet events. Nothing was observed to suggest that it is not modeling the real W + jet backgrounds correctly. In addition, it also agrees very well with samples expected to be rich in non-W backgrounds. At this time the statistics are limited, but VECBOS seems to be a fair model for the expected backgrounds.

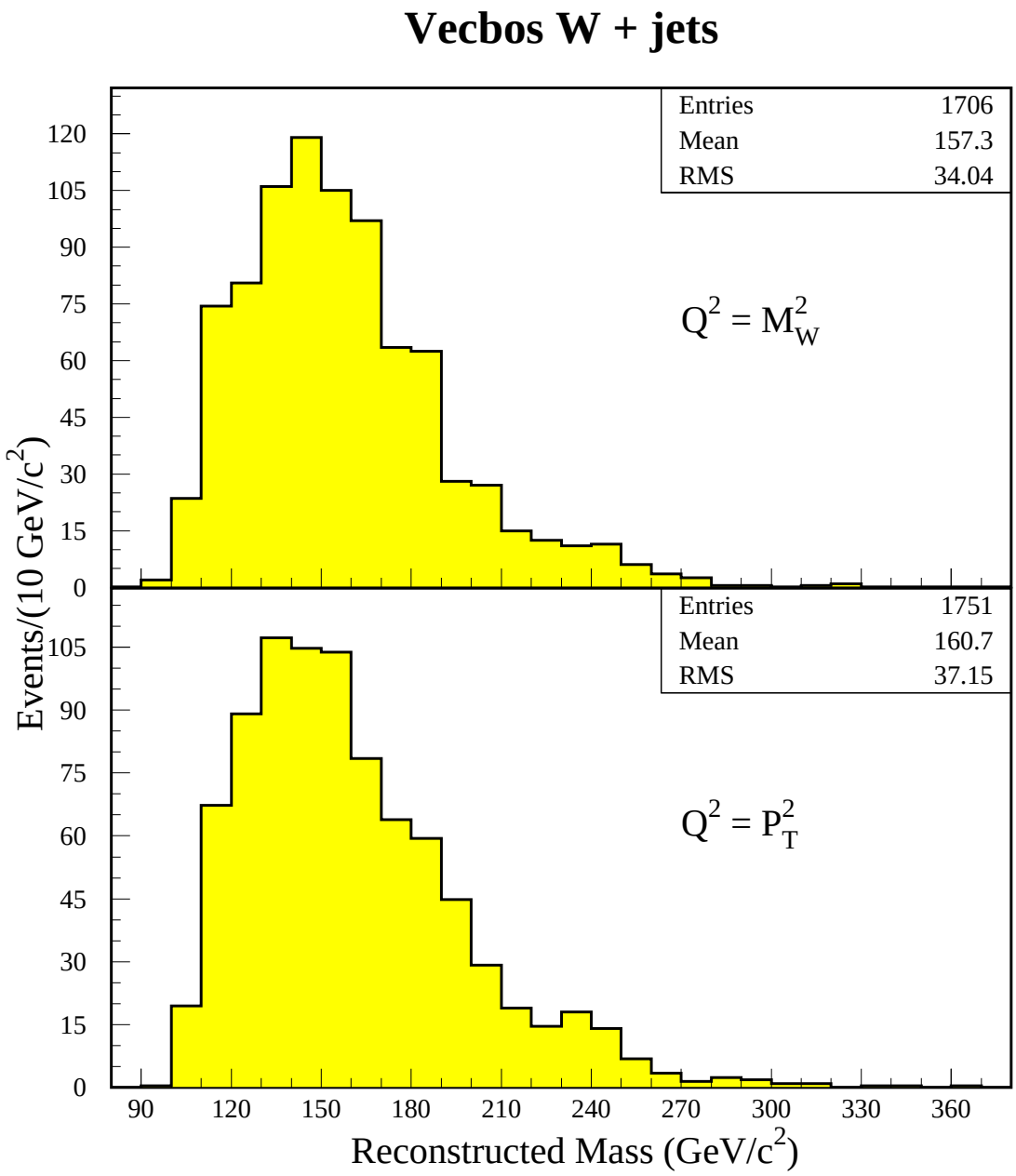

Figure D.1: The reconstructed mass for VECBOS with $Q^2 = M_W^2$ and $Q^2 = P_T^2$.

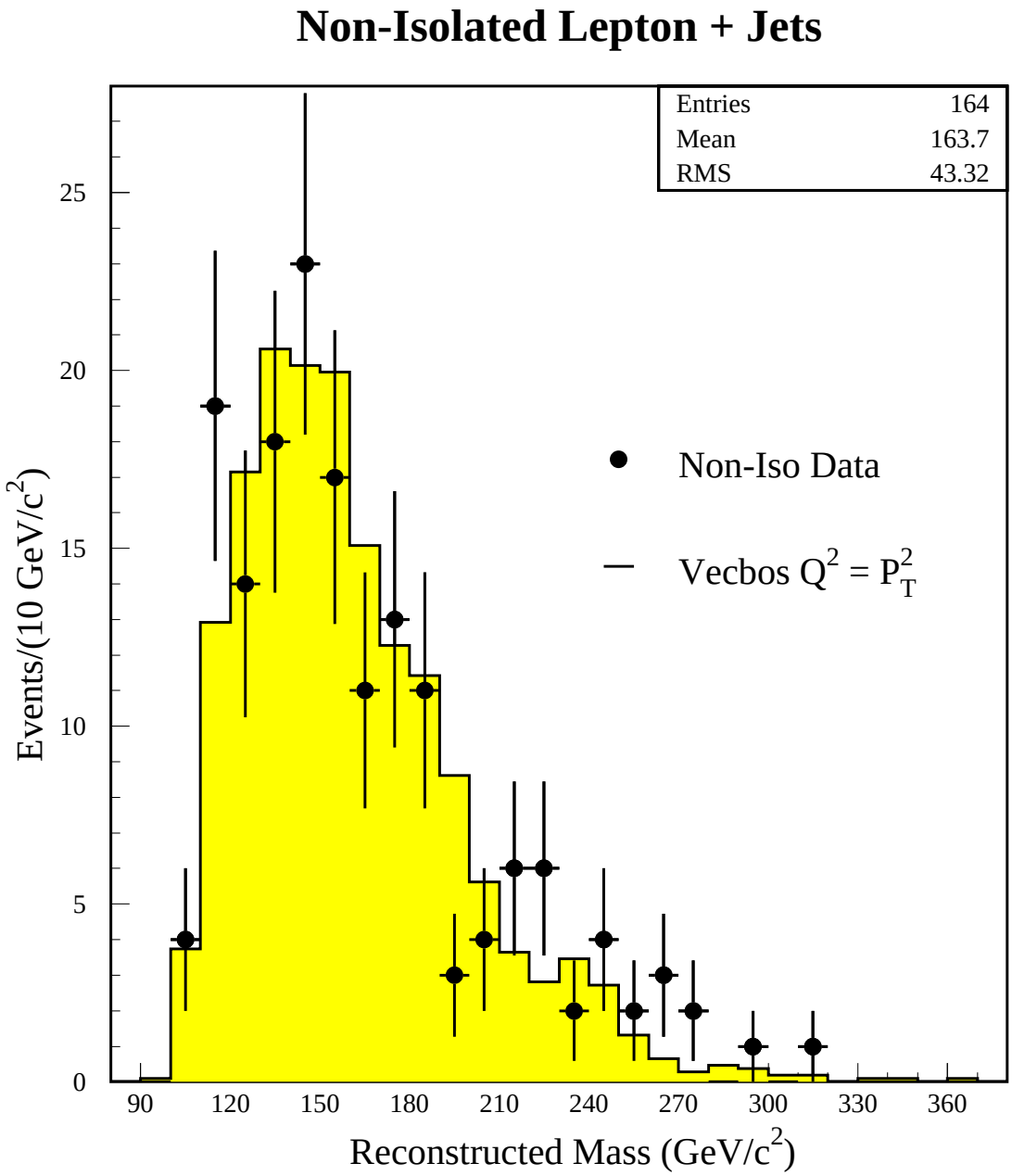

Figure D.2: The reconstructed mass for non-isolated lepton events (points) along with the VECBOS $Q^2 = P_T^2$ distribution (histogram). A KS test gives a 36% C.L. that they are the same.

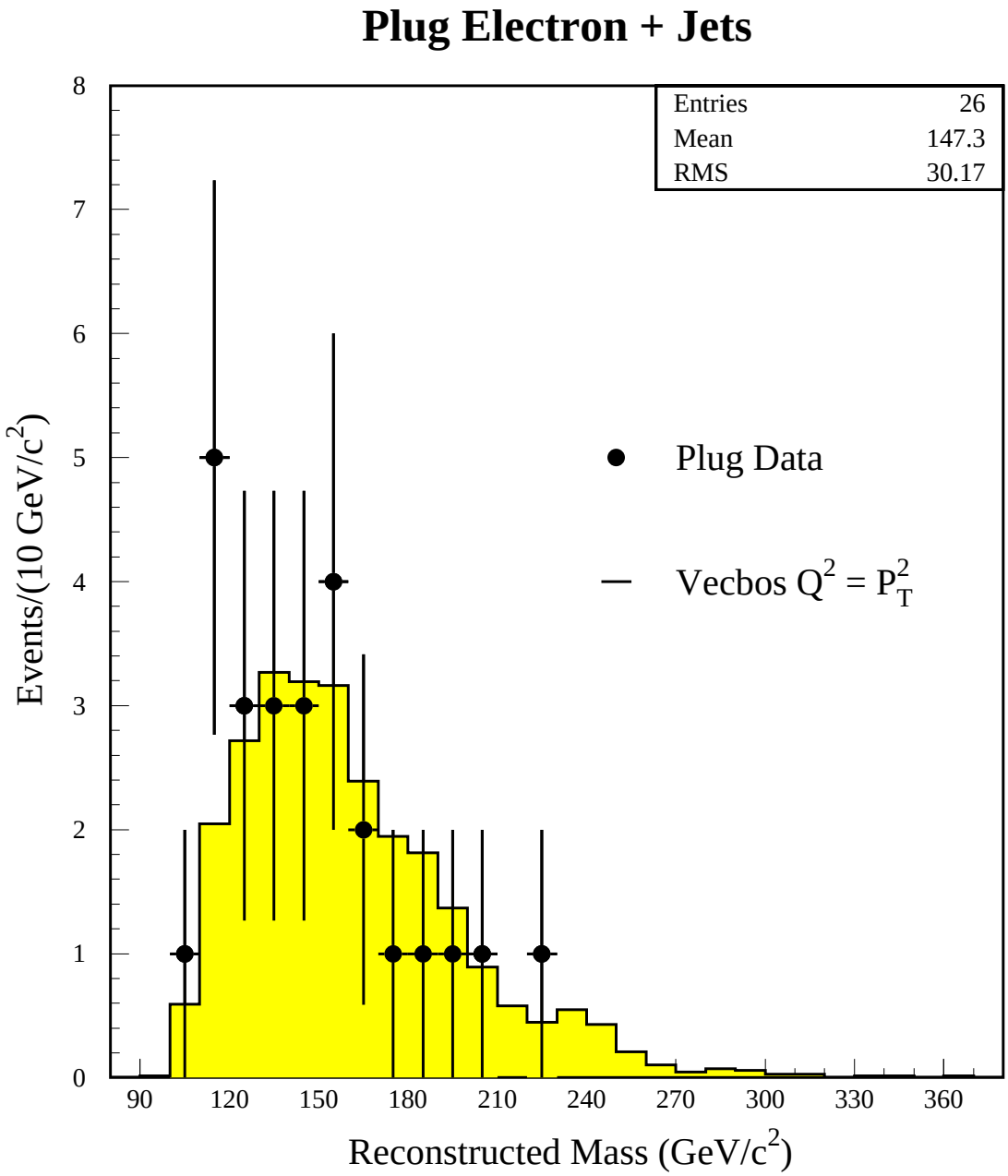

Figure D.3: The reconstructed mass for plug electron W events (points) along with the VECBOS $Q^2 = P_T^2$ distribution (histogram). A KS test gives a 33% C.L. that they are the same.

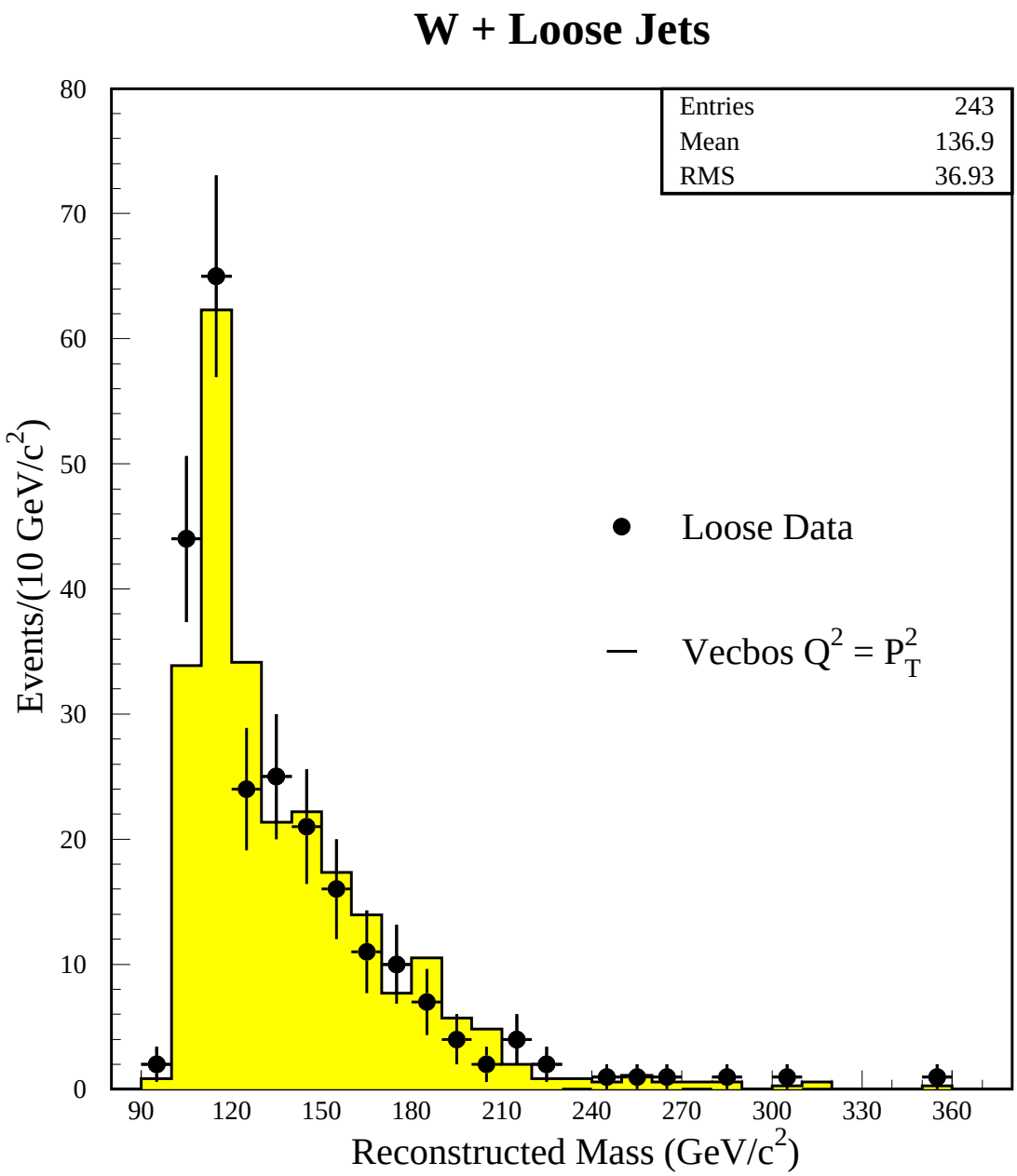

Figure D.4: The reconstructed mass for W + loose jet events (points) along with the VECBOS $Q^2 = P_T^2$ distribution with loose jet cuts (histogram). A KS test gives a 45% C.L. that they are the same.

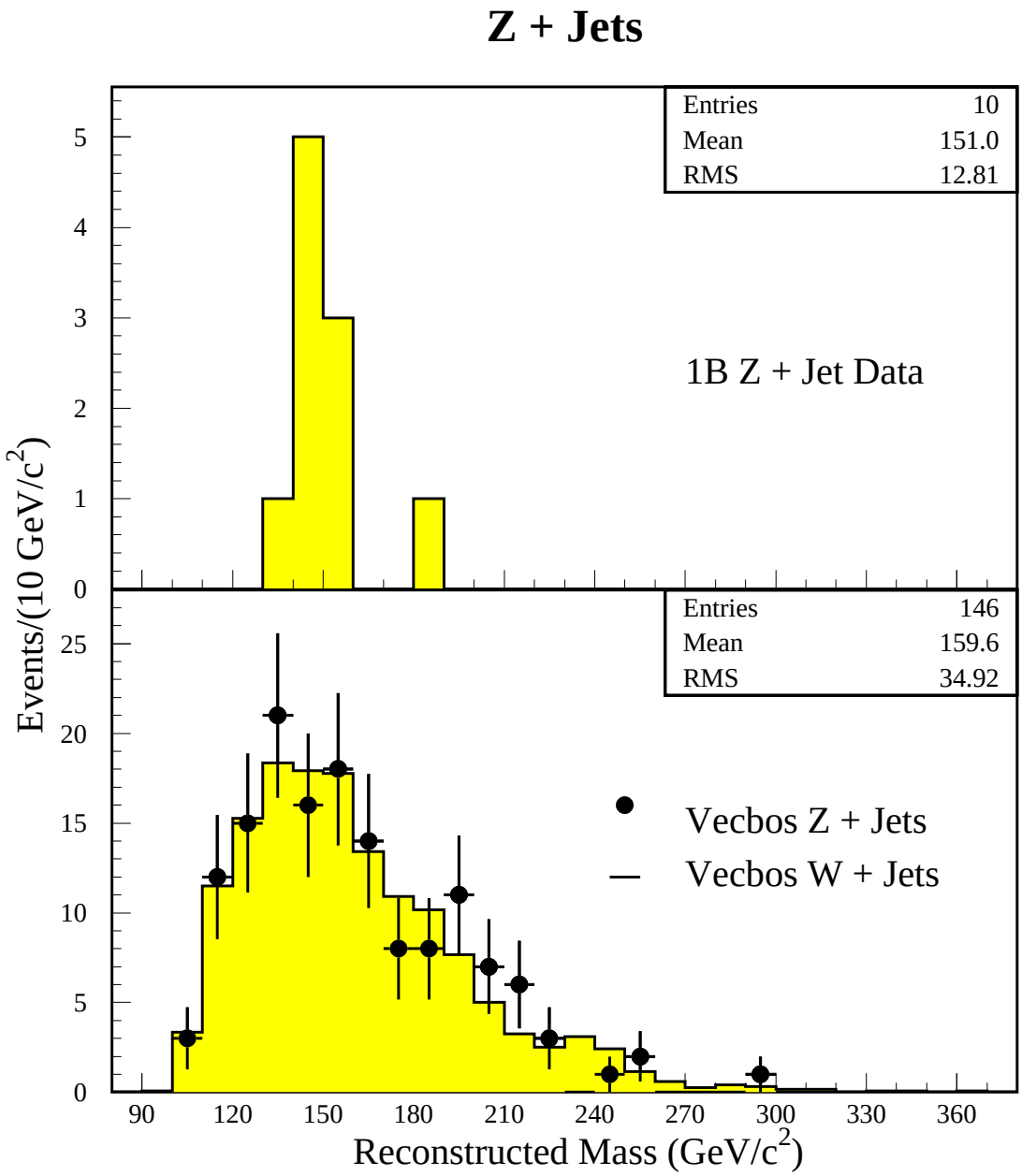

Figure D.5: The reconstructed mass for Z + 4 jet events in the 1B data and a comparison of VECBOS Z + jet and W + jet Monte Carlo. A KS test yields an 85% C.L. that the latter two distributions are the same.

Bibliography

[1] C. Albajar *et al.*, Z. Phys. **C37**, 505 (1988).

[2] F. Abe *et al.*, Phys. Rev. Lett **68**, 447 (1992).

[3] S. Abachi *et al.*, Phys. Rev. Lett **72**, 2138 (1994).

[4] F. Abe *et al.*, Phys. Rev. Lett **74**, 2626 (1995).

[5] S. Abachi *et al.*, Phys. Rev. Lett **74**, 2632 (1995).

[6] P. Azzi, Thesis, University of Padova, (1996).

[7] F. Abe *et al.*, Phys. Rev. Lett **80** 2779 (1988).

[8] F. Abe *et al.*, Phys. Rev. D **50**, 2966 (1994).

[9] F. Abe *et al.*, Phys. Rev. D **80**, 2767 (1998).

[10] Gordon Kane, *Modern Elementary Particle Physics: The Fundamental Particles and Forces?*, Addison-Wesley (1993).

[11] I. Bigi *et al.*, Phys. Lett. B, **157**, (1986).

[12] L. Orr, Phys. Rev. D **44**, 44, (1991).

[13] R. R. Wilson, Phys. Today **10**,23 (1977).

[14] F. Abe *et al.*, Nucl. Instrumen. Meth. **A271**, 387 (1988).

[15] D. Amidei, *et al.*, Nucl. Instrumen. Meth. **A350**, 73 (1994).

[16] D. Glenzinski, Ph.D. Thesis, The Johns Hopkins University, (1995).

[17] D. Kestenbaum, Ph.D. Thesis, Harvard University, (1996).

[18] C. Mao, Ph.D. Thesis, University of Michigan, (1997).

[19] J. Freeman *et al.*, ANL-HEP-CP-80-51, 190 (1987).

[20] G. Marchesini *et al.*, Comp. Phys. Comm. **67**, 465 (1992).

[21] F. Abe *et al.*, FERMILAB-PUB-98/327-E, submitted to Phys. Rev. D, October (1998).

[22] T. Sjöstrand, Comp. Phys. Comm. **82**, 74 (1994).

[23] F. Paige and S. Protopopescu, BNL Report No. 38034, 1986 (unpublished).

[24] F.A. Berends *et al.*, Nucl. Phys. B **357**, 32 (1991).

[25] F. Abe *et al.*, Phys. Rev. Lett **75**, 11 (1995).

[26] M. Jeżabek and J.H. Kühn, Phys. Rev. D **48**, R1910 (1993).

[27] F. Abe *et al.*, Phys. Rev. Lett **74**, 341 (1995).

[28] F. Bedeschi *et al.*, CDF internal document No. 3878 (1996).

[29] F. Abe *et al.*, Phys. Rev. Lett **80**, 2773 (1998).

[30] K. Tollefson, Ph.D. Thesis, University of Rochester, (1997).

[31] T. Dorigo, FERMILAB-CONF-98/239-E, PASCOS 98, March (1998).

[32] *Future Electro Weak Physics at the Fermilab Tevatron: Report of the tev_2000 Study Group*, edited by D. Amidei and R. Brock.